Metastable Phases and Dynamics of Low-Dimensional Strongly-Correlated Atomic Quantum Gases

A dissertation presented

by

Susanne Pielawa

to

The Department of Physics

in partial fulfillment of the requirements

for the degree of

Doctor of Philosophy

in the subject of

Physics

Harvard University

Cambridge, Massachusetts

August 2011

Thesis advisor   Author

Subir Sachdev   **Susanne Pielawa**

Metastable Phases and Dynamics of Low-Dimensional Strongly-Correlated Atomic Quantum Gases

Abstract

In this thesis we theoretically study low-dimensional, strongly corrleated systems of cold atoms, which are not in an equilibrium situation. This is motivated by recent experimental progress, which has made it possible to study quantum many-body physics in a controllable and clean setting; and parameters can be changed during the experiment.

In Chapter 2 and 3 we study phases and quantum phase transitions of 'tilted' Mott insulator of bosons. We analyze a variety of lattices and tilt directions in two dimensions: square, decorated square, triangular, and kagome. We show that there are rich possibilities for correlated phases with non-trivial entanglement of pseudospin degrees of freedom encoded in the boson density. For certain configurations three-body interactions are necessary to ensure that the energy of the effective resonant subspace is bounded from below. We find quantum phases with Ising density wave order, with superfluidity transverse to the tilt direction, a quantum liquid state with no broken symmetry. We also find cases for which the resonant subspace is described by effective quantum dimer models.

In Chapter 4 we study spin 1/2 chains with a Heisenberg interaction which are coupled in a way that would arise if they are taken off graphene at a zig-zag edge.
In Chapter 5 we theoretically analyze interference patterns of parametrically driven one-dimensional cold atomic systems. The parametric driving leads to spatial oscillations in the interference patter, which can be analyzed to obtain the sound velocity of the 1d system, and to probe spin-charge separation.

Contents

Citations to Previously Published Work

Most of the results of Chapter 2 appear in

"Correlated phases of bosons in tilted frustrated lattices",
Susanne Pielawa, Takuya Kitagawa, Erez Berg, and Subir Sachdev,
Phys. Rev. B. **83**, 205135 (2011)

Chapter 5 appears in its entirety in

"Interference of parametrically driven one-dimensional ultracold gases",
Susanne Pielawa,
Phys. Rev. A. **83**, 013628 (2011)

This thesis contains unpublished results, which will be submitted for publication soon.

Citations to other work by the author, not mentioned in this thesis

"Ramsey Interference in One-Dimensional Systems: The Full Distribution Function of Fringe Contrast as a Probe of Many- Body Dynamics",
Takuya Kitagawa, Susanne Pielawa, Adilet Imambekov, Jörg Schmiedmayer, Vladimir Gritsev, and Eugene Demler,
Phys. Rev. Lett. **104**, 255302 (2010)

"Engineering atomic quantum reservoirs for photons",
Susanne Pielawa, Luiz Davidovich, David Vitali, and Giovanna Morigi,
Phys. Rev. A **81**, 043802 (2010)

"Generation of Einstein-Podolsky-Rosen-Entangled Radiation through an Atomic Reservoir",
Susanne Pielawa, Giovanna Morigi, David Vitali, and Luiz Davidovich,
Phys. Rev. Lett. **98**, 240401 (2007)

Acknowledgments

I would like to begin by thanking my adviser, Subir Sachdev, for his guidance and encouragements, which made this work possible. I am grateful for many good ideas and advice he gave me, for his belief in my abilities, and for passing on his enthusiasm, which made my work so enjoyable and rewarding.

During the later stages of my PhD I enjoyed collaborating with Markus Greiner, whose beautiful experiments were a source of inspiration for part of the work presented in this thesis. Markus became a great mentor to me, and I would like to thank him for many discussions in which he shared his physical intuition that helped me see everything in a broader context.

I am grateful to Roy Glauber for being in my thesis committee, for his interest in my work, and for many illuminating conversations. I would like to thank Jenny Hoffman for many insights she shared with me and the advice she gave me during our monthly mentoring lunches.

During the last year I enjoyed working with Erez Berg, and I benefited much from his remarkable knowledge and intuition. The problem discussed in Chapter 5 of this thesis was suggested by Eugene Demler, whom I thank for introducing me to the field of ultracold atoms. I would like to thank Benoît Grémaud and Christian Miniatura for collaborating with me on the work presented in Chapter 4.

The condensed matter theory group here at Harvard has been a very inspiring and stimulating work environment. I learned a lot from fellow students and post docs, including David Pekker and Vladimir Gritsev, who taught me about dynamics in cold atoms and gave valuable feedback on my first project; Max Metlitski and Eun Gook Moon, who helped me deepen my understanding of field theory when I first needed to use it; Barbara Capagrosso-Sansone and Lode Pollet, who gave me advice on quantum Monte Carlo simulations and taught me many tricks to make my code more efficient; Takuya Kitagawa, with whom I collaborated on a few projects; Liza Huijse, who taught me a numerical technique I used to calculate correlation functions; Rajdeep Sensarma, Bernhard Wunsch, Nikolaj Zinner, Matthias Punk, Philipp Strack, Liang Fu, Mark Rudner, Lars Fritz, Ariel Amir, Misha Zvonarev, Charles Mathy, Izhar Neder, Ville Pietila, Ludwig Mathey Adilet Imambekov, Yejin Hu, Rudro Biswas, Luiz Santos, Alexey Gorshkov, Liang Jiang, Michael Gullans, Adi Pick, David Benjamin, Mehrtash Babadi, Suzanne Pittman, Gilad Ben-Shach.

I would like to thank Jonathan Simon and Waseem Bakr for explaining and showing their experiment to me, and I thank all members of the Greiner lab, including Eric Tai,

Ruichao Ma, Widagdo Setiawan, Kate Wooley-Brown, Philipp Preiss, Florian Huber, Simon Foelling, and Amy Peng for many stimulating discussions.

I thank the Centre for Quantum Technologies for hospitality during my stay in Singapore, where I enjoyed interacting with many scientists, including Berge Englert, Cord Müller, Vlakto Vedral, George Batrouni, Marcelo Santos, Marta Wolak, Momo Lu Yin, Elisabeth Rieper, Han Rui, Arun, Bess Fang, Niels Lörch, Lee Kean Loon, Ng Hui Khoon, Philippe Raynal, Arun, Libby Heaney, Elica Kyoseva, John Goold.

I would like to thank Ehud Altman, Steve White, Bryan Clark, and Krishnendu Sengupta for insightful conversations during their visits. I would like to thank Thierry Giamarchi for helpful discussions and hospitality during my visit to Geneva. I thank Fabian Essler, John Chalker, John Cardy, Steve Simon, Fiona Burnell, Vlatko Vedral for hospitality and for stimulating discussions during my visit to Oxford. During my PhD I continued collaborating with Giovanna Morigi, whom I thank for stimulating discussions and for hospitality during my visits to Barcelona and Saarbrücken.

I thank the administrative staff here at Harvard for all their help, especially Sheila Ferguson, Barbara Drauschke, and Heidi Kaye.

I would like to thank my fellow graduate students, including Yiwen Chu, Julia Rasmussen, Nick Hutzler, Chin Lin Wong, Eleanor Millman, Jonathan Ruel, David Benjamin, Daniyar Nergaliev, Vasily Dzyabura, Timur Gatanov, and Pavel Petrov for the good times we spent together.

Thanks to my friends and flatmates for making me feel at home in Boston. Special thanks to Jaya Remond, Catherine Girard, HyeWon Yoon, Wei Hu, Sabine Leisten, Naina Ratalsky, Jonathan Ruel, Roberto Olivares and Joel Yuen.

I thank close friends and family from home for their support, encouragement, and friendship.

I am grateful to the Studienstiftung des Deutschen Volkes for financial support.

Chapter 1

Introduction

Recent experimental progress in the field of ultracold atomic gases has made it possible to study quantum many-body physics in a controllable and clean setting (see Ref [1] for a review). This makes cold atoms in optical lattices candidates for analogue quantum simulators of real materials and model Hamiltonians in equilibrium. They are also particularly well suited to realize and study non-equilibrium quantum systems for the following reasons: cold atoms can be almost perfectly isolated from their environment, and parameters can be changed during the experiments.

Since the observation of a quantum phase transition from a superfluid state to an interaction driven insulating state [2] there has been a lot of effort to simulate other correlated quantum phases, such as magnetic phases. Many proposals suggest using an internal degree of freedom of the atoms to simulate a spin degree of freedom. Virtual hopping processes then lead to an effective magnetic interaction called superexchange. The energy scale of those processes is still low compared to experimentally reachable temperatures, and so magnetic long range order has not yet been observed.

An important milestone was recently reached taking a surprising new route: An equilibrium quantum phase transition of an antiferromagnetic spin chain was simulated using spinless bosons in a non-equilibrium situation. Starting with a one dimensional array of ^{87}Rb atoms in an optical lattice, an additional potential gradient[1] ('tilt') drove the transition to a state with density wave order. This happened in a metastable state, which is *not* the ground state of the full bosonic hamiltonian. However, the dynamics of the tilted lattice was confined to

---

[1]Experimentally the tilt is realized by a magnetic field gradient.
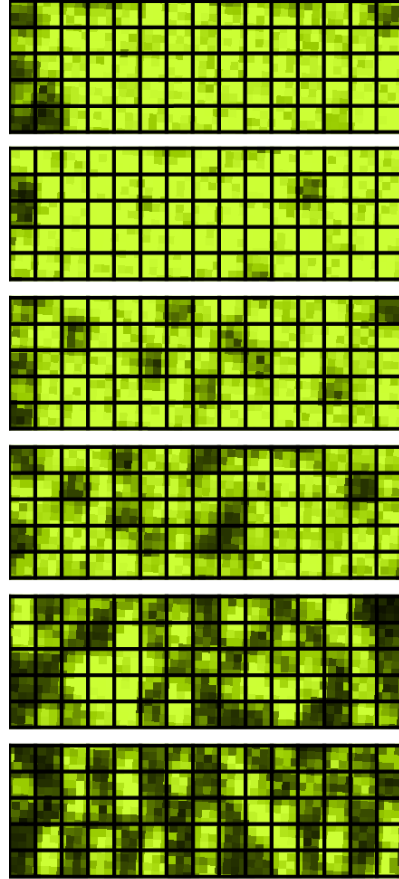
Figure 1.1: Snapshots of an experimental simulation of an antiferromagnetic Ising spin chain in longitudinal and transverse magnetic field taken by the Greiner group; see Ref. [3, 4]. The chains are aligned in longitudinal direction, and each image shows five independent chains. Tunneling of atoms in vertical direction is surpressed. Images were taken with a Quantum Gas Microscope [5, 6] for different strength of the tilt. First image is for weakest tilt, last image for strongest tilt. Experimentally the tilt is realized by a magnetic field gradient. A dark site corresponds to having no atom on that site, a bright site corresponds to either one or two atoms. See Chapter 2 for a more detailed discussion of this transition. Images courtesy Greiner group.

a resonantly connected effective subspace, which has an energy bounded from below [3, 7], and so a mapping to an antiferromagnetic Ising model in a transverse and longitudinal field is possible. Understanding *non-equlibirium* properties helped simulating *equilibrium* physics of a model with different degrees of freedom. The idea to drive a system, which can be prepared in the lab, *out of equilibrium* in order to simulate *equilibrium* properties of a previously inaccessible model with different degrees of freedom, is a new tool in the toolbox of ultracold atoms as analogue quantum simulators. Fig. 1 shows and absorption images for several tilt magnitudes taken by the Greiner group.

In two dimensions there are of course more knobs to turn, allowing for a larger variety of models that can be simulated. We can use different lattice geometries, and in addition to tuning the tilt magnitude, we can also change the tilt angle. In Chapter 2 we will show that, for example, two dimensional Ising order appears in a square lattice tilted into a non-equilibrium state; and that other lattices lead to intriguing models, as quantum dimer models and frustrated Ising antiferromagnets. In Chapater 3 we will analyze a particular lattice configuration in detail, and discuss its quantum phase transitions as a function of tilt angle and tilt magnitude.

Chapter 2

Metastable Phases of Tilted Two Dimensional Mott Insulators

We study the 'tilting' of Mott insulators of bosons into metastable states. These are described by Hamiltonians acting on resonant subspaces, and have rich possibilities for correlated phases with non-trivial entanglement of pseudospin degrees of freedom encoded in the boson density. We extend a previous study (Phys. Rev. B **66**, 075128 (2002)) of cubic lattices to a variety of lattices and tilt directions in 2 dimensions: square, decorated square, triangular, and kagome. For certain configurations three-body interactions are necessary to ensure that the energy of the effective resonant subspace is bounded from below. We find quantum phases with Ising density wave order, with superfluidity transverse to the tilt direction, and a quantum liquid state with no broken symmetry. The existence of the quantum liquids state is shown by an exact solution for a particular correlated boson model. We also find cases for which the resonant subspace is described by effective quantum dimer models.

2.1 Introduction

The observation of the superfluid-insulator quantum phase transition of ultracold bosonic atoms in an optical lattice [2] has launched a wide effort to engineering other correlated quantum states of trapped atoms. Much of the effort has focused on entangling the spin quantum number of the atoms between different lattice sites: superexchange interactions between neighboring lattice sites have been observed [8], but longer range spin

4

correlations have not yet been achieved.

Here we focus on a proposal [7, 9] to obtain quantum correlated phases in a pseudospin degree of freedom which measures changes in boson number across the links of a tilted lattice [10]. The interactions which entangle the pseudospins are not suppressed by factors of t/U (where t is the tunneling between lattice sites, and U is the local boson repulsion), and so non-trivial entanglement is likely to be readily accessible [3]. This proposal takes advantage of the unique feature of ultracold atom systems, namely, the ability to study many-body non-equilibrium physics [3, 11, 12, 13, 14], and suggests that various intriguing phases can appear as metastable states. Moreover, the recent advent of site-resolved imaging of ultracold atoms in optical lattices [5, 6, 15] opens the way to the direct detection of the pseudospin and the investigation of its quantum correlations.

The previous theoretical work on tilted lattices [7, 9, 16] focused on simple cubic lattices in spatial dimensions $d = 1, 2, 3$, with the tilt along one of the principal cubic axes. In $d = 1$, this theory predicted Ising density wave order for strong tilt, and this has been observed in recent experiments [3]. Here, we will study a variety of other lattices and tilt directions. We will find analogs of the density wave and anisotropic superfluid phases found earlier. However we will also find new quantum liquid states, and some cases which map onto the quantum dimer model. These states entangle the displacements of all the atoms, and so should be attractive targets of future experiments. We will find an exact liquid ground state for a particular correlated boson model.

We begin by recalling the Hamiltonian of a tilted Mott insulator. It is described by the generalized bosonic Hubbard model [17] with an additional potential gradient along a certain direction: $H = H_{\text{kin}} + H_{\text{U}} + H_{\text{tilt}}$:

$$H_{\text{kin}} = -t \sum_{<ij>} \left(\hat{b}_i^\dagger \hat{b}_j + \hat{b}_j^\dagger \hat{b}_i \right) \tag{2.1}$$

$$H_{\text{U}} = \frac{U}{2} \sum_i \hat{n}_i(\hat{n}_i - 1) + \frac{U_3}{6} \sum_i n_i(n_i - 1)(n_i - 2) + \dots \tag{2.2}$$

$$H_{\text{tilt}} = -E \sum_i \mathbf{e} \cdot \mathbf{r}_i \, \hat{n}_i. \tag{2.3}$$

Here $\hat{b}_i$ are canonical boson operators on lattice sites i at spatial co-ordinate $\mathbf{r}_i$, and $\hat{n}_i \equiv \hat{b}_i^\dagger \hat{b}_i$. The first term in H_{U} describes two body interactions. The second term is an effective three body interaction, generated by virtual processes involving higher bands [18, 19]. Such a term is present in ultracold atomic systems, as has recently been measured [18, 19, 20].

As we will show, the presence of this term dramatically changes the physics of tilted two dimensional lattices, therefore we include it in our model. The potential gradient is E, and the fixed vector $\mathbf{e}$ is normalized so that the smallest change in potential energy between neighboring lattice sites has magnitude E. We will assume a filling of one atom per site in the parent Mott insulator in most of the following discussion.

We are interested in the dynamics of the resonant subspace that appears when the lattice is tilted so that E becomes of order U. Specifically, we will work in the limit

$$|\Delta|, t \ll E, U, \tag{2.4}$$

where we define

$$\Delta = U - E. \tag{2.5}$$

We also define our tuning parameter

$$\lambda \equiv \frac{\Delta}{t}, \tag{2.6}$$

and allow λ to range over all real values. Thus we include processes which carry energy denominators of order $U - E$ to all orders, but neglect processes which have energy denominators of order U or E.

Let us now review the properties [7] of a tilted chain of sites in $d = 1$; see Fig. 2.1. As explained in Ref. [7], the limit Eq. (2.4) defines a strongly interacting many-body problem in the resonant subspace, which can be described by an effective Hamiltonian. Unlike the underlying Hubbard model in Eq. (2.3), the energy of this effective Hamiltonian is bounded from below, and it makes sense to study its stable ground state and low-lying excitations by the traditional methods of equilibrium many body theory. This will help us describe the dynamics of experimental studies in the metastable resonant subspace of the full Hubbard model in Eq. (2.3) defined by Eq. (2.4). It was found that the resonant subspace was described by a quantum Ising model for an Ising pseudospin residing on the links of the chain: an up spin represented the transfer of an atom across the link (or the creation of a dipole particle-hole pair), while the down spin had no change from the parent Mott insulator. In other words, in a parent Mott insulator with occupancy n_0 per site, a down spin was a pair of sites with occupancy (n_0, n_0), while an up spin was $(n_0 - 1, n_0 + 1)$. The Ising model had both a longitudinal and transverse external field, representing the energy of the dipole and the tunneling amplitude of the atom respectively. However, two nearest neighbor dipoles cannot be created simultaneously, and this implied the presence of infinitely
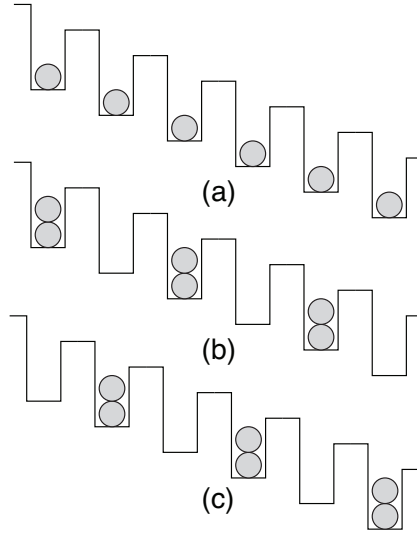
Figure 2.1: (a) Parent Mott insulator, which is the ground state for $\lambda \to \infty$. (b,c) Ground states with Ising density wave order for $\lambda \to -\infty$.

strong nearest-neighbor *antiferromagnetic* exchange interactions. It is this infinitely strong exchange which allows easy access to strong-correlation physics in such tilted lattices [3]. The phase diagram of the Ising antiferromagnet with both longitudinal and transverse fields has also been studied by others, [21, 22] with different physical motivations. For $\lambda \to \infty$, the Ising model had a paramagnetic ground state, corresponding to configurations close to the parent Mott insulator. In contrast for $\lambda \to -\infty$, the Ising model had antiferromagnetic long-range order, corresponding to a maximum density of particle-hole pair excitations about the Mott insulator. There are two possible ways of arranging these excitations, depending upon whether the particles reside on the odd or even sites, and this ordering is linked to the antiferromagnetic order of the Ising model. In between these limit cases, a quantum phase transition was found [7] at an intermediate value of λ: this transition was in the universality class of the quantum Ising *ferromagnet* in a transverse field and zero longitudinal field [21, 22, 7].

Next, let us review [7] cubic lattices in dimensions $d > 1$, with a tilt along a principal lattice axis, with $|U_3| \gg t$. Then we have to distinguish the physics parallel and transverse to the tilt direction. Parallel to the tilt direction, the physics is similar to $d = 1$: there is an Ising density wave order associated with dipolar particle-hole pairs, which turns on as λ decreases. In contrast, transverse to the tilt direction, the quantum motion of in-

dividual particles and holes is allowed, not just of dipole bound states. Such motion raises the possibility of Bose condensation of particles/holes and of the appearance of superfluidity. However, the single particle or hole motion is constrained to be purely transverse. Consequently there are an infinite number of conservation laws, one for each lattice layer orthogonal to the tilt direction: the total number of particles in any layer is constrained to equal the total number of holes in the preceding layer. Because of these conservation laws, the superfluidity is not global, but restricted to each transverse layer separately: there is no Josephson tunneling term which links the superfluid order parameter of adjacent layers. Of course, because of the translational symmetry in the effective Hamiltonian parallel to the tilt, the superfluidity appears simultaneously in all the layers. In this superfluid state, atomic motion is insulating parallel to the tilt, and superfluid transverse to the tilt. Such transverse-superfluid states also appear as λ decreases, and can co-exist with the Ising order parallel to the tilt. The previous work [7] did not note the U_3 term, even though its presence is required for the applicability of the $d > 1$ dimensional results therein.

In the present Chapter we will examine several tilted two dimensional lattices. We find that the physics not only depends on the lattice geometry and tilt direction, but also on the magnitude of U_3 compared to other energy scales of the systems. This U_3 term is needed to guarantee the stability of some lattices, as for example the cubic lattices reviewed above. The reason is the following. Let us assume a parent Mott insulator with filling $n_0 = 1$. Processes of the kind $(1, 1) \rightarrow (0, 2)$ cost repulsion energy U, and gain tilt-energy E (if the two participating sites differ in potential energy E). These processes are tuned to be resonant. Depending on the lattice structure, it may then happen that two sites differing in potential E are each occupied by two bosons. The process $(2, 2) \rightarrow (1, 3)$ costs repulsion energy $U + U_3$, and gains potential energy E. In the case $|U_3| \gg t$ this process is off-resonant. We can then identify a resonant subspace which focuses on the $(1, 1) \rightarrow (0, 2)$ processes only. This was implicitly assumed in Ref. [7] without discussion of the crucial role played by U_3, and will be assumed in our Sections 2.2-2.4. In such cases, our effective Hamiltonian[1] method applies, the energy of the resonant subspace is bounded from below, and we can use equilibrium methods to study the phase diagrams.

---

[1]It is worth noting here that these effective Hamiltonians always have full translational symmetry both parallel and transverse to the tilt directions, unlike Eq. (2.3) which is only invariant under translations transverse to the tilt. Of course, there is no equivalence between the physics parallel and transverse to the tilt direction, and the lattice rotation symmetry is reduced by the tilt, even in the effective Hamiltonian.

On the other hand, if $|U_3| \lesssim t$, we cannot neglect processes of the type $(2, 2) \rightarrow (1, 3)$. In the presence of such processes, the resonant Hilbert space is increased. This can have dramatic consequences on the physics; in some cases, we find that the energy in the resonant subspace becomes unbounded from below, and the system becomes unstable.

The present Chapter will examine several lattice configurations of Eq. (2.3) in $d = 2$. We will assume $|U_3| \gg t$ in all cases, except in Section 2.5. We will find analogs of the Ising and transverse-superfluid phases described above in these lattices. However, we will also find a qualitatively new phenomenon: the appearance of quantum liquid ground states with no broken symmetries. These phases appear in these lattices for two main reasons. First, even for a large tilt, not all the sites can participate in the creation of particles or holes due to the geometrical constraints present in these lattice configurations. Such geometrical constraints generate exponentially large degenerate states in the limit of infinite tilt. Secondly, the lattice structure ensures that there is no free motion of unbound particles or holes in the direction transverse to the tilt in the resonant subspace. The absence of such unbound motion prevents transverse-superfluidity, allowing for the appearance of the quantum liquid states.

The outline of the remainder of the Chapter is as follows. In Section 2.2 we study a square lattice with a tilt in a diagonal direction, while in Section 2.3 we study a triangular lattice with different tilt directions. In these cases, we will find analogs of phases studied previously, involving Ising density wave and transverse-superfluid order. In Section 2.4, we will consider the kagome and certain decorated square lattices. Here, the transverse-superfluid order is suppressed for certain tilt directions, and novel quantum liquid ground states appear. Also, for another tilt direction on the kagome, the Ising density wave order is suppressed, and we obtain effective decoupled one dimensional systems. In Section 2.5, we briefly discuss the $U_3 = 0$ case.

2.2 Square lattice

As noted in Section 2.1, this section always assumes $|U_3| \gg t$. We have already reviewed the results of Ref. [7] for a square lattice tilted along a principle lattice direction. Ref. [7] also briefly considered a tilt along a diagonal lattice direction, and we will discuss this case more completely in the present section.

For the diagonal tilt, we choose the vector $\mathbf{e} = (1, 1)$ in the Hubbard model in
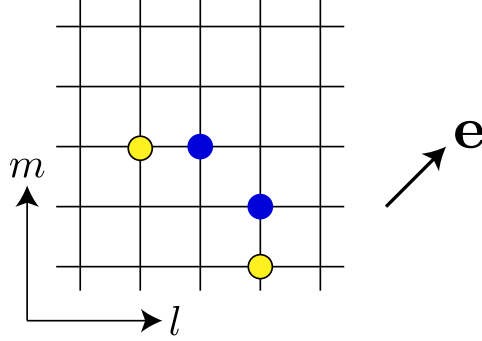
Figure 2.2: Full blue circles denote quasiparticles, and black circles with light yellow filling denote quasiholes. The tilt vector is $\mathbf{e} = (1,1)$ and the resonant particle-hole excitations are as shown in the figure.

Eq. (2.3). In this situation each site has two neighbors to which resonant tunneling is possible; see Fig. 2.2. Here and in the following, we label the lattice sites as (l, m) where l (m) represents the x (y) coordinate, respectively. Using the methods of Ref. [7], the Hamiltonian of the resonant subspace can be written as

$$H_{ph} = -t\sqrt{n_0(n_0+1)} \sum_{lm} \left[\left(\hat{p}^\dagger_{l(m+1)} + \hat{p}^\dagger_{(l+1)m} \right) \hat{h}^\dagger_{lm} + \text{H.c.} \right] + \frac{\Delta}{2} \sum_{l,m} \left(\hat{p}^\dagger_{lm}\hat{p}_{lm} + \hat{h}^\dagger_{lm}\hat{h}_{lm} \right).$$

$$(2.7)$$

Here we have introduced bosonic quasiparticles $\hat{p}^\dagger_{lm}$ and quasiholes $\hat{h}^\dagger_{lm}$, and we identify the parent Mott insulator with filling n_0, $|Mn_0\rangle$, as quasiparticle and quasihole vacuum, $|0\rangle$, and so

$$\hat{p}^\dagger_{l,m} |0\rangle \quad := \quad \frac{1}{\sqrt{n_0+1}} \hat{b}^\dagger_{l,m} |Mn_0\rangle, \qquad (2.8)$$

$$\hat{h}^\dagger_{l,m} |0\rangle \quad := \quad \frac{1}{\sqrt{n_0}} \hat{b}_{l,m} |Mn_0\rangle. \qquad (2.9)$$

These operators are hard-core bosons and so we have the constraints

$$\hat{p}^\dagger_{l,m}\hat{p}_{l,m} \quad \leq \quad 1, \qquad (2.10)$$

$$\hat{h}^\dagger_{l,m}\hat{h}_{l,m} \quad \leq \quad 1, \qquad (2.11)$$

$$\hat{p}^\dagger_{lm}\hat{p}_{lm}\hat{h}^\dagger_{lm}\hat{h}_{lm} \quad = \quad 0. \qquad (2.12)$$

We are now interested in describing the global ground state of the effective Hamiltonian in Eq. (2.7) while it is subject to the constraints in Eqs. (2.2). It is useful to first consider the limits of $\lambda \to \infty$ and $\lambda \to -\infty$, followed by a general discussion.
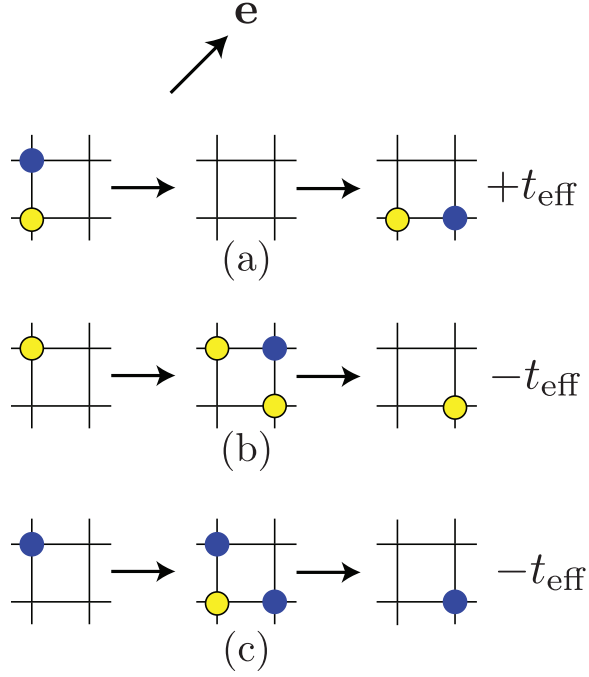
Figure 2.3: The matrix elements for the above processes are $+t_{\mathrm{eff}}$ for process (a), and $-t_{\mathrm{eff}}$ for (b) and (c).

2.2.1 Limit $\lambda \to \infty$

To zeroth order in $1/\lambda$, the unique ground state is the vacuum, the parent Mott insulator. All particle-hole excitations are gapped with the same energy (see Fig. 2.2), $E_1 = \Delta$. At second order in $1/\lambda$, we obtain an effective Hamiltonian for particles and holes, whose structure is strongly constrained by Eq. (2.2). A number of distinct processes appear in the perturbation theory:

- Overall energy shift due to virtual processes. The vacuum couples to all states with one neighboring particle-hole pair, and so the vacuum energy is shifted down. Each particle-hole state couples to zero and two particle-hole states. To second order the energy E_0 for the vacuum and E_1 for states with one particle hole pair are:

$$E_0 \;=\; -2N\frac{t^2}{\Delta}n_0(n_0+1), \tag{2.13}$$

$$E_1 \;=\; = \Delta - (2N-8)\frac{t^2}{\Delta}n_0(n_0+1). \tag{2.14}$$

where N is the number of lattice sites.

- Hopping of particles and holes along direction transverse to the tilt: Particles and holes can hop *individually* via second order processes along lines which are orthogonal to the tilt direction, see Fig. 2.3b,c. The magnitude of the effective hopping is

$$t_{\text{eff}} = \frac{t^2 n_0(n_0 + 1)}{|\Delta|}. \tag{2.15}$$

It is this process which leads to transverse superfluidity. Of course, because the superfluidity is now one-dimensional, it is only quasi-long range, and characteristic of a Luttinger liquid.

- When particles and holes are proximate to each other, we should consider their hopping as contributing to the hopping of a dipole particle-hole pair. One such process is shown in Fig. 2.3a, and it leads to the motion of a particle (or rotation of a dipole) with matrix element opposite to that without an adjacent hole.

Collecting these processes, we can write down an effective Hamiltonian in the manifold of excited states with one particle hole pair (with energy $\approx \Delta$). We label (l_p, m_p) the position of the quasiparticle, and (l_h, m_h) the position of the hole. Clearly the vacuum state only couples to states where particle and hole are on neighboring transverse diagonals, so that $m_p + l_p = m_h + l_h + 1 = d$. We only need three integers to describe the positions of particle and hole: d, m_p, m_h. We label the states by

$$|d, m_p, m_h\rangle = \hat{p}^\dagger_{d-m_p,m_p} \hat{h}^\dagger_{d-m_h-1,m_h} |0\rangle \tag{2.16}$$

and the effective Hamiltonian in this manifold is

$$
\begin{aligned}
H_{\text{ph, eff}} = E_1 + t_{\text{eff}} \sum_{d,m} & \Big[\left(|d, m, m\rangle + |d, m, m - 1\rangle\right) \left(\langle d+1, m, m| + \langle d+1, m+1, m|\right) \\
& + |d, m, m\rangle \langle d, m+1, m| + |d, m, m\rangle \langle d, m, m-1| + \text{H.c.} \Big] \\
- t_{\text{eff}} \sum_{d, m_p \neq m_h} & \Big[|d, m_p, m_h\rangle \langle d, m_p + 1, m_h| + |d, m_p, m_h\rangle \langle d, m_p, m_h - 1| + \text{H.c.} \Big]. \tag{2.17}
\end{aligned}
$$

Here the first sum is for hopping of particle-hole pairs, both in transverse and longitudinal direction of the tilt. The second sum is for particles and holes hopping individually in transverse direction. Diagonalization of this Hamiltonian, as in Ref. [7], yields a continuum of separated particle-hole excitations, along with a dipolar particle-hole bound state.
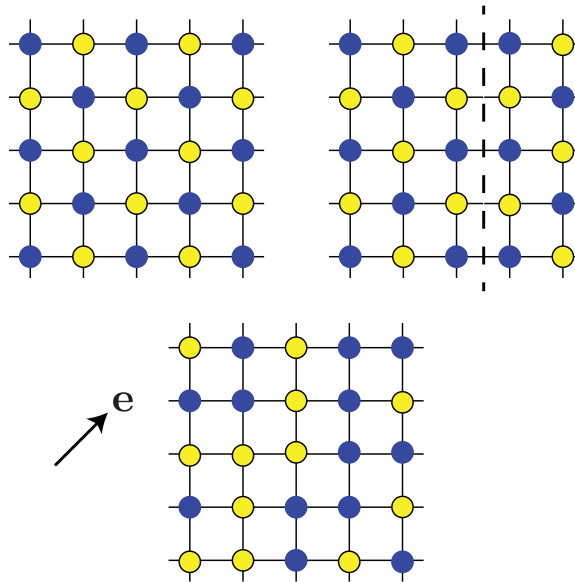
Figure 2.4: $\lambda \to -\infty$: Three possible states with maximum dipole density. At zeroth order in $1/|\lambda|$, these states are degenerate, along with an infinite number of other state with the same dipole density. At second order in $1/|\lambda|$, two states are selected as the global ground states: the checkboard state on the top-left, and its symmetry-related partner. The state in the top-right has a domain wall between the two checkerboard states: the domain wall costs energy $t^2/(2|U - E|)$ per unit length.

2.2.2 Limit $\lambda \to -\infty$

At zeroth order in $1/|\lambda|$ there are an infinite number of degenerate ground states, all maximizing the number of particle-hole pairs. Three such states are shown in Fig. 2.4. In Ref. [7], it was stated that these degenerate ground states can be labelled by the set of dimer coverings of the square lattice: this is incorrect, because given a set of particle and hole configurations, there is, in general, no unique assignment of them into nearest-neighbor dipoles.

We can examine the lifting of the ground state degeneracy in a perturbation theory in $1/|\lambda|$. At leading order, the matrix elements in the ground state subspace are all diagonal. Each particle that has one hole to the left or below, can undergo a virtual annihilation, reducing the energy by $(t^2/|\Delta|)n_0(n_0 + 1) = t_{\text{eff}}$. If it has two neighbors that are holes (left and below) it can do two virtual hopping processes, reducing its energy by $2t_{\text{eff}}$. Thus we should optimize the latter configurations: this leads to two degenerate ground states, which look like checkerboards. These states break a lattice translation symmetry, and there is an

Ising order parameter.

2.2.3   Discussion

The basic phenomenology that has emerged from our discussion so far of the diagonal tilted square lattice is quite similar to that for the principal axis tilt considered in Ref. [7]. For $\lambda \to \infty$, we have continua of particle-hole excitations, while for $\lambda \to -\infty$ we have a state with Ising density wave order,

and domain wall excitations. While for the principal axis tilt, these results appeared already at first order in $1/|\lambda|$, here for the diagonal tilt case we had to go to order $1/\lambda^2$ to obtain the free hopping of particles and holes, and the appearance of the Ising order. We don't expect these distinctions to be important at smaller values of $|\lambda|$, and so the phase diagram of the diagonal tilt case should be similar to that of the principal axis tilt: Ising order appearing as λ decreases, along with transverse quasi-superfluidity at intermediate values of λ.

2.3   Triangular lattice

As in Section 2.2, this section also assumes $|U_3| \gg t$. The triangular lattice case is very similar to the square lattice case. The phase transitions are to Ising density-wave ordered states and possibly transverse quasi-superfluid phases. The tilt breaks the rotation symmetry, so the dipole states on the tilted triangular lattice are not frustrated.

2.3.1   Tilt along a principal lattice direction

For the tilt along a lattice direction, e.g. $\vec{a}_1$, we choose the tilt magnitude so that the creations of dipoles along the two other lattice directions, $\vec{a}_2$ and $\vec{a}_3$, are resonant (see Fig. 2.5a) but the dipole creation along the direction $\vec{a}_1$ is *not*. Therefore, the effective Hamiltionian in the resonant subspace for this case is the same as for the square lattice with a diagonal tilt, and all conclusions from Section 2.2 apply here.

One could also choose the tilt magnitude so that processes along $\vec{a}_1$ are resonant. Then all processes along $\vec{a}_2$ and $\vec{a}_3$ are off-resonant, and the resonant subspace separates into decoupled one-dimensional systems.
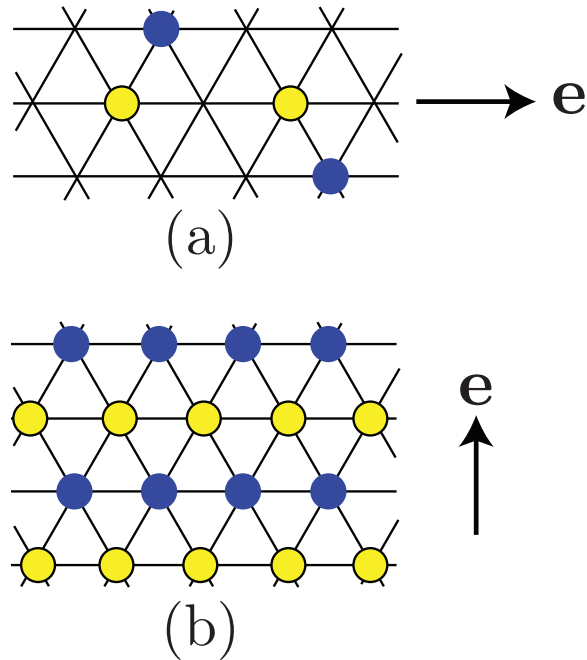
Figure 2.5: (a) Triangular lattice tilted along principal lattice direction. The effective Hamiltonian of the resonant subspace for this system is the same as the one for a square lattice with diagonal tilt. Full blue circles denote quasiparticles, and black circles with yellow filling denote quasiholes. (b) Triangular lattice tilted perpendicular to a principal lattice direction. For large negative λ, there are two-fold degenerate ground states with broken lattice symmetry.

2.3.2   Tilt perpendicular to a principal lattice direction

Here we briefly consider a triangular lattice with tilt along a principal direction. In the limit $\lambda \to \infty$, the ground state is the parent Mott insulator and all excitations are gapped. Particles and holes can separate and hop along the axis transverse to the tilt direction and reduce their kinetic energy.

On the other hand, for large and negative λ, there are precisely two degenerate ground states, as illustrated in Fig. 2.5b. There is an Ising density wave order parameter associated with these states. These states and their symmetries are similar to those found for the tilted square lattice in Ref. [7], and a similar phase diagram is expected.

2.4   Decorated square and kagome lattices

As in Sections 2.2 and 2.3, this section also assumes $|U_3| \gg t$. We will now consider frustrated models in the sense that in the strongly tilted limit, $\lambda \to -\infty$, not all sites can participate in dipole creation. This requires lattices with a larger unit cell, as will become clear from our discussion. Furthermore, the tilt direction of those lattices can be chosen such that independent motion of particles and holes is not possible in the resonant subspace. We can then label the resonant subspace by a set of dipole coverings. In the limit $\lambda \to -\infty$, we will obtain a large degeneracy in the dense dipole states. This degeneracy is lifted by corrections in inverse powers of $|\lambda|$. The leading corrections are not diagonal in the basis of dipole coverings: this sets up the possibility for novel quantum liquid phases.

2.4.1   Decorated square lattice with a diagonal tilt

Here we consider a decorated square lattice tilted along a diagonal direction, as illustrated in Fig. 2.6a. We define the distance between nearest-neighbor sites to be a so that the unit cell of the square lattice in Fig. 2.6a has size $2a$.

Interestingly, the effective Hamiltonian for the resonant subspace resulting from the tilted kagome lattice shown in Fig. 2.6b is the same as the one obtained in the decorated square lattice in Fig. 2.6a. While the geometry of the kagome lattice is different from the decorated square lattice, for the specific tilt of Fig. 2.6b, dipoles cannot be resonantly created along the links parallel to the tilt direction. This reduces the geometry of the tilted kagome to the tilted decorated square lattice. Using this identity, we will present most of
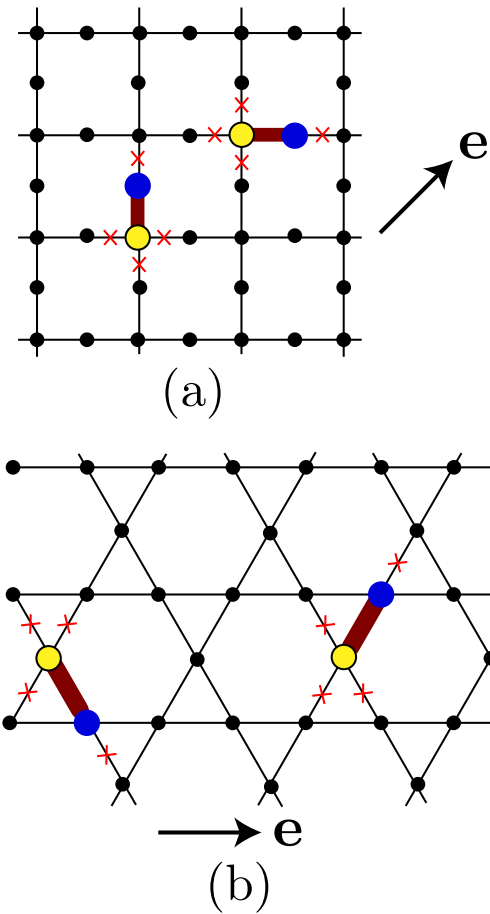
Figure 2.6: (a) Decorated square lattice in diagonal tilt, and (b) kagome lattice with tilt along lattice direction, where the tilt strength is chosen so that only processes along the diagonal lines are resonant. These two models lead to the same effective Hamiltonian in the resonant subspace. Excitations of the parent Mott insulator are dipoles (shown as think lines connecting quasiparticle and quasihole). The particles and holes cannot separate. Each dipole link blocks four other links from forming dipoles (shown as crosses). Those are also the four links onto which each dipole is allowed to hop through virtual processes.

the results using the decorated square lattice illustrated in Fig. 2.6a.

The decorated square lattice has 3 sites per unit cell. Let N be the number of unit cells, and we assume periodic boundary conditions. There are two kinds of sites on this lattice: N sites that have four neighbors, and $2N$ sites that only have two neighbors. We define the unit cell so that a site with four neighbors is in its center. We will refer to these sites as central sites.

The Hamiltonian in the resonant subspace is

$$H = \Delta \sum_a \hat{d}_a^\dagger \hat{d}_a - t\sqrt{n_0(n_0 + 1)} \sum_a \left(\hat{d}_a + \hat{d}_a^\dagger \right), \tag{2.18}$$

where a labels the lattice links, and $\hat{d}_a^\dagger$ creates a dipole on this link. The resonant subspace has the constraints

$$\hat{d}_a^\dagger \hat{d}_a \leq 1, \tag{2.19}$$

and

$$\hat{d}_a^\dagger \hat{d}_a \hat{d}_{a'}^\dagger \hat{d}_{a'} = 0 \tag{2.20}$$

if a and a' share a lattice site, see Fig. 2.6. Note that particles and holes cannot separate on this lattice through hopping in the resonant subspace. It is notable that this effective model restores the rotational symmetry of the lattice and is symmetric under rotation of $\pi/2$ around the central sites.

Limit $\lambda \to \infty$

Here the ground state is the parent Mott insulating state. The excitations are gapped and the lowest excitations are given by the creation of a single dipole. To zeroth order in $1/\lambda$, all states with one dipole are degenerate. We now describe the effective Hamiltonian for the manifold of excited states with energy $\approx \Delta$ to second order in $1/\lambda$. First of all, there are energy shifts for the vacuum energy E_0 and energy of one dipole E_1, given by

$$E_0 = -4Nt_{\text{eff}} \tag{2.21}$$
$$E_1 = \Delta - (4N - 6)t_{\text{eff}} \tag{2.22}$$

with

$$t_{\text{eff}} = \frac{t^2 n_0(n_0 + 1)}{|\Delta|}. \tag{2.23}$$
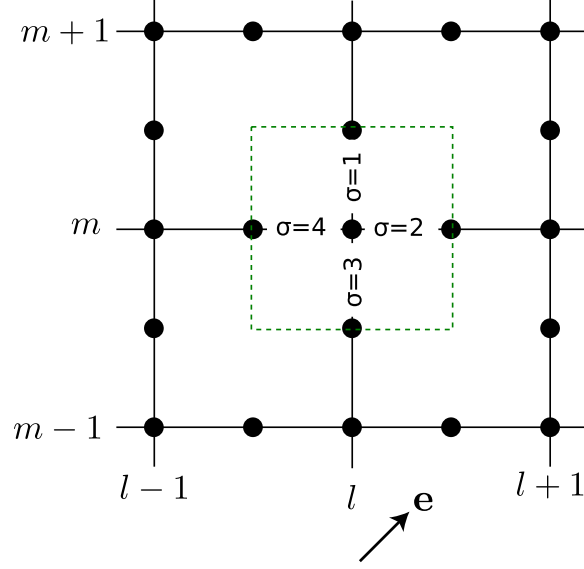
Figure 2.7: Labeling of sites and links on the decorated square lattice.

Additionally, second order processes lead to hopping of the dipoles. Note that a dipole always involves one central site and one neighboring site located to the right, left, up or down relative to the central site. Thus, we label the dipole states by $|l, m, \sigma\rangle$, where (l, m) denotes the position of the central site and $\sigma = 1, 2, 3, 4$ indicates the direction of the dipole, see Fig. 2.7. With this notation, the effective Hamiltonian for one dipole excitation is given by

$$
\begin{aligned}
H_{1\text{dimer}} \;=\; & E_1 + t_{\text{eff}} \sum_{\sigma \neq \sigma', m, l} |l, m, \sigma\rangle \langle l, m, \sigma'| \\
& + t_{\text{eff}} \sum_{l, m} \left[|l, m, 1\rangle \langle l, m+1, 3| + |l, m, 2\rangle \langle l+1, m, 4| + \text{H.c.} \right]. \quad (2.24)
\end{aligned}
$$

The first sum represents hopping of the dipole at a central site from one orientation to another, and the second sum represents hopping from one unit cell to another. Diagonalizing the above Hamiltonian Eq. (2.24), one obtains the spectra of a single dipole excitation given

by

$$\epsilon_1(k_x, k_y) = E_1 - 2t_{\text{eff}} \tag{2.25}$$

$$\epsilon_2(k_x, k_y) = E_1 \tag{2.26}$$

$$\epsilon_3(k_x, k_y) = E_1 + \left(1 - \sqrt{5 + 2\cos(2ak_x) + 2\cos(2ak_y)}\right) t_{\text{eff}} \tag{2.27}$$

$$\epsilon_4(k_x, k_y) = E_1 + \left(1 + \sqrt{5 + 2\cos(2ak_x) + 2\cos(2ak_y)}\right) t_{\text{eff}} \tag{2.28}$$

where $2a$ is the distance between two neighboring central sites. The first two bands are 'flat bands' as they do not depend on momentum.

Limit $\lambda \to -\infty$, quantum liquid state

Exact solution for $\lambda \to -\infty$. To zeroth order in $1/\lambda$, all states which maximize the number of dipoles are degenerate, and they are all ground states of the effective Hamiltonian. These states require every central site on the square lattice to have a dipole (on the kagome lattice, every site marked with a square has a dipole), as illustrated in Fig. 2.8. There is an exponentially large number of such states which satisfy this requirement.

To second order in $1/|\lambda|$, dipoles can hop as long as the constraint Eq. (2.20) is satisfied. As there is a dipole on every central site, the constraint implies that dipoles may only change their orientation while remaining at the same central site. Thus, we can write the hopping of the dipoles as a 4-state quantum clock model, with the clocks residing on the vertices of the square lattice. The hopping Hamiltonian can be written as (see Fig. 2.8)

$$
\begin{aligned}
H_{\text{clock}} &= \sum_{lm} H_{l,m} \\
H_{l,m} &= \Delta - t_{\text{eff}}(|1\rangle + |2\rangle + |3\rangle + |4\rangle)(\langle 1| + \langle 2| + \langle 3| + \langle 4|) \tag{2.29}
\end{aligned}
$$

where (l, m) is the site index, and $|\sigma\rangle$ is a shorthand for $|l, m, \sigma\rangle$ representing the orientation of the dipole sitting at (l, m). It should be remembered that states within the resonant subspace have the important constraint that two dipoles sitting at neighboring central sites cannot be directed toward each other. Such constraints are not contained in H_{clock}. If we define the projection operator onto the resonant subspace which satisfies the constraints as P, the effective Hamiltonian with the constraints is given by projecting the hopping Hamiltonian,

$$H^c_{\text{clock}} = P H_{\text{clock}} P. \tag{2.30}$$
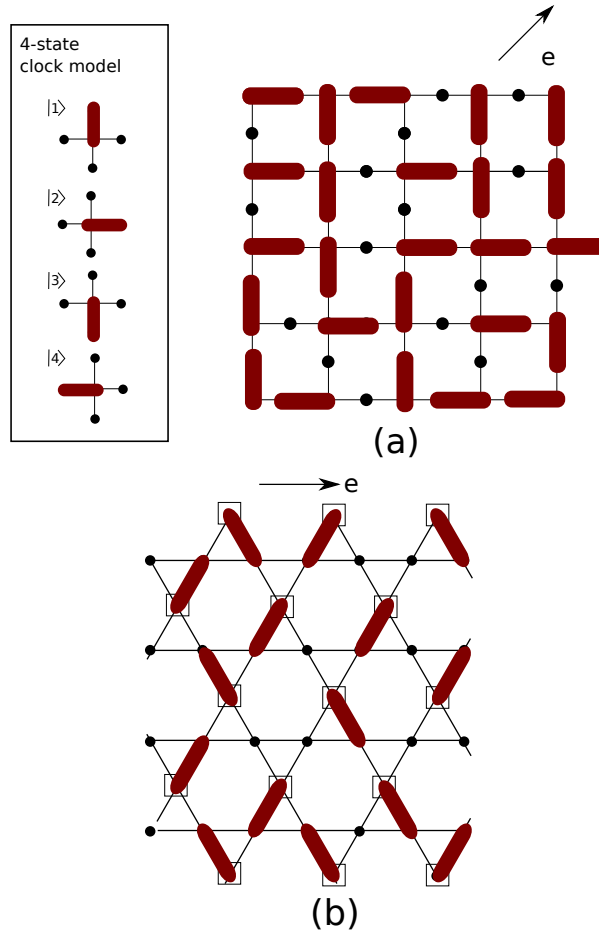
Figure 2.8: $\lambda \to -\infty$: quantum 4-state clock model: (a) decorated square lattice, (b) kagome lattice. Both lattices lead to the same effective Hamiltonian. Minimum of the energy for the effective Hamiltonian is obtained when the number of dipoles is maximum. This requires, on the square lattice, every central site to have a dipole, and on the kagome lattice, every site marked with a square to have a dipole. As a result, we can look at the system in the limit $\lambda \to -\infty$ as a collection of four state clocks, one each on the central sites of the square lattice, or on the marked sites of the kagome. The states on neighboring clocks are constrained by the requirement that the dipoles cannot overlap.

In the following we will show that the *exact* ground state of the Hamiltonian with constraint H_{clock}^c is obtained through the projection of the ground state of the Hamiltonian without constraint, H_{clock}, onto the resonant subspace which satisfy the constraints Eq.(4.1). The ground state of the unconstraint single-site Hamiltonian $H_{l,m}$ is given by $|1\rangle + |2\rangle + |3\rangle + |4\rangle$ with eigenenergy $\Delta - 4t_{\text{eff}}$, and there are three degenerate excited states[2] with eigenenergy Δ. Therefore, the ground state of H_{clock} is given by

$$|\psi_0\rangle = \mathcal{N} \prod_{l,m}(|l,m,1\rangle + |l,m,2\rangle + |l,m,3\rangle + |l,m,4\rangle) \qquad (2.31)$$

where $\mathcal{N}$ is some normalization constant. As we will show in the following, the exact ground state of H_{clock}^c is given by

$$|\psi_c\rangle = P|\psi_0\rangle. \qquad (2.32)$$

Any configuration with maximum number of dipoles corresponds to a product state given by $\prod_{l,m}|l,m,\sigma_{l,m}\rangle$ where $\sigma_{l,m} = 1,2,3,4$. Then the state $|\psi_c\rangle$ is nothing but the equal superposition of all the product states in the resonance subspace in the limit $\lambda \to -\infty$ i.e. all the configurations with maximum number of dipoles.

The proof proceeds in two steps. First, we will show that this nodeless state $|\psi_c\rangle$ is an eigenstate of the Hamiltonian H_{clock}^c. Second, we will show that it is necessarily the unique ground state of the Hamiltonian H_{clock}^c.

In order to see that $|\psi_c\rangle$ is an eigenstate of H_{clock}^c, we check that $H_{\text{clock}}^c|\psi_c\rangle$ is again the equal superposition of all the configurations with maximum number of dipoles. Consider a particular configuration with maximum number of dipoles represented by the product state $|M\rangle$. We count how many different configurations in $|\psi_c\rangle$ produce $|M\rangle$ after the action of H_{clock}^c. This is equivalent to counting how many different state can be created from $|M\rangle$ through the action of H_{clock}^c. For any $|M\rangle$, there are in total $2N$ different configurations that are connected with $|M\rangle$ through an action of H_{clock}^c, where N is the total number of dipoles in the system. The decorated square lattice has in total $2N$ non-central sites, and in a configuration with maximum number of dipoles $|M\rangle$, N of them are part of a dipole and N of them are *not*. Now the action of H_{clock}^c is a change of the orientation of a dipole at a central site, and the action can change the configuration by hopping a

---

[2]Interestingly, it is possible to fill the lattice with these excited states while respecting the constraint: some of the highest energy eigenstates of H_{clock} are also eigenstates of H_{clock}^c. Note that states of the form $|\sigma\rangle - |\sigma'\rangle$, with $\sigma \neq \sigma'$, are excited eigenstates of the single site Hamiltonian (2.29). These states only occupy two links. We could, for example, fill the lattice with the state $|1\rangle - |2\rangle$ on every site.

dipole to these non-central sites that are not occupied by a dipole in $|M\rangle$. Since each unoccupied non-central site is connected with 2 central sites, there are in total $2N$ different configurations connected with $|M\rangle$. This consideration is true for any $|M\rangle$, so we conclude that $H^c_{\text{clock}} |\psi_c\rangle = N (\Delta - 3t_{\text{eff}}) |\psi_c\rangle$. Notice that the Hamiltonian Eq. (2.29) contains terms which bring a configuration back to itself, so the eigenenergy is $N (\Delta - 3t_{\text{eff}})$. Indeed $|\psi_c\rangle$ is an eigenstate.

Now we show that this state is necessarily the unique ground state. Note that if we take as the basis the product states which correspond to configurations with maximum number of dipoles, all the off-diagonal matrix element of H^c_{clock} are negative. Moreover, repeated applications of H^c_{clock} can connect any configuration with maximum number of dipoles to any other configurations with maximum number of dipoles. This statement is even true when the system is placed on a manifold with non-trivial topology, such as a torus. From these two conditions, it follows through Perron-Frobenius theorem [23, 24, 25] that the ground state of the effective Hamiltonian Eq. (2.29) is the superposition of product states with strictly positive amplitudes. Moreover, since two of such states cannot be orthogonal to each other, this ground state is unique. This statement is true for any finite system with doubly periodic boundary conditions. However, the above argument does not tell us anything about the scaling of the energy gap to the next lowest eigenvalues as a function of system sizes. Even though we know the exact ground state, the question of whether the system is gapped or gapless, and whether the ground state remains unique in the thermodynamic limit is still open[3] .

Correlation functions. In order to probe the properties of the ground state $|\psi_c\rangle$, we numerically computed correlations for the state in Eq. (2.32). For the correlations of local operators in a state which is the equal superposition of product states, the correlations can be related to the corresponding classical problem [26]. Here we study the density-density correlation $\langle \hat{n}_{0,0} \hat{n}_{0,m} \rangle$ on the central sites. $n_{l,m}$ is the density of the central site at (l, m) measured relative to the density of the Mott insulator, so that $n_{l,m}$ can, in principle, take

---

[3]By looking at Fig. 2.8 one might be tempted to compare this system to a loop model, for example by drawing lines following the direction of the dipoles from one central site to the next one. This leads to a model where lines may begin anywhere, they may never end (every dipole points to some site which also has a dipole on it), but lines may merge; and so ultimately every line ends in some loop. Acting upon any state with the Hamiltonian a single time can change the structure completely, and so this model seems not to be related to a loop model.
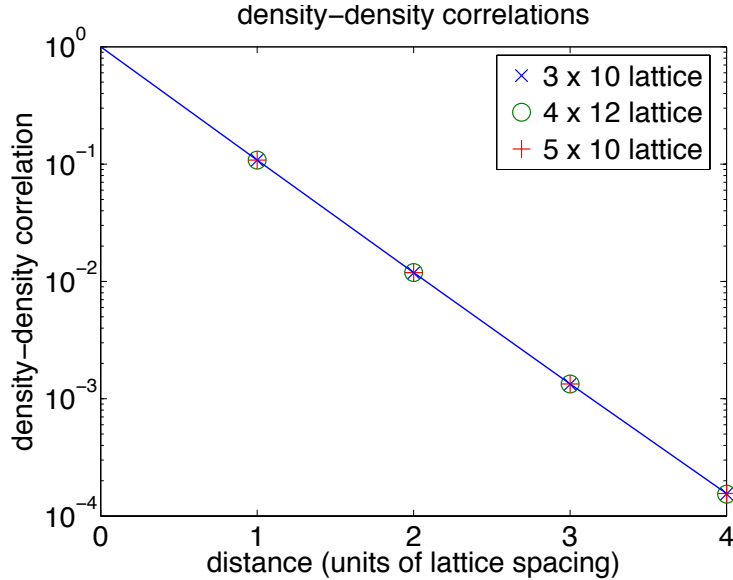
Figure 2.9: Density-density correlation function $\langle \hat{n}_{0,0} \hat{n}_{0,m} \rangle$ on the central sites (the ones marked by a square in Fig. 2.8), obtained using transfer matrices and periodic boundary conditions. Correlations decay rapidly in an exponential fashion. A fit to the exponential $f(m) = a \exp(-bm) + c$ gives $a = 0.9999$, $b = 2.225$, $c = 7.371 \times 10^{-5}$, this corresponds to a correlation length of less than half a lattice spacing.

the values $+1, 0, -1$. Here $+1$ (-1) means that there is an extra (a missing) boson on that lattice site, and that this site has formed a dipole with a neighbor below or to the left (above or to the right). $n_{l,m} = 0$ would mean that this central site is not participating in a dipole bond; in the limit $\lambda \to -\infty$ all central sites have $n_{l,m} = \pm 1$. We used row-to-row transfer matrices with rows of length up to 5 unit cells and periodic boundary conditions to compute density-density correlations [27]. Results for lattice sizes 3×10, 4×12, and 5×10 are plotted in Fig. 2.9. We obtain essentially the same results for different lattice sizes, and a fit of the correlation function to the exponential $f(m) = a \exp(-bm) + c$ gives $a = 0.9999$, $b = 2.225$, $c = 7.371 \times 10^{-5}$, corresponding to a correlation length of less than half a lattice spacing. Similarly, dipole-dipole correlations can also be calculated: let $\hat{d}_{\sigma,l,m}$ be an operator that projects onto states which have dipole orientation σ at site (l, m). We find that correlations $\langle \hat{d}_{\sigma,0,0} \hat{d}_{\sigma',l,m} \rangle - \langle \hat{d}_{\sigma,0,0} \rangle \langle \hat{d}_{\sigma',l,m} \rangle$ decay exponentially.

Discussion.   The exponential decay of the equal-time correlations suggests that the $\lambda \to -\infty$ liquid state has a gap to all excitations. Furthermore this liquid state is non-

degenerate on a torus, implying the absence of topological order, and we expect the ground state to remain unique in the thermodynamic limit $N \rightarrow \infty$. Thus there is a possibility that the parent Mott insulator state at $\lambda \rightarrow \infty$ is adiabatically connected to the liquid state at $\lambda \rightarrow -\infty$, without an intervening quantum phase transition.

Ultracold atom experiments are expected to realize this quantum liquid state as long as the temperature is lower than the energy scale of $t_{\text{eff}} \propto t^2/|E - U|$. Since the magnitude of t_{eff} can be controlled by changing the tilting strength E, it is likely that the temperature of the order of t_{eff} is achievable in experiments. Moreover, recent experiments by Bakr *et. al.* [6] showed that the Mott phase contains particularly low entropy compared to the surrounding superfluid, and fits with theoretical curve suggest that the Mott phase is as low temperature as a few nK. Therefore, together with the demonstration of lattice tilting [2, 3] and possibility to create various lattice structures through a holographic mask technique [5], realization of this quantum liquid state should be possible with current technology.

2.4.2 Doubly-decorated square lattice

Although the quantum liquid state found in Section 2.4.1 has non-trivial entanglement, it does not have topological order. Here we show that by decorating the square lattice further, it is possible to obtain a model whose resonant subspace is labeled by the set of dimer packings of the undecorated square lattice. The dipole hopping terms appear in the perturbation theory of $1/\lambda$, and the effective Hamiltonian in this resonant subspace is expected to take a version of the quantum dimer model [26].

In this model, we consider a square lattice decorated by *two* sites at each link between lattice sites, as shown in Fig. 2.10a. Quantum spin models on a similar decorated square lattice were considered in Ref. [28]. In the limit $\lambda \rightarrow -\infty$, the ground states in the resonant subspace are those with maximum number of dipoles. As before, there are a large number of such states and they are all degenerate in this limit. The dipoles now come in two flavors: those which have one end on a central site of the square lattice, and those which reside exclusively on a link between central sites. Along a link between two central sites, the first kind of dipoles always come in pairs. We associate this pair with a "dimer" which connects two neighboring central sites (see Fig. 2.10b). Because there can be only one dimer on each site for $\lambda \rightarrow -\infty$, the dimers are close-packed, and there is a one-
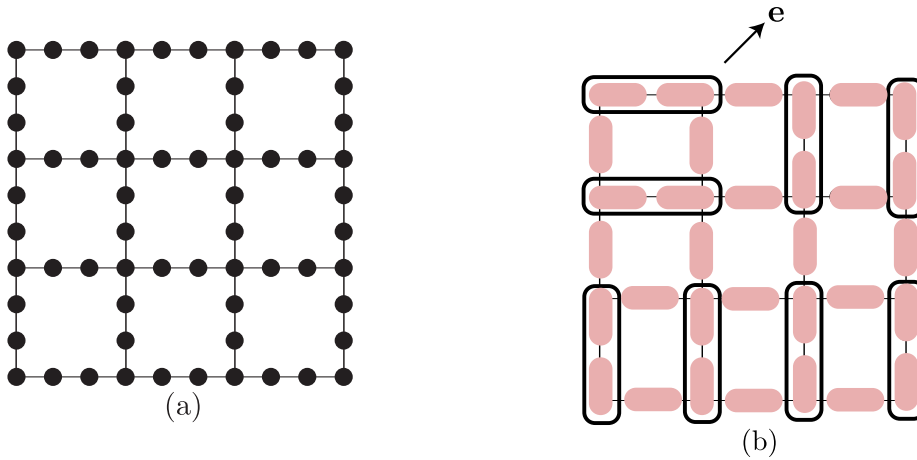
Figure 2.10: (a) The doubly-decorated square lattice. (b) Dense dipole configuration obtain in the limit $\lambda \to -\infty$. Each dipole is represented by the thick line, and consists of a particle-hole pair. Links with two dipoles are identified as having a "dimer", and these are indicated by the ovals. These dimers are described by an effective quantum dimer model.

to-one correspondence between the degenerate ground state manifold and the set of dimer packings of the square lattice. Including corrections in powers of $1/|\lambda|$ we expect an effective Hamiltonian which acts on a Hilbert space of states labeled by the dimer coverings: this must have the form of the quantum dimer model [26]. In particular, a plaquette-flip term appears at order $1/|\lambda|^{12}$; up to this order, all diagonal terms in the basis of dipole coverings are equal and independent of the configurations. We leave the details of the calculations as well as possible extensions to a future work, and give a general discussion below.

On the square lattice, quantum dimer models are generically expected to have ground states with valence bond solid orders [29]. At critical points between different solid orders, topologically ordered spin-liquids can be obtained [30, 31]. The quantum dimer model realized in this system consists of only a kinetic term, and no energy cost or gain for parallel dimers,

$$H_{\text{dimer}} = -t_{\text{dimer}} \sum_{\text{plaquettes}} \left(|{\parallel}\rangle \langle {=}| + |{=}\rangle \langle {\parallel}| \right). \tag{2.33}$$

This model is not critical, and so valence bond order is expected, but the precise nature of the square lattice symmetry breaking remains under study. An early exact diagonalization study [32] suggested a plaquette phase, more recent quantum Monte Carlo calculations [33] predicted a columnar phase, and recently a mixed columnar-plaquette phase has been proposed [34]. As λ increases away from $\lambda = -\infty$, configurations with less number of dipoles
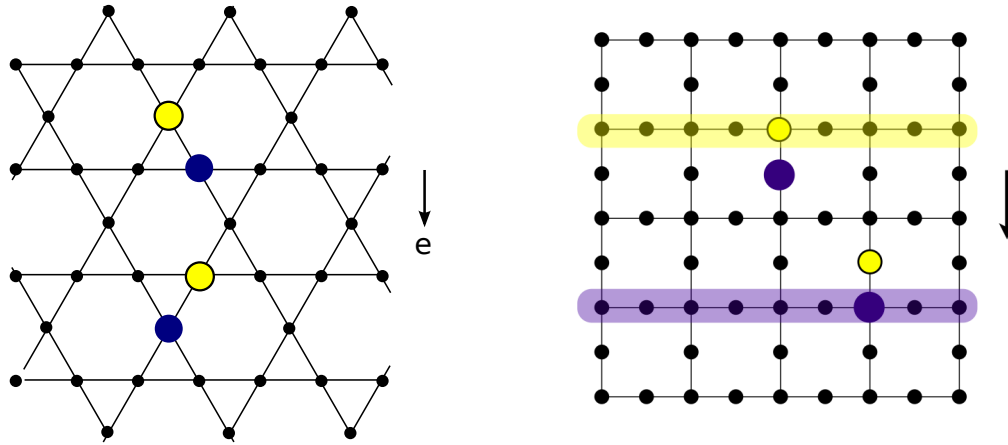
Figure 2.11: a) Kagome lattice tilted perpendicular to a principal lattice axis: resonant particle-hole excitations are illustrated. After a particle-hole pair is created, either the particle or the hole can hop along the direction transverse to the tilt. b) Decorated square lattice tilted along a principal lattice axis.

become energetically favorable. These states are analogous to those in the doped quantum dimer model [26, 35], where other novel phases are possible [36]. As the parent Mott insulator at $\lambda = \infty$ is non-degenerate, it cannot be connected adiabatically to all the possible $\lambda \to -\infty$ states with topological order or broken symmetry: there must be at least one intervening quantum phase transition.

2.4.3 Kagome lattice tilted perpendicular to a principal lattice axis

At last, we study the kagome lattice tilted perpendicular to a principle axis, as illustrated in Fig. 2.11. Similar conclusions hold for a decorated square lattice tilted along a principal lattice direction. Because of the low connectivity in the lattice structure, dipole creations are frustrated in the limit $\lambda \to -\infty$ and even in this limit, some sites cannot not participate in the creation of dipoles. As a result, there is no Ising ordering and the transverse superfluidity persists in the limit $\lambda \to -\infty$, as we describe below.

Limit $\lambda \to \infty$

The ground state is again the Mott insulator, and the excitations are particles and holes. For every particle-hole pair, either the particle or the hole is located on a transverse layer where it can hop, while the other is fixed and cannot move, see Fig. 2.11. The
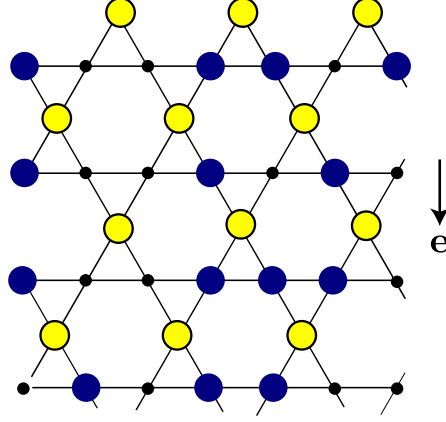
Figure 2.12: $\lambda \to -\infty$. Single non-degenerate ground state with half-filled Tonks gases along horizontal lines for $\lambda = -\infty$.

dispersion of the hopping quasiholes is

$$\epsilon_h(k) = \Delta - 2n_0 t \cos(ka),$$

while for hopping quasiparticles it is

$$\epsilon_p(k) = \Delta - 2(n_0 + 1)t \cos(ka).$$

Therefore, the hopping quasiparticles have lower energy than the hopping quasiholes. The excitations are gapped for $\lambda \to \infty$, but excitations become gapless for some critical value λ_c.

Limit $\lambda \to -\infty$

The ground state in the resonant subspace has the maximum number of dipoles. Due to the geometry of the kagome lattice, some sites are frustrated in the sense that they cannot participate in the creations of dipoles. These sites allow the particles and holes to move along the horizontal direction perpendicular to the tilt, forming Luttinger liquids. As the kinetic energy of quasiparticles is lower than that of the quasiholes, the ground state maximizes the number of moving quasiparticles in a transverse layer and localizes all the quasiholes, as shown in Fig. 2.12. Each transverse layer thus realizes a "Tonks-Girardeau gas" of bosons at half-filling [37], and the ground state realizes a collection of uncoupled gapless Luttinger liquids. These are gapless only in the limit $\lambda = -\infty$. Perturbation theory to second order in $1/\lambda$ generates a dimerized hopping term, *i.e.* the effective hopping

between two sites in a one-dimensional chain which share a neighbor above them becomes different from the hopping between sites which share a neighbor below. This breaks the translation symmetry along the one-dimensional layers explicitly, doubles the unit cell, and opens a gap, as the Tonks gases are exactly at half filling. Therefore, to order $1/\lambda^2$ the one-dimensional systems remain decoupled, but they are no longer gapless.

2.5   Modifications for $|U_3| \ll t$

In this section we briefly discuss how the physics of tilted lattices is modified if the U_3 term in Eq. (2.3) vanishes. In this case all processes $(n, n) \rightarrow (n - 1, n + 1)$ for general n are resonant at the same tilt magnitude. This greatly increases the size of space of states resonantly connected to the parent Mott insulator. As we will show in some cases the energy of this enlarged space is not bounded from below, and we then cannot use equilibrium methods to describe the physics. In other cases the resonant subspace remains bounded from below, but the phases differ from the ones found for $|U_3| \gg t$. We will illustrate this by two examples: square lattice tilted along a principle lattice direction, and diagonally tilted decorated square. We leave a more complete discussion for future study.

2.5.1   Square lattice tilted along a principal lattice direction

This case was considered in Ref. [7]. However, the results there apply only if the resonant subspace is limited by a large $|U_3|$. For small $|U_3|$ the physics is quite different, as we now describe.

In particular, we can no longer use equilibrium methods, as the energy of the subspace resonantly connected to the parent Mott insulator is not bounded from below, when $\lambda \rightarrow -\infty$. Once a particle-hole pair is created, the particle and hole are each free to move in the direction transverse to the tilt. It is then possible that two quasiparticles are adjacent to each other, in such a way that they can undergo a resonant transition. The system can resonantly reach states with an arbitrarily large number of bosons on a lattice site, as illustrated in Fig. 2.13, leading to an arbitrarily large negative energy.
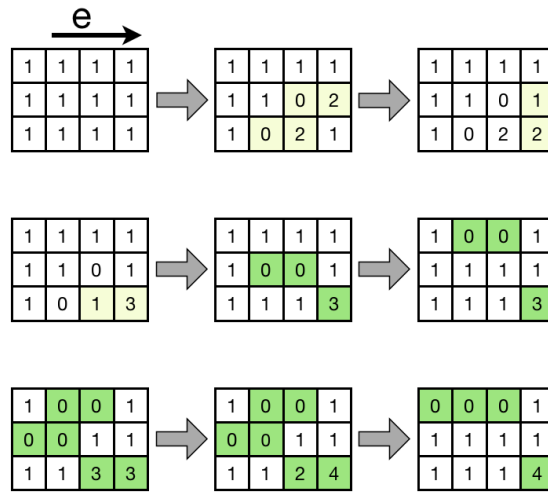
Figure 2.13: Square lattice tilted along a lattice direction for $U_3 = 0$. The number in each square represents the number of bosons at that site. Here the occupancy of the parent Mott insulator is $n_0 = 1$. We illustrate resonant processes which eventually lead to the creation of lattice sites occupied by 4 bosons. It is possible to continue this pattern, thus we obtain any arbitrarily large number n_B of bosons on a single site, through resonant processes. In the end, only a total number of n_B lattice sites remain changed (shown in green). Having n_B bosons on a site reduces potential energy $n_B(n_B - 1)\Delta/2$. One could fill the lattice with such patterns. Thus the energy of states resonantly connected to the parent Mott insulator is not bounded from below.
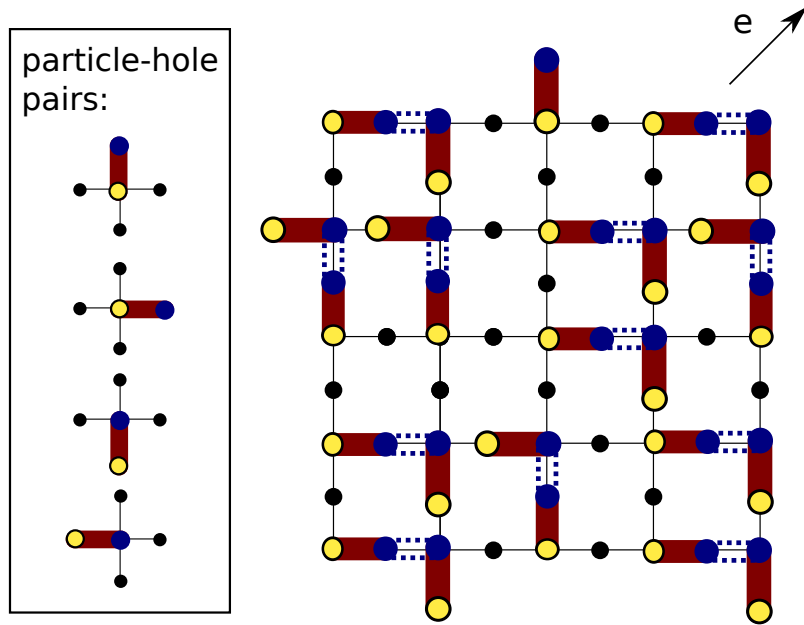
Figure 2.14: Decorated square lattice in diagonal tilt, filling factor $n_0 = 1$, $U_3 = 0$. Quasi-particles are shown as dark blue circles, quasiholes as circles with yellow filling. Two neighboring quasiparticles can form another dipole bond $(2, 2) \rightarrow (1, 3)$ which reduces the energy by Δ. This is indicated in the figure by dotted blue lines. Quasiholes contain no bosons, and they cannot form another dipole bond. To minimize its energy, the system not only maximizes the number of dipoles on the lattice, but also maximize the number of neighboring quasiparticles. The set of states fulfilling these requirements maps to the dimer coverings of a square lattice, and one such dimer covering is shown above.

2.5.2 Diagonally tilted decorated square lattice

This lattice remains stable: the energy of the enlarged resonant subspace is bounded from below. This stability is related to the lower connectivity of the lattice structure, and the suppression of transverse superfluidity in Section 2.4.1. Let us consider the phases in the limit $\lambda \rightarrow -\infty$. We distinguish two cases: filling factor $n_0 = 1$, and filling factor $n_0 > 1$.

Filling of parent Mott insulator: $n_0 = 1$

Particle-hole pairs each reduce potential energy by Δ, and they may be arranged in such a way that each quasiparticle is adjacent to another quasiparticle. This allows for a third resonant transition, $(2, 2) \rightarrow (1, 3)$, which again reduces potential energy by Δ. As illustrated in Fig. 2.14, this always leads to a central site being occupied by three bosons.

Two such sites are never adjacent to each other, so that an occupation number of four or more bosons on any site cannot be reached resonantly. The energy remains bounded from below. In the limit $\lambda \to -\infty$ the resonantly connected subspace has a large number of ground states, and there is a one-to-one correspondence between this degenerate ground state manifold and the set of dimer packings on the square lattice. A plaquette-flip term of the dimers appears in order $1/\lambda^{12}$. Thus we obtain a remarkable mapping of the effective Hamiltonian to the quantum dimer model. Unlike the large U_3 case in Section 2.4, here the dimer model appears already for the singly-decorated square lattice, and so should be easier to realize experimentally.

Filling of parent Mott insulator: $n_0 > 1$

If the filling factor is two or larger, then two adjacent 'quasiholes' can undergo a resonant transition $(n_0 - 1, n_0 - 1) \to (n_0 - 2, n_0)$, reducing the potential energy by Δ. Potential energy is minimized if each 'quasihole' and each 'quasiparticle' can undergo such a transition, as illustrated in Fig. 2.15. This leads to a two fold degenerate ground state with density-wave order: all central sites are occupied by either $(n_0 + 2)$ or $(n_0 - 2)$ bosons, while all other sites contain n_0 bosons.

2.6   Conclusions

This Chapter has shown that there are rich possibilities for generating non-trivial quantum states upon tilting a Mott insulator of bosons. Our classical intuition tells us that applying a strong tilt to a Mott insulator should lead to a runaway instability of particles flowing downhill. However, quantum mechanically, for a single band model in the absence of external dissipation, and with a significant three-body interaction U_3, this does not happen. Instead particle motion is localized in the direction of the tilt, and free motion is only possible in orthogonal directions. It is useful to introduce the idea of a resonant subspace of states which are strongly coupled to the parent Mott insulator when the tilt approaches its critical value. Within this resonant subspace, we can define an effective Hamiltonian whose energy is bounded from below, and which has well defined equilibrium quantum phases and phase transitions. We presented a variety of such effective models here, and described general aspects of their phase diagrams. As in the previous work [7], we found phases with Ising density wave order along the tilt direction, and superfluid/Luttinger
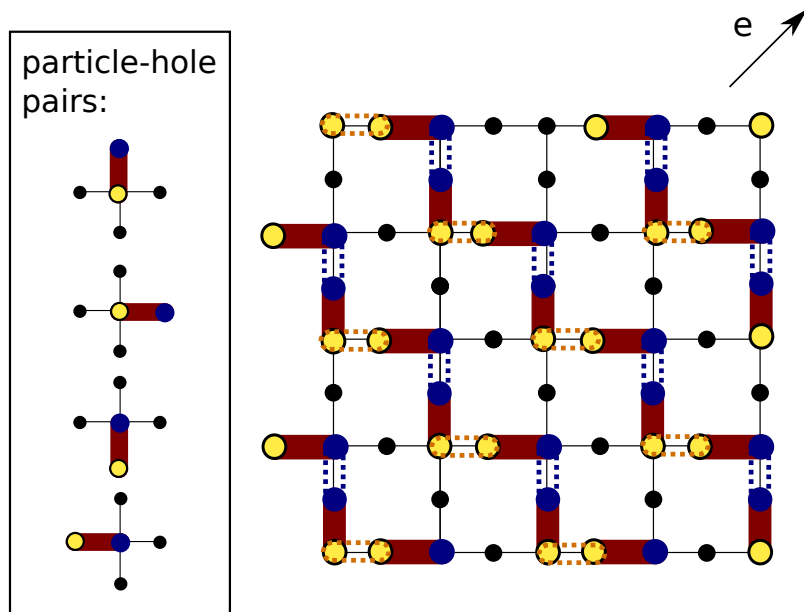
Figure 2.15: Decorated square lattice in diagonal tilt, filling factor $n_0 > 1$, $U_3 = 0$. In this case 'quasiholes' can also undergo a resonant transition, which is shown as orange dotted lines. There are two degenerate ground states with density-wave order: the one shown in the figure, and its symmetry related partner.

liquid behavior in the direction transverse to the tilt. More interestingly, we showed that on a variety of frustrated or decorated lattices, particle motion can be suppressed also in directions transverse to the tilt. Then, the tilted lattices map onto quantum clock or dimer models, with novel quantum liquid and solid phases.

We also briefly noted, in Section 2.5, the situation when $|U_3|$ was small. In some cases, the energy of the resonant subspace is unbounded from below, and so non-equilibrium methods will be necessary to understand the physics. However, for the simple case of the decorated square lattice, we found a mapping of the effective Hamiltonian to that of the quantum dimer model in a limiting case, as illustrated in Fig. 2.14.

It is clear that the models studied here have extensions to numerous other lattices and decorations, and that there are many promising avenues for obtaining exotic phases. It would also be interesting to study the analogous models of fermions, which could display metallic states associated with motion in the transverse directions. In principle, all these models should be readily accessible in experiments on trapped ultracold atoms.

2.7 Appendix: Decorated square lattice in the $\lambda \to -\infty$ limit

2.7.1 Ground state correlation functions

To calculate correlation functions in the exact ground state of the effective clock model, Eq. (2.32), we make use of the following "transfer matrix" method. For an equal-amplitude ground state, correlations of operators, $\hat{O}$, which are diagonal in the basis of dipole coverings, can be related to a corresponding classical problem

$$\langle \hat{O} \rangle = \frac{\langle \psi_c | \hat{O} | \psi_c \rangle}{\langle \psi_c | \psi_c \rangle} = \frac{\sum_M \langle M | \hat{O} | M \rangle}{D_c}. \tag{2.34}$$

Here, the sum over M runs over all states that maximize the number of dipoles and respect constraints Eq. (2.19) and (2.20). We assume that all the states $|M\rangle$ are properly normalized, $\langle M | M \rangle = 1$, and define $D_c = \sum_M \langle M | M \rangle = \dim(H_c)$ as the dimension of the Hilbert space with constraint. The density operator $\hat{n}_{l,m}$ measuring the relative density at central site (l, m) is diagonal in the basis of dipole coverings; it has eigenvalues ± 1. Therefore, $\langle \hat{n}_{(0,0)} \hat{n}_{(l,m)} \rangle$ can be written as

$$\langle \hat{n}_{(0,0)} \hat{n}_{(l,m)} \rangle = \frac{N_+ - N_-}{D_c}, \tag{2.35}$$

where $N_{\pm}$ is the number of configurations which have $\langle M| \, \hat{n}_{(0,0)} \hat{n}_{(l,m)} \, |M\rangle = \pm 1$. The problem of calculating correlation functions of the ground state reduces to counting the number of classically allowed dipole coverings. This counting can be done using row-to-row transfer matrices.

Let T be the transfer matrix for a row of length N_x unit cells. T is a $4^{N_x} \times 4^{N_x}$ matrix and acts on the space of dipole configurations within that row. Note that this Hilbert space includes configurations which are not allowed by the constraint. Such configurations are excluded by setting the corresponding matrix elements of T to zero. The matrix elements of T are either 1 or 0, so that $T_{c',c} = 1$ if the sequence of two row configurations c, c' contains no violations of the constraint, and $T_{c',c} = 0$ otherwise. The dimension of the Hilbert space for a $N_x \times N_y$ lattice with periodic boundary conditions is then given by the trace of powers of the transfer matrix,

$$D_c = \mathrm{Tr}(\mathrm{T}^{\mathrm{N_y}}). \tag{2.36}$$

A naive numerical implementation of Eq. (2.36) (without using the sparseness of T) gives a complexity of $O(N_y 4^{3N_x})$, compared to going over all the states in the Hilbert space with complexity $O(4^{N_x N_y})$. The values for $N_{\pm}$ can be similarly found by including projection matrices in the trace, for example

$$N_+ = \mathrm{Tr}\left(T^{N_y - m} P_{p;l} T^m P_{p;0}\right) + \mathrm{Tr}\left(T^{N_y - m} P_{h;l} T^m P_{h;0}\right). \tag{2.37}$$

Here $P_{p;l}$ ($P_{h;l}$) is a projection matrix that projects onto configurations which have a particle (a hole) at site $l = 0, 1, \ldots, N_x - 1$ of a given row, respectively. Using this method different correlations for the dipole-directions can also be calculated.

2.7.2 Connecting the ground state to a site-factorizable state

In this appendix, we provide evidence that the ground state of H^c_{clock}, Eq. (2.32), is not topologically ordered. To show this, we demonstrate that the ground state of H^c_{clock} can be smoothly connected to the ground state of H_{clock} (without the "hard core" constraint of the dipole-clocks). The ground state of H_{clock} is a site factorizable state, and therefore it is topologically trivial. The fact that $|\psi_c\rangle$ can be connected to it, while keeping the correlation length finite, is a strong indication that $|\psi_c\rangle$ does not have topological order either. To connect the ground state of H^c_{clock} to the ground state of H_{clock}, Eq. (2.29), we

define the wave function

$$|\psi(\epsilon)\rangle = \sum_C \epsilon^{n(C)/2} |C\rangle . \tag{2.38}$$

Here the sum over C runs over all 4^N dipole coverings with one dipole per unit cell, including those which do not respect the constraint. The function $n(\epsilon)$ is an integer counting the number of colliding arrows in configuration C. All allowed configurations M have $n(M) = 0$. Thus changing the value of ϵ interpolates between the ground state of H_{clock}^c, $|\psi_c\rangle$, and the ground state of H_{clock}, $|\psi_0\rangle$,

$$|\psi(\epsilon = 0)\rangle = |\psi_c\rangle , \tag{2.39}$$

$$|\psi(\epsilon = 1)\rangle = |\psi_0\rangle . \tag{2.40}$$

As the density operator $\hat{n}_{(l,m)}$ is still diagonal in the basis of C, we can again use (generalized) transfer matrices to compute density-density correlation functions for any value of ϵ. The result is shown in Fig. 2.16, and we find no divergence in the correlation length. This supports our conjecture that the ground state $|\psi_c\rangle$ is topologically trivial. Of course, we have not calculated *all* possible correlation functions, so this is an evidence, but not a proof.

To calculate the correlation functions, we make use of equations (2.35), (2.36), and (2.37), with one modification: the transfer matrix $T(\epsilon)$ now depends on the parameter ϵ in the following way

$$(T(\epsilon))_{c',c} = \epsilon^{n(c',c)}, \tag{2.41}$$

where $n(c', c)$ is the number of collisions in row-configuration c', plus the number of collisions *between* rows c and c'. The number of collisions in the other row, c, does not come in here, to avoid double counting.
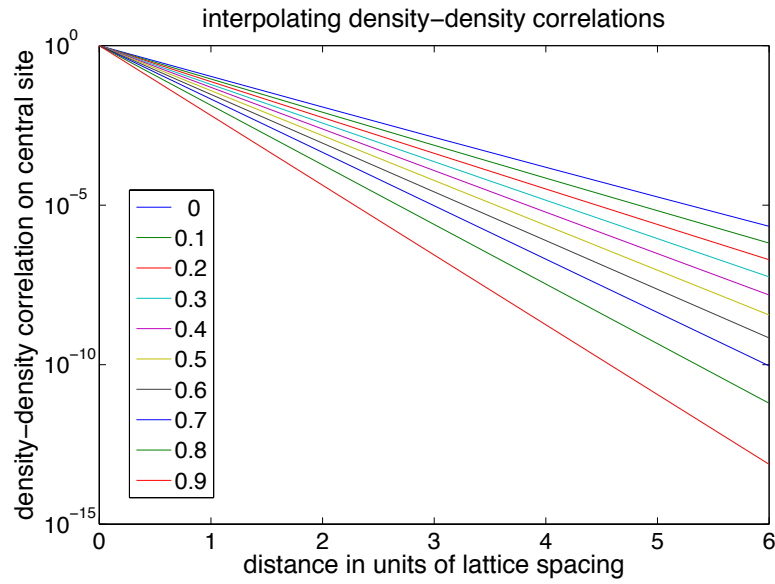
Figure 2.16: Density-density correlations of a wavefunction which interpolates between the ground states of H_{clock}^c and H_{clock}, see text. Different colors stand for different values of the parameter ϵ. The correlation length does not diverge, it decreases as $\epsilon \to 0$. This provides evidence that the state $|\psi_c\rangle$ is topologically trivial.

Chapter 3

Phase Diagram of the Tilted Decorated Square Lattice

3.1 System and Model

In this chapter we study the phase diagram of the decorated square lattice in diagonal tilt, and in slightly off diagonal tilt. We have already described the phases of the diagonally tilted decorated square lattice in the previous chapter: in the weakly tilted limit the Mott insulator remains stable, while in the strongly tilted limit the ground state is a unique and gapped disordered dipole liquid state.

In diagonal tilt the Hamiltonian in the resonant subspace is given by Eq. (2.18)

$$H = \Delta \sum_a \hat{d}_a^\dagger \hat{d}_a - t\sqrt{n_0(n_0 + 1)} \sum_a \left(\hat{d}_a + \hat{d}_a^\dagger \right),$$

where a labels the lattice links, and $\hat{d}_a^\dagger$ creates a dipole on this link. The resonant subspace has the constraints $\hat{d}_a^\dagger \hat{d}_a \leq 1$, and $\hat{d}_a^\dagger \hat{d}_a \hat{d}_{a'}^\dagger \hat{d}_{a'} = 0$, if a and a' share a lattice site, see Fig. 3.2. As in the previous chapter we have defined $\Delta = U - E$ and we work in the limit $|\Delta|, t \ll |U|, |E|, |U_3|,$. For most of the following discussion we will use units in which

$$t\sqrt{n_0(n_0 + 1)} = 1 \tag{3.1}$$

Note that using these units, the one dimensional chain has its Ising transition at $\Delta = -1.31$ for $n_0 = 1$ [7]. If the tilt is not exactly diagonal, $\vec{E} = (E_x, E_y)$, then we have two tuning parameters

- $\Delta_x = U - E_x =$ energy cost for dipoles in x direction (left-right); we define

$$\lambda_x = \frac{\Delta_x}{t\sqrt{n_0(n_0 + 1)}},$$

- $\Delta_y = U - E_y =$ energy cost for dipoles in y direction (up-down); we define

$$\lambda_y = \frac{\Delta_y}{t\sqrt{n_0(n_0 + 1)}},$$

and we tune Δ_x and Δ_y separately. We are still in the regime

$$|\Delta_x|, |\Delta_y|, t \ll |U|, |E|, |U_3|,$$

which gives us two independent tuning parameters which can take all real values: λ_x and λ_y. The Hamiltonian in the effective resonant subspace becomes

$$\hat{H} = \Delta_x \sum_{i \in \text{x-links}} \hat{d}_i^\dagger \hat{d}_i + \Delta_y \sum_{j \in \text{y-links}} \hat{d}_j^\dagger \hat{d}_j - t\sqrt{n_0(n_0 + 1)} \sum_a \left(\hat{d}_a + \hat{d}_a^\dagger \right), \qquad (3.2)$$

where the first sum runs only over links aligned in x direction, second sum only over links aligned in y direction, last sum over all links. The constraints Eq. (2.19) and Eq. (2.20) hold. Note that a non-diagonal tilt reduces the rotation symmetry of the effective resonant subspace: it is no longer invariant under rotation by 90 degrees, we illustrate this by drawing a decorated rectangular lattice, see Fig. 3.1b.

3.1.1 Description by a constrained five-state model

We can describe the resonantly connected subspace for all values of our tuning parameters λ_x and λ_y by a constrained five-state model on a simple square lattice. We again let our unit cell be centered about the sites with four neighbors, see Fig. 2.7. Each of the unit cells may be in one out of five states, see Fig. 3.1: It may contain no dipole (state $|0\rangle$), or it may contain one dipole, and there are four links to choose from (states $|1\rangle, |2\rangle, |3\rangle, |4\rangle$). The Hamiltonian of a single site[1] is then given by (using units in which

---

[1] For $\Delta_x = \Delta_y$ this Hamiltonian has three degenerate dark states at energy Δ and two other eigenvalues at $\epsilon_{\text{gs/es}} = \frac{\Delta}{2} \pm \frac{1}{2}\sqrt{\Delta^2 + 16}$ which correspond to the eigenstates $|\phi_{\text{gs}}\rangle = \sin\theta |0\rangle + \frac{1}{2}\cos\theta (|1\rangle + |2\rangle + |3\rangle + |4\rangle)$, $|\phi_{\text{es}}\rangle = \cos\theta |0\rangle + \frac{1}{2}\sin\theta (|1\rangle + |2\rangle + |3\rangle + |4\rangle)$, where $\tan\theta = \frac{4}{-\Delta + \sqrt{\Delta^2 + 16}}$. For $\Delta_x = \Delta_y$ there are only two dark states.
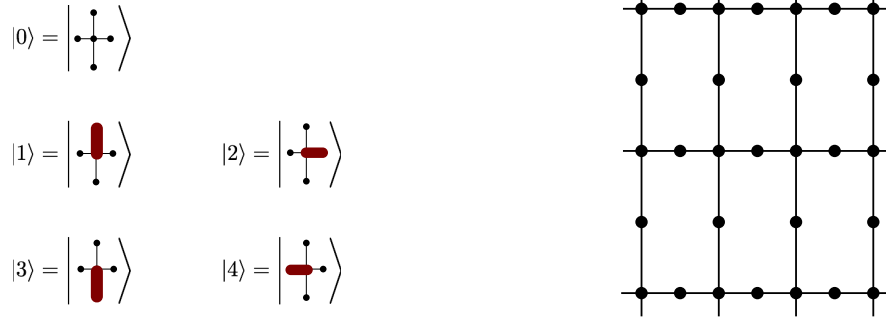
Figure 3.1: a) Notation of the constrained five-state model. b) If $\Delta_x \neq \Delta_y$ then horizontal dipoles have a different energy cost than vertical ones. We illustrate this by a decorated rectangular lattice. The effective resonant subspace has all the symmetries of this lattice.

$t\sqrt{n_0(n_0 + 1)} = 1)$

$$
\begin{aligned}
H_{\text{site}} &= H_{\text{pot}} + H_{\text{kin}} \\
H_{\text{pot}} &= \Delta_x \left(|2\rangle \langle 2| + |4\rangle \langle 4| \right) + \Delta_y \left(|1\rangle \langle 1| + |3\rangle \langle 3| \right) \\
H_{\text{kin}} &= -|0\rangle \left(\langle 1| + \langle 2| + \langle 3| + \langle 4| \right) + \text{h.c.}.
\end{aligned}
\tag{3.3}
$$

Summing over all sites we obtain the free Hamiltonian of the five state system

$$
H_{\text{free}} = \sum_{x,y=1}^{L_x, L_y} H_{\text{site}}(x, y).
$$

Additionally there is a constraint that the dipoles may not overlap: two neighboring unit cells may not point toward each other. We take this into account by projecting out all the states which would create such a collision

$$
H^c = P_c H_{\text{free}} P_c
$$

where P_c is a projection operator which projects out all the states that are forbidden by the constraint.

3.1.2   Mapping to a frustrated Ising spin model

In [3] and [7] the physics of a tilted one dimensional Mott Insulator was described by an antiferromagnetic Ising spin chain in a transverse and longitudinal field. In the same spirit, we map the diagonally tilted decorated square lattice to an antiferromagnetic spin model, also in longitudinal and transverse field, on a *frustrated* lattice. Note that the spin
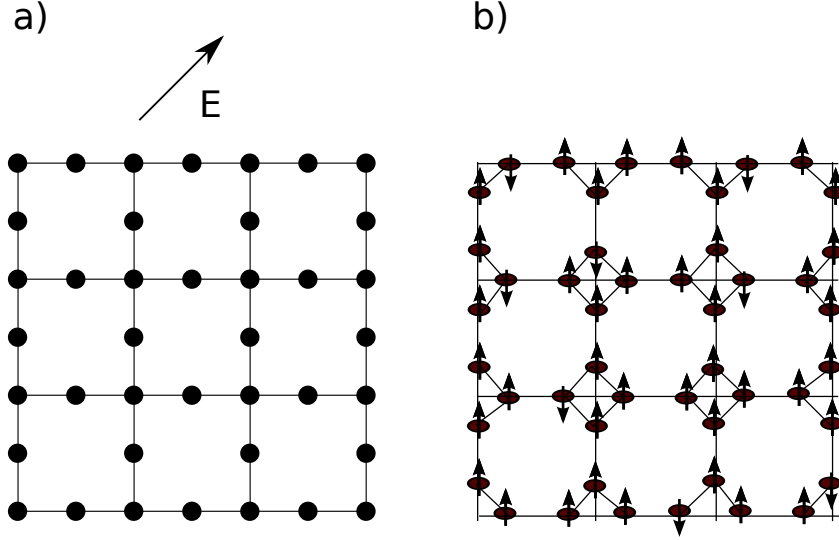
Figure 3.2: a) decorated square lattice: this is the lattice for the bosons. The spins reside on the links, which form the lattice b). The effective resonant subspace of the boson model maps to an antiferromagnet on this lattice, in a strong longitudinal and in a transverse magnetic field. If the tilt is not exactly diagonal, then spins on horizontal lines experience a different longitudinal field than spins on vertical lines. The spin lattice is not bipartite, and so the antiferromagnet is frustrated.

degrees of freedom reside on the links of the decorated square lattice, so that the lattice of the spin model is an 'octagon-square-cross' lattice as depicted in Fig. 3.2. This lattice has four sites per unit cell, and each spin has $z_{\mathrm{coord}} = 4$ neighbors. As the lattice is not bipartite, an antiferromagnetic spin model on this lattice is frustrated, and two-dimensional Ising density wave order is not possible. The Hamiltonian of the resonant subspace can be described by the following spin model

$$H = J \left(\sum_{\langle i,j \rangle} S_z^i S_z^j - h_z^{\mathrm{LR}} \sum_{i \in \mathrm{LR}} S_z^i - h_z^{\mathrm{UD}} \sum_{i \in \mathrm{UD}} S_z^i - h_x \sum_i S_x^i \right) \tag{3.4a}$$

$$h_z^{\mathrm{LR}} = \left(2 - \frac{\Delta_x}{J} \right), \qquad h_z^{\mathrm{UD}} = \left(2 - \frac{\Delta_y}{J} \right) \tag{3.4b}$$

$$h_x = \frac{2t}{J} \sqrt{n_0(n_0 + 1)} \tag{3.4c}$$

where $\vec{S} = \frac{1}{2}\vec{\sigma}$. The second sum ($i \in \mathrm{LR}$) is over all spins which reside on lines in horisontal direction, see Fig. 3.2, and the third sum ($i \in \mathrm{UD}$) is over spins that reside on vertical lines. While the first three terms all commute with each other, the last term does not. It

is this transverse field which makes this a quantum problem. The strong antiferromagnetic interaction and the strong longitudinal field are introduced to realize the constraint: having two neighboring spin down costs an energy of order J. The mapping becomes exact in the limit $J \to \infty$. As in one dimension, this is of course not a mapping of the full bosonic model to a spin model, but of the resonantly connected subspace.

We will phrase most of the following discussion in the language of the constrained five-state model, keeping in mind that the results can directly be applied to the frustrated Ising spin model.

3.1.3   Limiting cases

We understand the system in the following limiting cases

1. $\Delta_x, \Delta_y \to \infty$, $\Delta_x/\Delta_y = 1$: This is the parent Mott insulator state, the dipole vacuum. Dipole creation costs an infinite amount of energy, and so no dipoles are created.

2. $\Delta_x, \Delta_y \to -\infty$, $\Delta_x/\Delta_y = 1$: This is the quantum liquid state described in Section 2.4. The number of dipoles is maximized, and the ground state is an equal amplitude superposition of all dipole product states that fulfill the constraint. As we have shown in the previous chapter, this is a disordered state; the ground state is unique and gapped.

3. $\Delta_y \to +\infty$; $\Delta_x/\Delta_y \to 0$: along this line vertical dipole states on links aligned in y direction can never be occupied, as they cost an infinite amount of energy, while horizontal dipoles along links in x direction are accessible. In this limit it is clear that the system decouples into a collection of horizontal one dimensional chains. These chains are effectively one dimensional, they undergo a phase transition in the Ising universality class[2] at a critical value of $\Delta_y = -1.31$ (which is the same as in the one dimensional case).

We expect the one dimensional order within each chain to persist when Δ_y takes on finite values. Neighboring chains may then interact via dipole states aligned in y direction, which might lead to a coupling between these chains, and thus to two-dimensional order.

The dipole liquid state in the limit of strong diagonal tilt and the Mott insulator in the

---

[2]The symmetry which is broken in the ordered phase is a reflection symmetry. The lattice does not have this translation symmetry unless Δ_x strictly ∞.

limit of weak tilt have the same symmetries: no broken symmetries. In the following we will show that the quantum liquid phase is continuously connected to the parent Mott insulator without an intervening quantum phase transition.

3.1.4 Order parameters

In the following we will use Quantum Monte Carlo (QMC) simulations to study the phase diagram for all values of the tuning parameters λ_x and λ_y. We expect one dimensional order to persist in some region of the phase diagram, and so we introduce order parameters which probe for 1D Ising order, as well as order parameters which probe for two-dimensional order.

Before introducing our order parameters, we begin by reviewing the order parameter of the one dimensional system in [7, 3]: a staggered magnetization which breaks lattice symmetries (translation, inversion, and reflection symmetry). In the language of the spin mapping in Section 3.1.2, and Ref. [3] it is given by

$$M = \frac{1}{L}\sum_l (-1)^l \sigma_l^z.$$

In our case in the limit $\Delta_y = \infty$, $\Delta_x/\Delta_y = 0$ each unit cell of the decorated square lattice has only three states available, and we can directly translate this staggered magnetization to our notation. Each chain aligned along the x direction and at position y then has its own, independent order parameter

$$M_{\mathrm{LR}}(y) = \frac{1}{L_x}\sum_x (\hat{p}_\to - \hat{p}_\leftarrow)_{x,y} = \frac{1}{L_x}\sum_x m_{\mathrm{LR}}(x,y), \qquad (3.5)$$

where $\hat{p}_d$ is a projection operator that projects onto the dipole state d. The (staggered) magnetization of each unit cell has been defined for dipoles along left-right direciton only as

$$m_{\mathrm{LR}}(x,y) = \hat{p}_\leftarrow - \hat{p}_\to$$

When $\Delta_y \neq \infty$, then each unit cell has two additional states available[3]. We can still use the above definition, and add another component to the order parameter,

$$m_{\mathrm{UD}}(x,y) = \hat{p}_\downarrow - \hat{p}_\uparrow$$

---

[3]This breaks the translation symmetry of the one dimensional chain explicitly: There is no translation relating the state $|\to\rangle$ to the state $|\leftarrow\rangle$, under which the order parameter would change sign. There is, however, an inversion symmetry and a reflection symmetry left, which can be spontaneously broken by an ordered state.

the magnetization for dipoles aligned in y direction. We combine the two to a vector,

$$\vec{m}(x,y) = \begin{pmatrix} m_{\mathrm{LR}}(x,y) \\ m_{\mathrm{UD}}(x,y) \end{pmatrix}$$

we will refer to this as the "magnetization" of a unit cell of our system. $\vec{m}(x,y)$ transforms as a vector and is odd under inversion (and rotation about 180 degrees),

$$(x,y) \to (-x,-y) \quad : \qquad \vec{m} \to -\vec{m}$$

$$(x,y) \to (-x,y) \quad : \qquad \begin{pmatrix} m_{\mathrm{LR}} \\ m_{\mathrm{UD}} \end{pmatrix} \to \begin{pmatrix} -m_{\mathrm{LR}} \\ m_{\mathrm{UD}} \end{pmatrix}$$

$$(x,y) \to (x,-y) \quad : \qquad \begin{pmatrix} m_{\mathrm{LR}} \\ m_{\mathrm{UD}} \end{pmatrix} \to \begin{pmatrix} m_{\mathrm{LR}} \\ -m_{\mathrm{UD}} \end{pmatrix}$$

To probe for two-dimensional order in the system, we define the total magnetization

$$\vec{M} = \frac{1}{L_x L_y} \sum_{x,y} \vec{m}(x,y). \tag{3.6}$$

and measure

$$\langle \vec{M}^2 \rangle = \frac{1}{L_x^2} \frac{1}{L_y^2} \sum_{x,x',y,y'} \left(\langle m_{\mathrm{LR}}(x,y) m_{\mathrm{LR}}(x',y') \rangle + \langle m_{\mathrm{UD}}(x,y) m_{\mathrm{UD}}(x',y') \rangle \right).$$

If the chains are aligned ferromagnetically, then this order parameer is non-zero. To probe for antiferromagnetically aligned chains we define a total staggered magnetization

$$\vec{M}_{\mathrm{stagg,x}} = \frac{1}{L_x L_y} \sum_{x,y} (-1)^x \vec{m}(x,y),$$

$$\vec{M}_{\mathrm{stagg,y}} = \frac{1}{L_x L_y} \sum_{x,y} (-1)^y \vec{m}(x,y).$$

For anisotropic tilt we expect the most important effect to be an order within each chain. These chains may or may not be coupled to form two-dimensional order. It is therefore usefull to define order parameters which probe for one dimensional order along x or y direction only. For this purpose we will use $M_{\mathrm{LR}}(y)$, Eq. 3.5, and average its absolute value over all chains,

$$\langle \langle M_{\mathrm{LR}}^2 \rangle \rangle = \frac{1}{L_y} \sum_y \langle M_{\mathrm{LR}}^2(y) \rangle = \frac{1}{L_x} \frac{1}{L_y^2} \sum_y \langle \left(\sum_x m_{\mathrm{LR}}(x,y) \right)^2 \rangle,$$

$$= \frac{1}{L_x} \frac{1}{L_y^2} \sum_{x,y,y'} \langle m_{\mathrm{LR}}(x,y) m_{\mathrm{LR}}(x,y') \rangle$$

and similarly for for chains aligned along y

$$\langle\langle M_{\text{UD}}^2 \rangle\rangle = \frac{1}{L_x^2} \frac{1}{L_y} \sum_{x,x'y} \langle m_{\text{UD}}(x,y) m_{\text{UD}}(x',y) \rangle.$$

3.2   Quantum Monte Carlo study of the problem

To find the phase diagram for all values of λ_x and λ_y we study the problem by Quantum Monte Carlo simulation.

3.2.1   Mapping to a three dimensional classical problem

Let us first map the single site Hamiltonian 3.3 to a one dimensional classical statistical mechanics problem. Next we will map the two-dimensional constrained five state problem to a three dimensional classical problem. The partition function of the single site quantum system at temperature T is given by

$$Z = \text{Tr}\left(e^{-\beta H_{\text{site}}}\right)$$

where $\beta = 1/T$ and we work in units where $\hbar = k_B = 1$. We can now rewrite this expression using $\beta = aM_\tau$, which then allows us to separate the non-commuting potential and kinetic energy term,

$$Z = \text{Tr}\left(\left(e^{-aH}\right)^{M_\tau}\right) = \text{Tr}\left(\left(e^{-aH_{\text{pot}}} e^{-aH_{\text{kin}}} + O\left(a^2\right)\right)^{M_\tau}\right),$$

this introduces the so called Trotter error [reference] of order a^2. To map to a classical system, we define the transfer matrices

$$T_1 = e^{-aH_{\text{pot}}} = \begin{pmatrix} 0 & 0 & 0 & 0 & 0 \\ 0 & e^{-a\Delta_x} & 0 & 0 & 0 \\ 0 & 0 & e^{-a\Delta_y} & 0 & 0 \\ 0 & 0 & 0 & e^{-a\Delta_x} & 0 \\ 0 & 0 & 0 & 0 & e^{-a\Delta_y} \end{pmatrix}$$

$$T_2 = e^{-aH_{\text{kin}}} = \begin{pmatrix} 1 & a & a & a & a \\ a & 1 & 0 & 0 & 0 \\ a & 0 & 1 & 0 & 0 \\ a & 0 & 0 & 1 & 0 \\ a & 0 & 0 & 0 & 1 \end{pmatrix}$$

and rewrite

$$Z = \text{Tr}\left((T_1 T_2)^{M_\tau}\right) + O\left(a^2\right)$$

We can now map this quantum problem to a classical statistical mechanics problem with an additional dimension, the "imaginary time direction" in the following way. The off-diagonal matrix elements of the quantum Hamiltonian become a nearest neighbor energy cost for configurations along this new imaginary time direction. Let σ be one of the five states,

$$
\begin{aligned}
Z &= \sum_{\sigma=0}^{4} \langle\sigma|(T_1 T_2)^{M_\tau}|\sigma\rangle = \sum_{\sigma=0}^{4} \langle\sigma|\left(T_1 T_2 \sum_{\sigma'}|\sigma'\rangle\langle\sigma'|\right)^{M_\tau}|\sigma\rangle \\
&= \sum_{\{\sigma_\tau\}} \prod_{\tau=1}^{M_\tau} \langle\sigma_\tau|T_1 T_2|\sigma_{\tau+1}\rangle
\end{aligned}
$$

and this is how an additional dimension appears! We can make this mapping more explicit by interpreting the log of T_2 as a Hamiltonian acting between different time slices

$$\langle\sigma_\tau|T_2|\sigma_{\tau+1}\rangle = e^{-H_2^{\text{class}}(\sigma_\tau,\sigma_{\tau+1})}$$

with

$$
H_2^{\text{class}}(\sigma_\tau,\sigma_{\tau+1}) =
\begin{pmatrix}
0 & -\log(a) & -\log(a) & -\log(a) & -\log(a) \\
-\log(a) & 0 & \infty & \infty & \infty \\
-\log(a) & \infty & 0 & \infty & \infty \\
-\log(a) & \infty & \infty & 0 & \infty \\
-\log(a) & \infty & \infty & \infty & 0
\end{pmatrix}
$$

in imaginary time direction there is also a hard constraint: a dipole state cannot be neighbor to any different dipole state. This is not at all related to the constraint in real space. There is an energy cost for bonds between $|0\rangle$ and a dipole. The diagonal part of the classical Hamiltonian is the same as for the quantum Hamiltonian, and $H_{\text{class}} = H_1^{\text{class}} + H_2^{\text{class}}$. Finally, the partition function can be written as

$$Z = \sum_{\{\sigma_\tau\}} e^{-H_{\text{class}}(\{\sigma_\tau\})}$$

Here $\{\sigma_\tau\}$ means a particular configuration of all the different time slices, and $\sum_{\{\sigma_l\}}$ sums over all possible configuration of the M_τ time slices. It is also worth noting that we do not need the classical Hamiltonian for the QMC simulations: instead we work directly with the transfer matrices.

It is now straightforward to generalize this to the two-dimensional quantum problem. In fact, the only off-site terms are the ones coming from the hard constraint. This translates directly to the classical Hamiltonian:

$$Z = \text{Tr}\left(e^{-\beta P_c H_{\text{clock}} P_c}\right) = \text{Tr}\left(\left(e^{-a P_c H_{\text{kin}} P_c} e^{-a P_c H_{\text{pot}} P_c}\right)^{M_\tau}\right) = \sum_{\{\sigma_{x,y,\tau}\}} e^{-H_{\text{class}}(\{\sigma_{x,y,\tau}\})}$$

and the Hamiltonian H_{class} now has the additional hard core constraint in real space direction.

3.2.2 QMC updates

We simulate the corresponding classical statistical mechanics problem, and so we need a three dimensional lattice. Instead of summing over all possible configurations $\{\sigma_{x,y,\tau}\}$ – that would of course be impossible – we generate a sample of configurations which appear with the right probabilities, given by the weight

$$w(\{\sigma_{x,y,\tau}\}) = e^{-H_{\text{class}}(\{\sigma_{x,y,\tau}\})}.$$

Single updates

To create such a sample, we prepare an initial lattice in which all sites are occupied by the same state, which is randomly chosen. Then one Monte Carlo sweep does the following single updates

- go through all sites of the lattice

- for each site choose a random new state

- calculate probability of accepting this step. Let the current site be (x, y, τ), and its state $\sigma_{x,y,\tau}$, let the proposed state be $\sigma'_{x,y,\tau}$. If the new state creates a collision in real space or in imaginary time, then the move is rejected, otherwise the accpetance probability is

$$p = \min\left(1, \frac{w(\text{new})}{w(\text{old})}\right) \tag{3.7}$$

$$\frac{w(\text{new})}{w(\text{old})} = \frac{e^{-h(\ldots,\sigma'_{x,y,\tau},\ldots)}}{e^{-h(\ldots,\sigma_{x,y,\tau},\ldots)}} \tag{3.8}$$

$$\tag{3.9}$$

and so we can use directly the elements of the transfer matrices $T_1 T_2$:

$$\frac{w(\text{new})}{w(\text{old})} = \frac{\langle \sigma_{x,y,\tau-1} |\, T_1 T_2 \, | \sigma'_{x,y,\tau} \rangle \, \langle \sigma'_{x,y,\tau} |\, T_1 T_2 \, | \sigma_{x,y,\tau+1} \rangle}{\langle \sigma_{x,y,\tau-1} |\, T_1 T_2 \, | \sigma_{x,y,\tau} \rangle \, \langle \sigma_{x,y,\tau} |\, T_1 T_2 \, | \sigma_{x,y,\tau+1} \rangle}. \tag{3.10}$$

to decide whether a move is accepted or not, we only need to know the state of the site's nearest neighbors.

Cluster updates: flipping many sites at once

To speed things up, we also want to flip many sites at once. One simple way of doing this is to group a sequence of the same dipole state in imaginary time into one cluster, then propose a new dipole state for every site in this entire cluster. If this move does not create any collision in real space, then the acceptance probablility is simply given by

$$A(X \to Y) = \min\left(1, \frac{w(Y)}{w(X)}\right) = \min\left(1, \left(\frac{\langle \sigma' |\, \mathrm{T}_1 \, | \sigma' \rangle}{\langle \sigma |\, \mathrm{T}_1 \, | \sigma \rangle}\right)^{\mathrm{L_{cluster}}}\right),$$

where L_{cluster} is the length of the cluster.

Another update which flips many spins at once is the `FlipChainUpdate`. This update chooses a plane in (x,τ) direction. If no collisions are created throught this move, then every site pointing left is fliped to point right, and vice versa ($|4\rangle \leftrightarrow |2\rangle$). This update does not change the statistical weight of the configuration, and so it can always be accepted. A similar update exists in the (y,τ) plane, which flips $|1\rangle \leftrightarrow |3\rangle$. Because of the hard constraints in real space direction it is not straightforward to generalize the cluster updates used for example for the Ising model [38, 39] to this system.

Detailed balance

This procedure will sample a system at equilibrium if the following condition is fulfilled [40, 41]

$$\frac{N_e(X)}{N_e(Y)} = \frac{w(X)}{w(Y)} = \frac{P(Y \to X)}{P(X \to Y)}$$

where X and Y stands for configurations, $N_e(X)$ is the equilibrium probability of being in that configuration, and $P(X \to Y)$ is the probability that a walker will make a transition to Y if it is in X, this is

$$P(X \to Y) = T(X \to Y)A(X \to Y)$$

where T is the probability of making a trial step $(X \to Y)$, and A is the probability of accepting that step,

$$A(X \to Y) = \min\left(1, \frac{w(\mathrm{Y})}{w(\mathrm{X})}\right)$$

For our single updates we have $T = \mathrm{const}$ (each of the four other states is chosen with the same probability), and thus detailed balance is fulfilled.

Once we have produced the configurations according to their statistical weight, we can measure correlation functions in real space and in imaginary time, and the order parameters defined in Section 3.1.4.

3.2.3 Quantum Monte Carlo Results

Phase diagram

Results of the QMC simulations are summarized in the phase diagram shown in Figure 3.3. We find no phase transition[4] along the line of diagonal tilt, $\Delta_x = \Delta_y$. The disordered dipole state described in Section 2.4.1 for $\Delta_x, \Delta_y \to -\infty$ appers to be continuously connected to the parent Mott insulator at $\Delta_x, \Delta_y \to +\infty$. There is a critical line where the system undergoes a transition to an ordered state with *one dimensional* order along individual chains. For $\Delta_y < \Delta_x$ these chains are aligned in y direction (lower right corner of the phase diagram in Fig. 3.3), and $\langle\langle M_{\mathrm{UD}}^2\rangle\rangle \neq 0$, while $\langle \vec{M}^2\rangle = \langle \vec{M}_{\mathrm{stagg,x}}^2\rangle = \langle \vec{M}_{\mathrm{stagg,y}}^2\rangle = 0$. We will show below that the system indeed seems to be disordered in transverse direction; it looks like each chain has a two fold degenerate ground state, which is independenet of the order parameters of the neighboring chains, and so the two-dimensional system has a ground state degeneracy 2^{L_x}, where L_x is the linear system size in x direction, i.e. the number of chains. Correlations in x directions decay exponentially with a correlation length that is less than the lattice spacing $\xi_x \ll a$. There is no region in the phase diagram where either $\langle \vec{M}^2\rangle$, Eq. 3.6, or $\langle \vec{M}^2_{\mathrm{stagg,x}}\rangle$ or $\langle \vec{M}^2_{\mathrm{stagg,y}}\rangle$ takes a non-zero value.

Binder cumulant

The binder cumulant gives a good estimate for the critical point, and it does not depend on critical exponents [42]. For an Ising order parameter, M, the binder cumulant

---

[4]extracting the gap from imaginary time correlations (not shown) shows that the system remains gapped everywhere along this line.
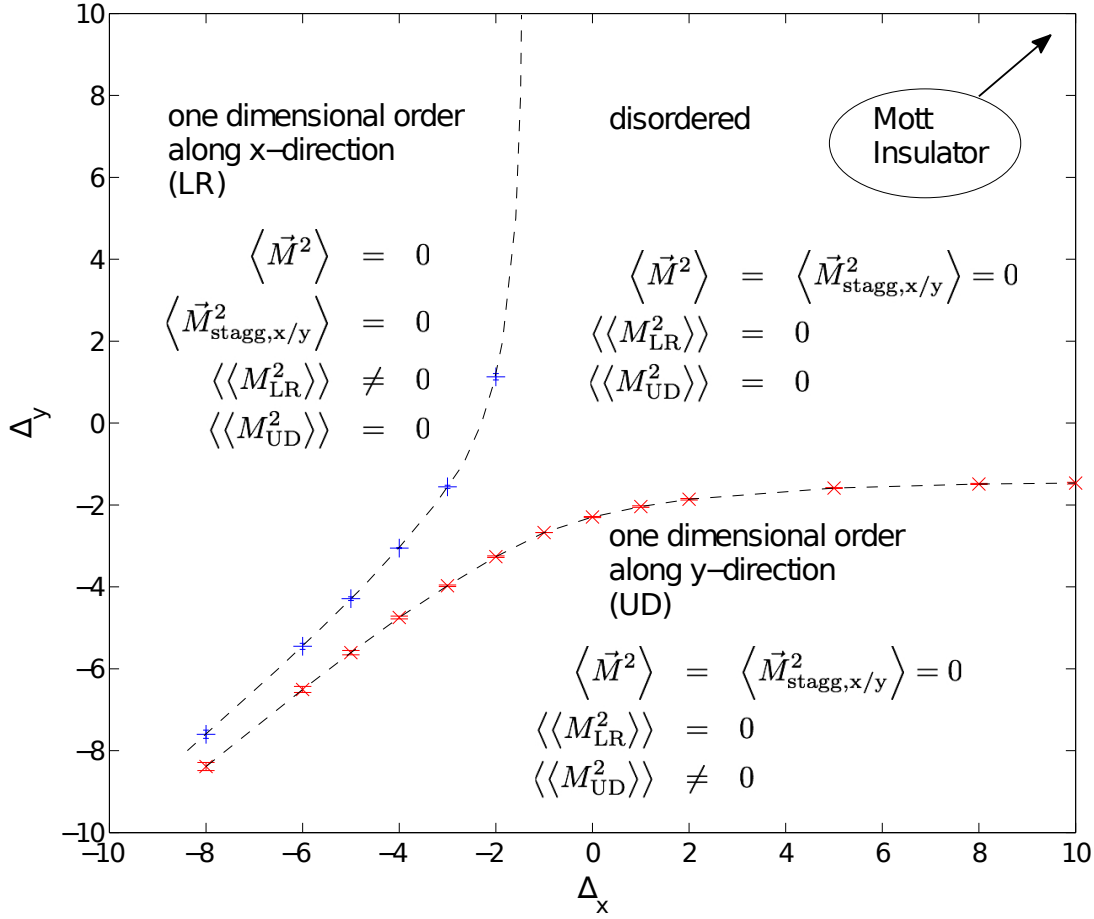
Figure 3.3: Phase diagram obtained from QMC study. The phase boundary was obtained from crossing of the binder cumulant of the pseudo-magnetization, see text. Square lattice of size $L_x = L_y = (4, 8, 16, 32, 64)$ the imaginary time slice thickness was $a = 0.04$, imaginary time direction was scaled with the linear system size, $M_\tau = (40, 80, 160, 320, 640)$, corresponding to temparatures $T = (0.625, 0.3125, 0.1562, 0.0781, 0.0391)$. Essentially the same phase diagram is obtained from order parameter scaling assuming the Ising exponent $\eta = 1/4$.

is defined as

$$U = 1 - \frac{\langle M^4 \rangle}{3 \langle M^2 \rangle^2}.$$

When the binder cumulant is plotted for different system sizes, all curves should cross at the critical point for the following reason. While for an infinite system the magnetization vanishes at the critical point as

$$M \propto (-\tau)^\beta,$$

where τ is the reduced temperature $\tau = T/T_c - 1$, ξ is the correlation length, β is the critical exponent of the magnetization, and ν is the correlation length exponent. For a finite system there are corrections to scaling, described by a scaling function ϕ, which only depends on ξ/L,

$$M = (-\tau)^\beta \phi(\xi/L) = (-\tau)^\beta \tilde{\phi}\left(\tau L^{1/\nu}\right)$$

We used $\xi = \tau^{-\nu}$ to rewrite the scaling function for a different argument. The average magnetization squared, and raised to the fourth power, have different scaling functions,

$$\langle M^2 \rangle = (-\tau)^{2\beta} u_2 \left(\tau L^{1/\nu}\right)$$
$$\langle M^4 \rangle = (-\tau)^{4\beta} u_4 \left(\tau L^{1/\nu}\right)$$

and so the binder cumulant is a function of this same argument, $\tau L^{1/\nu}$

$$U(\tau, L) = 1 - \frac{u_4 \left(\tau L^{1/\nu}\right)}{3 \left(u_2 \left(\tau L^{1/\nu}\right)\right)^2} = f\left(\tau L^{1/\nu}\right), \tag{3.11}$$

At the critical point we have $\tau = 0$, and so the binder cumulant at this point should not depend on system size[5]. In the thermodynamic limit for an Ising system in the ordered phase $U \to \frac{2}{3}$, and $U \to 0$ in the disordered phase. Fig. 3.4 shows the binder cumulant of the one dimensional order parameters $\langle\langle M_{LR}^2 \rangle\rangle$ and $\langle\langle M_{UD}^2 \rangle\rangle$ for different cuts through the phase diagram.

Order parameter scaling and the critical exponent η

The phase transition point can also be found from order paramter scaling. This will depend on the correlation length exponent, η. Let M again be an Ising order parameter,

---

[5]there are of course higher order corrections to scaling, and so for very small systems we do not expect the crossing points to agree exactly
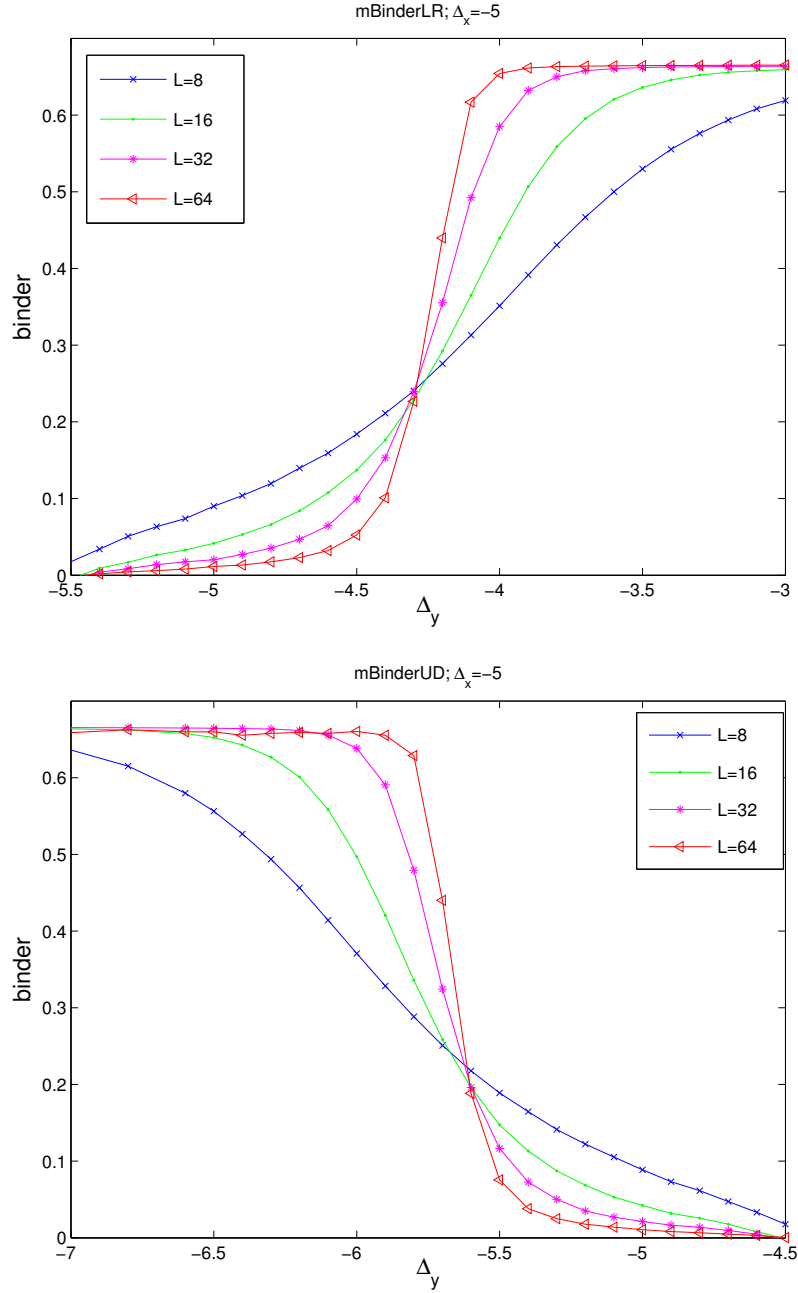
Figure 3.4: Binder cumulant for order parameters $\langle\langle M_{\mathrm{LR}}^2\rangle\rangle$ and $\langle\langle M_{\mathrm{UD}}^2\rangle\rangle$ for a horizontal cut through the phase diagram, keeping $\Delta_x = -5$ fixed, plotted for different system sizes, $L_x = L_y = 4$, 8, 16, 32, 64.

Figure 3.5: Binder cumulant of $\langle\langle M_{\mathrm{UD}}^2\rangle\rangle$ along different cuts throught the phase diagram: here $\Delta_x = 10$ and $\Delta_x = -2$.

at the critical point the correlation decays as a power law,

$$\langle M(r)M(0)\rangle \quad \propto \quad |r|^{-(D-2+\eta)} = |\vec{r}|^{-(d+z-2+\eta)}$$
$$\langle M^2 \rangle \quad = \quad L^{-\eta}$$

here D is the dimension of the classical system, and $d = D + 1$ is the dimension of the quantum system, z is the dynamic critical exponent. The 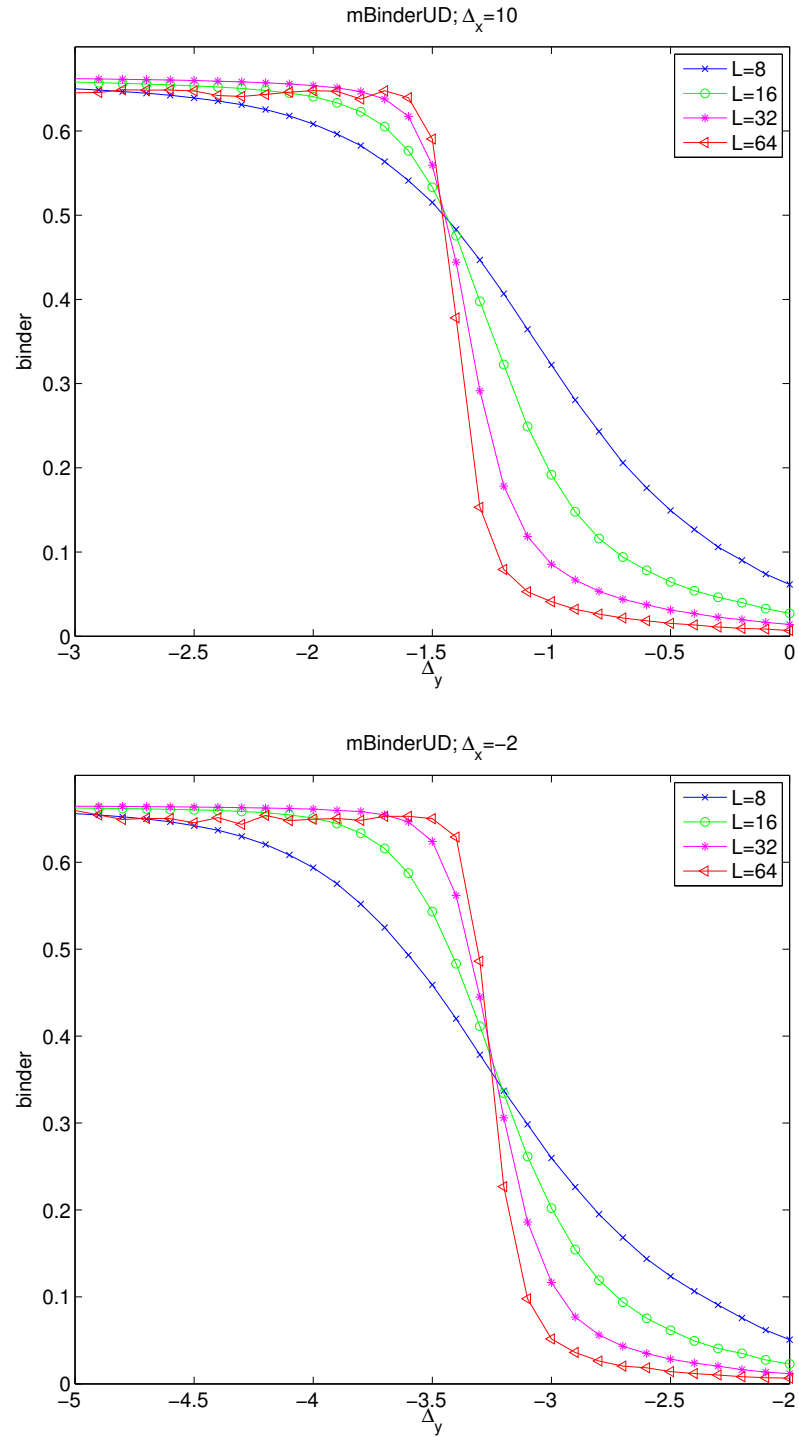correlation length exponent for the 2D classical Ising model is $\eta = 1/4$. In Figure 3.6 we plot $\langle\langle M_{LR}^2 \rangle\rangle L^{-1/4}$ and $\langle\langle M_{UD}^2 \rangle\rangle L^{-1/4}$ for different system sizes. The crossing point of these lines agrees with the one found from the binder cumulant.

Critical exponent ν

If we rescale the x axis for the binder cumulant, and plot it as a function of $(\lambda - \lambda_c) L^{1/\nu}$, then the data points for all system sizes should collapse. We indeed observe a good data collapse for the correlation length exponent of the classical two-dimensional Ising model, $\nu = 1$, see Fig. 3.7.

Absense of two-dimensional order

We probe for two-dimensional order by measuring $\langle \vec{M}^2 \rangle$. This quantity scales with system size exactly as a collection *randomly* aligned magnetized one dimensional chains. This suggests that there is no two-dimensional order: while in some regions of the phase diagram there is long range order along individual chains, there is no two dimensional order, see Figure 3.8.

Discussion

- The decorated square lattice can be regarded as a collection of one dimensional chains both in x direction and in y direction which cross and interact with each other via the hard constraint.

- For an unisotropic tilt, e.g. $\Delta_x < \Delta_y < 0$ we focus on chains aligned in the direction of stronger tilt, here the x direction. The only way two parallal chains can interact is via the hard constraint of the more expensive dipoles in the y direction.
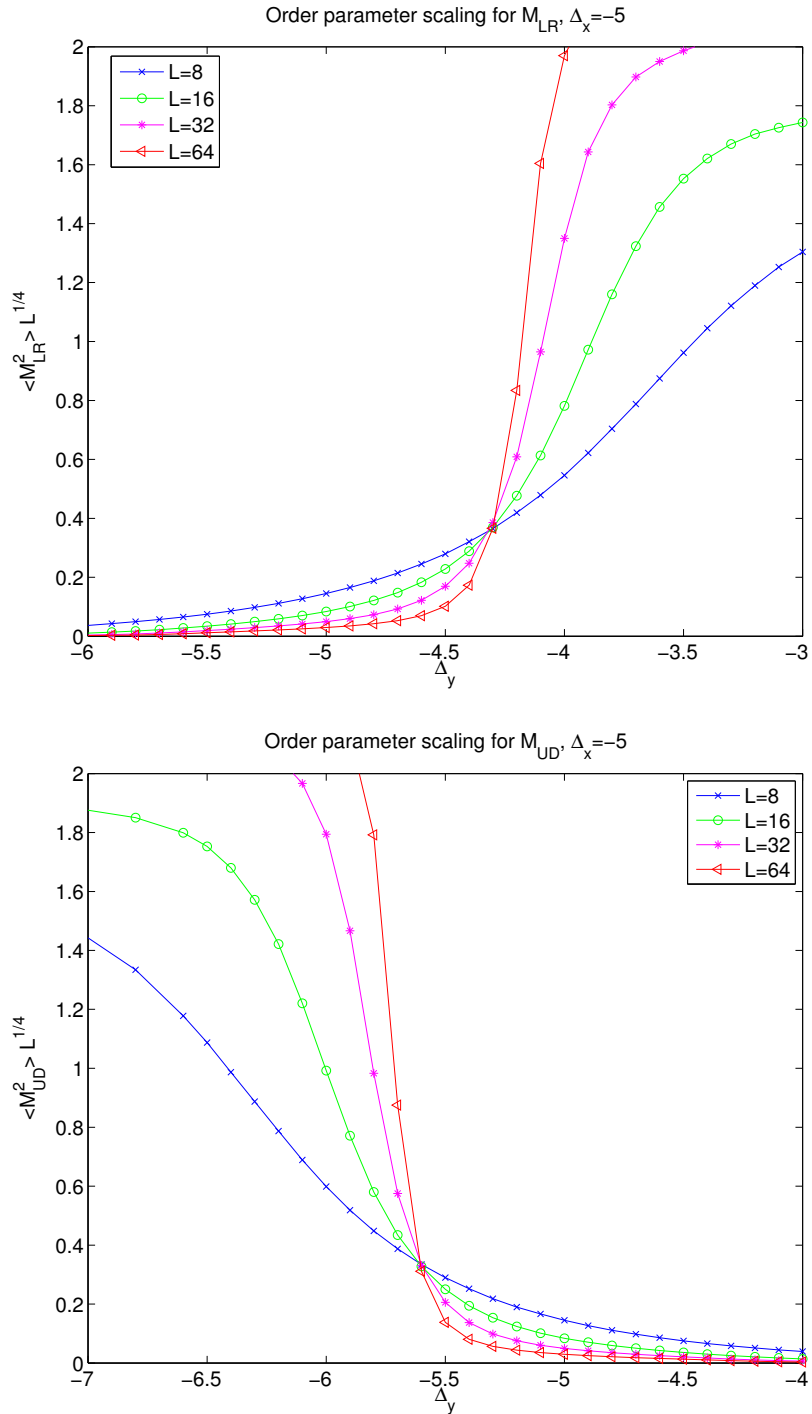
Figure 3.6: Order parameter scaling, assuming the correlation length exponent $\eta = 1/4$ of the classical two-dimensional Ising model. Good agreement of the crossing points, also with the ones found from the binder cumulant.
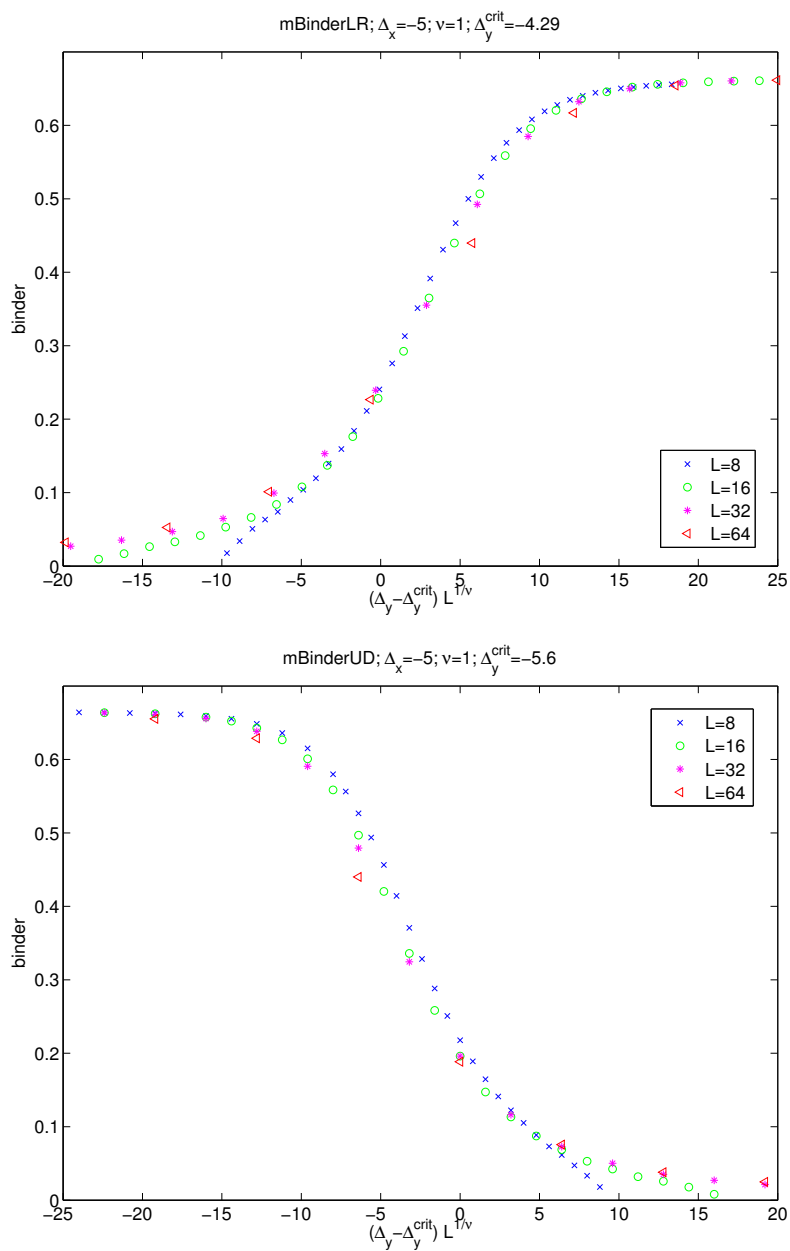
Figure 3.7: Data collapse for the critical exponent $\nu = 1$ of the classical two-dimensional Ising model. The x axis is centered around the critical point and rescaled by $L^{1/\nu}$
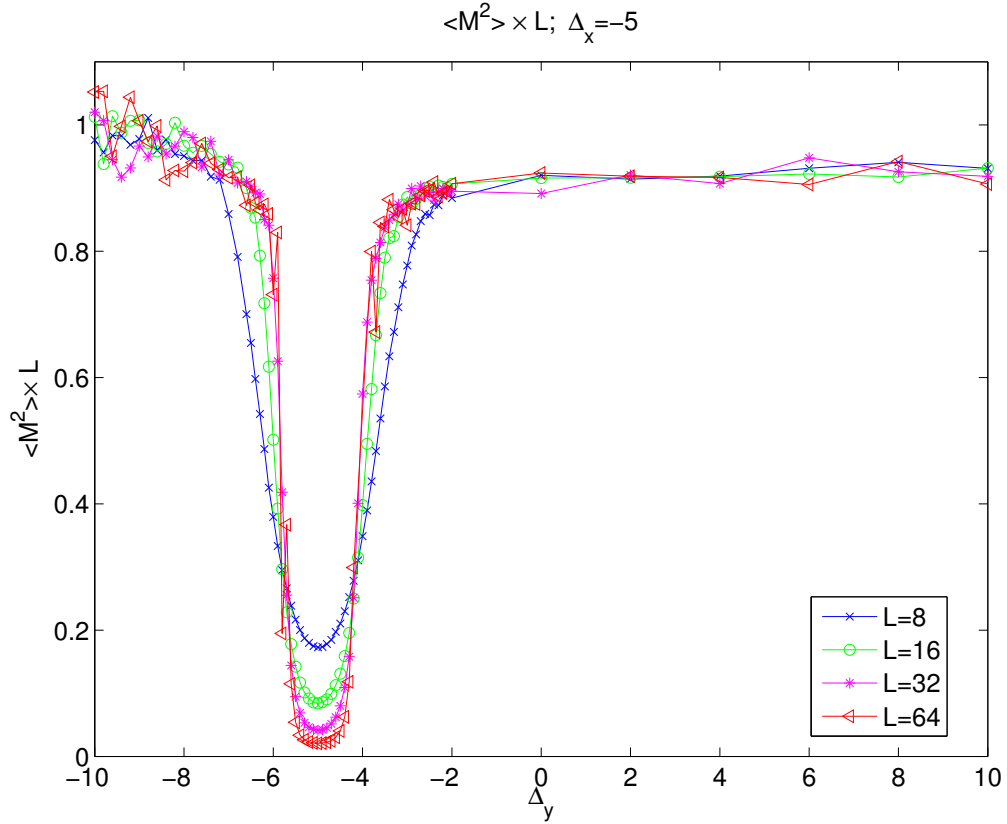
Figure 3.8: Scaling of the total magnetization with system size, $\langle \vec{M}^2 \rangle \times L$. For randomly aligned magnetized chains we expect $\langle \vec{M}^2 \rangle \propto 1/L$, while for perfectly aligned chains $\langle \vec{M}^2 \rangle =$ const and for antiferromagnetic order in transverse direction $\langle \vec{M}^2 \rangle = 0$. In the disordered phase $\langle \vec{M}^2 \rangle \propto 1/(L_x L_y)$. This plot shows that in the ordered phase the system behaves as a collection of independent chains with one dimensional order within each chain. Similar results are obtained for different cuts through the phase diagram.

- If $\Delta_y > 0$ these transverse dipole are associated with an energy cost compared to the vacuum state, and so we expect the constraint of those dipols to have little effect on the system, thus we expect the interchain coupling – if at all present – to be small.

- Critical exponents of the 2D classical Ising model (Onsager exponents) give a reasonalby good data collapse at all points along the critical lines.

- Quantum Monte Carlo results suggest that there is no coupling at all between the sign of the magnetization of the chains anywhere in the ordered phase.

3.3   Effective field theory close to the critical points

Let us now study the effective field theory close to the critical point. Motivated by results of the previous Chapters we start from uncoupled Ising chains. We will phrase our discussion for the critical line for $\Delta_x < \Delta_y$, in the left part of the phase diagram. Of course the phase diagram is symmetric about the diagonal axis $\Delta_x = \Delta_y$, and so all conclusions apply to the other critical line as well.

3.3.1   Microscopic model for the coupling between the chains

In a perfectly ordered phase, $\Delta_x \to -\infty$, $\Delta_y \to +\infty$, there are no dipoles in transverse direction, and therefore there can not be any coupling between the chains. Each chain has its own independent order parameter, and all unit cells of each chain have the same state, which does not depend on the neighbors. However, for finite values of Δ_y neighboring chains can feel each other trough domain wall excitations.

In each chain there are two different domain walls which always come in pairs. We will refer to them as *visible* and *invisible* domain walls, see Fig. 3.9

- visible domain walls change the sign of the order parameter from $\to$ to $\leftarrow$, and to avoid the hard constraint there has to be at least one central site which cannot be part in a horizontal dipole bond. There is an energy cost associated with these domain walls. Furthermore there is an additional energy cost if two neighboring chains both have a visible domain wall at the same x coordinate,

- invisible domain walls change the sign of the order parameter from $\leftarrow$ to $\to$, and all participating central sites may still have a horizontal dipole. There is no energy cost
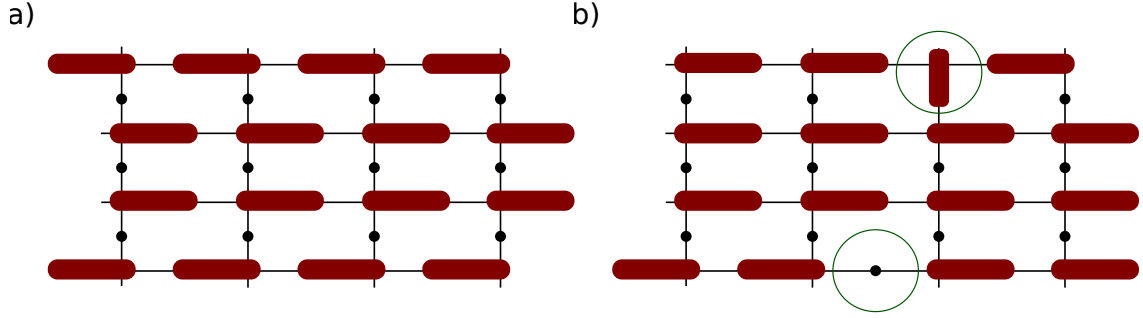
a) b)

Figure 3.9: a) Perfectly ordered state which is a ground state in the limit $\Delta_x \to -\infty$, $\Delta_y \neq -\infty$. In this state there are no dipoles in y direction, and so there cannot be any coupling between the chains. The ground state degeneracy in this limit is 2^{L_y} and the system is well described by a collection of uncoupled Ising chains. b) Two different kinds of domain wall excitation. We will refer to the kind shown in the top row as 'visible' domain walls, as there is one unit cell which cannot have a dipole aligned in x direction. This unit cell will reduce its energy by fluctuating between the states zero, up, and down. The neighboring chains can see this domain wall as it takes away sites for them to fluctuate: it is energetically favorable for them not to have the same kind of domain wall at the same x coordinate. An 'invisible' domain wall, which costs no energy, is shown in the bottom row. This kind of domain wall cannot be seen by the neighboring chains. Note that these two different kinds of domain wall always come in pairs.

associated with such domain walls, and neighboring chains cannot see it.

In the language of an Ising model

$$
\begin{aligned}
\Delta\sigma_i^z &= \sigma_{i+1}^z - \sigma_i^z = +2 \qquad : \qquad \text{visible domain wall} \\
\Delta\sigma_i^z &= \sigma_{i+1}^z - \sigma_i^z = -2 \qquad : \qquad \text{invisible domain wall}
\end{aligned}
$$

and the interaction between visible domain walls takes the form

$$
H_{1,2} = \frac{1}{16} \Delta\sigma_{1,i}^z \left(\Delta\sigma_{1,i}^z + 2 \right) \Delta\sigma_{2,i}^z \left(\Delta\sigma_{2,i}^z + 2 \right).
$$

Here i is an index labeling the sites along each chain. Note that we need all these terms to project only onto visible domain walls. The sign of H_{12} is positive, and the magnitude of this coupling scales as $t_{\text{eff}} \propto \frac{t^2}{\Delta_x}$.

$$
\begin{aligned}
H_{1,2} &= \frac{1}{16} \left(\Delta\sigma_{1,i}^z \Delta\sigma_{1,i}^z + 2\Delta\sigma_{1,i}^z \right) \left(\Delta\sigma_{2,i}^z \Delta\sigma_{2,i}^z + 2\Delta\sigma_{2,i}^z \right) \\
&= \frac{1}{16} \left[\underbrace{\Delta\sigma_{1,i}^z \Delta\sigma_{1,i}^z \Delta\sigma_{2,i}^z \Delta\sigma_{2,i}^z}_{A} + 4 \underbrace{\Delta\sigma_{1,i}^z \Delta\sigma_{2,i}^z}_{B} + 2 \underbrace{\left(\Delta\sigma_{1,i}^z \Delta\sigma_{2,i}^z \Delta\sigma_{2,i}^z + \Delta\sigma_{2,i}^z \Delta\sigma_{1,i}^z \Delta\sigma_{1,i}^z \right)}_{C} \right]
\end{aligned}
$$

- Term A will give us an energy-energy coupling, $\sigma^z_{1i+1}\sigma^z_{1i}\sigma^z_{2i+1}\sigma^z_{2i}$, and a mass term $\sigma^z_{j,i}\sigma^z_{j,i+1}$ for each chain $j = 1, 2$, which will shift the position of the critical point,

$$\Delta\sigma^z_{1,i}\Delta\sigma^z_{1,i} = \left(\sigma^z_{1,i+1} - \sigma^z_{1,i}\right)\left(\sigma^z_{i+1} - \sigma^z_i\right) = 2 - 2\sigma^z_{1,i+1}\sigma^z_{1,i}$$

$$
\begin{aligned}
A &= \Delta\sigma^z_{1,i}\Delta\sigma^z_{1,i}\Delta\sigma^z_{2,i}\Delta\sigma^z_{2,i} = 4\left(1 - \sigma^z_{1,i+1}\sigma^z_{1,i}\right)\left(1 - \sigma^z_{2,i+1}\sigma^z_{2,,i}\right) && (3.12) \\
&= 4\left(1 - \sigma^z_{1,i+1}\sigma^z_{1,i} - \sigma^z_{2,i+1}\sigma^z_{2,i} + \sigma^z_{1,i+1}\sigma^z_{1,i}\sigma^z_{2,i+1}\sigma^z_{2,i}\right) && (3.13)
\end{aligned}
$$

In the following we will consider the RG flow of the energy-energy term, and bosonize it. Note that this term is symmetric under a sign change of the order parameter of a single chain, $\sigma_{1i} \to -\sigma_{1i}, \sigma_{2i} \to -\sigma_{2i}$, and so it cannot generate an order parameter coupling, which does not have this symmetry.

- Term B is irrelevant by counting scaling dimensions, $[\lambda_B] = -1/4$. However, this one may generate an order parameter - order parameter coupling $\sigma^z_1\sigma^z_2$ between two neighboring chains. In the continuum limit it will become

$$H_B = \lambda_B \int dx \partial_x \sigma^z_1(x)\partial_x\sigma^z_2(x). \qquad (3.14)$$

It is not easy to bosonize this term: it becomes non-local after the Jordan-Wigner transfrom due to the string operator.

3.3.2   Renormalization group flow equations of the coupling constants

Now we study the flow of the coupling constants under RG. We consider the Hamiltonian of two coupled chains with the couping terms we found above from the microscopic Hamiltonian

$$H = H_1 + H_2 + \lambda_{ee}\sigma^z_1(x+a)\sigma^z_1(x)\sigma^z_2(x+a)\sigma^z_2(x) + \lambda_B\partial_x\sigma^z_1(x)\partial_x\sigma^z_2(x)$$

here H_1 and H_2 stand for each of the two chains. In the continuum limit, after a Jordan Wigner[6] transformation, each chain can be described by the field theory [43]

$$H_j = \int dx \left[\frac{c}{2}\left(\psi^\dagger_j\partial_x\psi^\dagger_j - \psi_j\partial_x\psi_j\right) + \Delta\psi^\dagger_j\psi_j\right] \qquad (3.15)$$

At the critical point we have $\Delta = 0$.

---

[6]after Jordan-Wigner transform the operators within the same chain have fermionic commutation relations. Operators of different chains still *commute* $[\psi_1(x), \psi_2(x')] = 0$. This is because the string operator is defined in each chain separately. This will not matter because the Hamiltonian only contains pairs of operators of each chain.

Generating an order parameter - order parameter coupling

The microscopic model does not have any term coupling the order parameters of two neighboring chains. But the term Eq. (3.14) will generate such an order parameter coupling term, if this is not forbidden by a hidden microscipic symmetry.

We can describe the low energy effective field theory of each chain by a field theory of a real field, which is symmetric under $\sigma \to -\sigma$, and so let each chain j be described by

$$H_j = \left(\nabla \sigma_j^z\right)^2 + r\left(\sigma_j^z\right)^2 + u\left(\sigma_j^z\right)^4 \tag{3.16}$$

then the following two terms will generate the order parameter coupling

$$H_B = \lambda_B \int \frac{dk}{2\pi} k^2 \sigma_1^z(k)\sigma_2^z(k) \tag{3.17}$$

$$H_{ee} = \lambda_e e \int \frac{dk_1}{2\pi} \int \frac{dk_2}{2\pi} \int \frac{dk_3}{2\pi}\frac{dk_4}{2\pi} \sigma_1^z(k_1)\sigma_1^z(k_2)\sigma_2^z(k_3)\sigma_2^z(k_4)\delta(k_1 + k_2 + k_3 + k_4)$$

in momentum shell RG

$$\lambda_{oo}\sigma_1(k_1)\sigma_2(k_3)\left\langle \int_{\Lambda/b}^{\Lambda} \frac{dk_2}{2\pi}\frac{dk}{2\pi} k^2 \sigma_1^z(k)\sigma_2^z(k)\sigma_1(k_2)\sigma_2^z(-k_1 - k_2 - k_3)\right\rangle. \tag{3.18}$$

This term is relevant, the scaling dimension of the coupling constant is $[\lambda_{oo}] = 7/4$. This term would cause neighboring chains to align (either ferromagnetically or antiferromagnetically).

Marginal energy - energy coupling: continuous change of critical exponent ν

Since we do not see any two-dimensional order in QMC we will also study the next most relevant term

$$\sigma_1^z(x)\sigma_1^z(x)\sigma_2^z(x)\sigma_2^z(x) \tag{3.19}$$

then using the operator product expansion we get the energy energy term

$$\sigma_1^z(x)\sigma_1^z(x) = 1 + \epsilon_1(x) = 1 + \psi_1^\dagger(x)\psi_1(x) \tag{3.20}$$

and so

$$\sigma_1^z(x)\sigma_1^z(x)\sigma_2^z(x)\sigma_2^z(x) = (1 + \epsilon_1(x))(1 + \epsilon_2(x)) \tag{3.21}$$

$$= 1 + \epsilon_1(x) + \epsilon_2(x) + \epsilon_1(x)\epsilon_2(x) \tag{3.22}$$

so there is a shift to the position of the critical point of each chain, and there is an energy energy coupling

$$\epsilon_1(x)\epsilon_2(x) = \psi_1^\dagger(x)\psi_1(x)\psi_2^\dagger(x)\psi_2(x) \tag{3.23}$$

the coupling λ has scaling dimension 0, using [43]

$$[\Delta] = 1, \qquad [\psi] = 1/2$$
$$[x] = -1, \qquad [\tau] = -z = -1$$
$$[\sigma^z] = 1/8, \qquad [\lambda] = 0$$

so from counting scaling dimension one finds this term to be marginal[7] , and so we need to look at the next order in the flow equations. The flow equations are

$$\frac{d\lambda_{\text{ee}}}{dl} = -\frac{\lambda_{\text{ee}}^2 \Delta^2}{\pi \left(\sqrt{1+\Delta^2}\right)^3},$$
$$\frac{d\Delta}{dl} = \Delta \left(1 - \lambda_{\text{ee}}\frac{1}{\pi\sqrt{1+\Delta^2}}\right). \tag{3.24}$$

it looks like the entire line $\lambda = 0$ is a fixed line. There is a continuously changing correlation length exponent ν, which is very unusual. The correlations length exponent[8] depends on the coupling strength as follows

$$\nu = \frac{1}{1 - D\lambda} \approx 1 + D\lambda + O(\lambda^2)$$

with $D = 1/\pi$.

---

[7]This works as follows: the important quantity is the scaling dimension $[\lambda]$ of the *coupling constant* in front of the operator. This determines whether or not the operator is relevant. If $[\lambda] > 0$ then this coupling constant grows under scaling, and the operator is relevant. If $[\lambda] < 0$ then the operator is irrelevant, as the coupling constant becomes smaller in RG flow. All dimensions have to add up to zero, e.g. in $\int d\tau dx \lambda \hat{O}$, where $\hat{O}$ is some operator, then $[\tau] + [x] + [\lambda] + [\hat{O}] = 0$. Here we have $\hat{O} = \psi_1^\dagger\psi_1\psi_2^\dagger\psi_2$, $[\hat{O}] = 2$, and so $[\lambda] = 0$.

[8]ν is the correlation length exponent, $\xi^{-1} \sim \Lambda |g - g_c|^\nu$. It is defined as the inverse of the RG flow eigenvalue of the most relevant perturbation about a quantum critical point [43, 44].Without coupling, each Ising chain has $\nu = 1$. The relation between the scaling dimension A of the most relevant eigenvalue and the correlation length exponent ν can be seen as follows: starting from the flow equation $\frac{d\Delta}{dl} = A\Delta$, solve to obtain $\Delta(l) = \Delta_0 e^{Al} = \Delta_0(\Lambda_0/\tilde{\Lambda})^A$. Here Λ_0 is the original cutoff, and $\tilde{\Lambda}$ is the new cutoff. We used $e^l = \Lambda_0/\tilde{\Lambda}$. The relevant energy scale is that of $\tilde{\Delta}$ when $\Delta(l) \approx \Lambda_0$. Then Δ is no longer a small perturbation and the system enters a new phase. So we need to solve for the $\tilde{\Lambda}$, the gap scales like this. $\tilde{\Lambda} = \Lambda_0(\Delta_0/\Lambda_0)^{1/A}$. And so gap $\sim \Delta_0^{1/A} = |g - g_c|^{1/A}$. By definition [43] gap $\sim |g - g_c|^{\nu z}$; gap $\sim \xi^{-z}$. This system has $z = 1$, and so $\nu = 1/A$. To first order A is the scaling dimension of the coupling constant of the most relevant operator.

Bosonization

Each chain can be described by one Majorana fermion. Two chains can be combined and described by one Dirac fermion, which we can then bosonize. Starting from Eq. 3.15 we write ψ as one majorana fermion with left moving and right moving part $(\alpha = \frac{1}{\sqrt{2}}(\chi_R + \chi_L); \beta = \frac{1}{\sqrt{2}}(\chi_R - \chi_L).)$

$$\psi_j = \alpha + i\beta = \frac{1+i}{\sqrt{2}}\chi_{j,R} + \frac{1-i}{\sqrt{2}}\chi_{j,L} \tag{3.25}$$

$$\psi_j^\dagger = \alpha - i\beta = \frac{1-i}{\sqrt{2}}\chi_{j,R} + \frac{1+i}{\sqrt{2}}\chi_{j,L} \tag{3.26}$$

while the ψ operators have the usual fermionic anti-commutation relations, and $\psi^2 = 0$, the majorana fermions are real, and fulfill $\chi_R^\dagger = \chi_R$, and thus $\chi_R^2 = 1$. The Hamiltonian for each chain is

$$H_j = \int dx \left[\frac{c}{2} \left(-i\chi_{jR}\frac{\partial \chi_{jR}}{\partial x} + i\chi_{jL}\frac{\partial \chi_{jL}}{\partial x} \right) \right] + i\Delta\chi_L\chi_R \tag{3.27}$$

and the energy-energy coupling

$$H_{12} = -\chi_{1L}(x)\chi_{1R}(x)\chi_{2L}(x)\chi_{2R}(x) \tag{3.28}$$

Now we combine two Majorana fermions to one Dirac fermion $\psi = \psi_R + \psi_L$ (note this is not the same ψ as in Eq. 3.15)

$$\chi_{1R} = \psi_R + \psi_R^\dagger \tag{3.29}$$

$$\chi_{2R} = \frac{1}{i}\left(\psi_R - \psi_R^\dagger\right) \tag{3.30}$$

and same for the left-movers. The uncoupled Hamiltonian $H_1 + H_2$ becomes a Dirac fermion with a mass term that vanishes at the critical point:

$$H_1 + H_2 = \int dx 2c \left[-i\psi_R^\dagger \frac{\partial \psi_R}{\partial \psi_L^\dagger} + i\frac{\partial \psi_L^\dagger}{\partial \psi}_L \right] + 2i\Delta \left(-\psi_L^\dagger\psi_R + \psi_R^\dagger\psi_L \right) \tag{3.31}$$

$$H_{12} = \left(\psi_L + \psi_L^\dagger\right)\left(\psi_R + \psi_R^\dagger\right)\left(\psi_L - \psi_L^\dagger\right)\left(\psi_R - \psi_R^\dagger\right) \tag{3.32}$$

using boson fields

$$\psi_R = \lim_{\alpha \to 0} \frac{1}{\sqrt{2\pi\alpha}}e^{-i(\phi-\theta)} \tag{3.33}$$

$$\psi_L = \lim_{\alpha \to 0} \frac{1}{\sqrt{2\pi\alpha}}e^{-i(\phi+\theta)} \tag{3.34}$$

we find the bosonized form ($\hat{\Pi}(x) = \frac{1}{\pi}\nabla\theta(x)$), here $K = 1$

$$H_1 + H_2 = \frac{1}{2\pi} \int dx \left[cK \left(\pi\Pi(x)\right)^2 + \frac{c}{K} \left(\nabla\phi(x)\right)^2 \right] + \frac{4\Delta}{\alpha} \sin(2\phi(x)) \tag{3.35}$$

the term coming from the coupling gives many contributions, most of them are irrelevant. In this notation

$\cos(A\phi)$ and $\sin(A\phi)$ are relevant if $K < \frac{8}{A^2}$,

$\cos(A\theta)$ and $\sin(A\theta)$ are relevant if $K > \frac{A^2}{8}$

Contributions from H_{12}:

- most importantly there is an interaction term

$$\psi_L\psi_R\psi_L^\dagger\psi_R^\dagger + \text{H.c.} = \frac{2}{(2\pi)^2} \left[(\nabla\phi)^2 - (\nabla\theta)^2\right],$$

  which will renormalize the Luttinger parameters

$$u = c\sqrt{1 - \left(\frac{\lambda}{\pi c}\right)^2} \tag{3.36}$$

$$K = \sqrt{\frac{1 + \lambda/(\pi c)}{1 - \lambda/(\pi c)}} \approx 1 + \frac{\lambda}{\pi c} + O(\lambda^2) \tag{3.37}$$

- there is a term that is marginal at $K = 1$, but irrelevant at $K \neq 1$

$$\psi_L\psi_R\psi_L^\dagger\psi_R + \text{H.c.} \rightarrow \cos(2(\phi - \theta)),$$

  which has scaling dimension $K + \frac{1}{K}$, and so it is relevant for $K + \frac{1}{K} < 2$. It is marginal at $K = 1$ and becomes irrelevant as soon as $K \neq 1$.

- other terms are $\cos(4\phi)$ and $\cos(4\theta)$, and those are irrelevant.

so the main effect of the coupling is the change of the Luttinger parameters. This affects the flow equation of Δ:

$$\frac{d\Delta(l)}{dl} = \Delta(l)(2 - K) = \Delta(l)\left(1 - \frac{\lambda}{\pi c}\right) \tag{3.38}$$

this agrees with Eq. 3.24

Relation ot the Ashkin-Teller model

This model of two chains with an energy-energy coupling is related to the so called Ashkin Teller model [45, 27], which also predicts a continuously changing correlation length exponent.

3.3.3 Discussion

While in the perfectly ordered state different chains cannot see the sign of each other's order parameters, there is a repulsion between certain kinds of domain walls. The effective field theory analysis has shown that his term generates an order parameter order parameter coupling under RG flow, which is relevant and should cause the chains to order. This term also contains an energy-energy coupling, which for two coupled chains changes the correlation length exponent ν. Additionally a term which shifts the location of the critical point of each is generated.

3.4 Coupled or uncoupled chains: Exact diagonalization study

Quantum Monte Carlo results show a system which decouples into a collection of one dimensional chains, while a field theory analysis suggests that a coupling between the chains should be generated. The following scenarios might explain this disagreement

- *hidden symmetry*: there could be a subtle microscopic symmetry which forbids any coupling between the order parameters of the chains. The next relevant term is then the energy-energy coupling, which leads to a change of the critical exponent ν but no ordering of the chains; or

- *finite size effects:* the coupling between the chains could be present, but too small to see at the system size studied with QMC. Simulating larger lattices should then, in principle, find a phase with two-dimensional order.

We expect the coupling between the chains to be most important in the regime $\Delta_y < 0$, where dipoles in direction transverse to the chains are prefered to the zero-dipole state. Here we resolve this question by an exact diagonalization study of a toy model, which consists of two chains and qualitatively captures the interchain constraint, and thus the coupling, if present.

3.4.1 Toy model

We use a simplified model, instead of five states, there are only three dipole states in every unit cell, see Figure 3.10 . The state with no dipole has been integrated out[9], while

---

[9]this of course only works for $\Delta_x, \Delta_y < 0$

one of the horizontal dipole states is missing: this enhances the coupling and reduces the size of the Hilbert space, which enables us to study longer chains. We expect this toy model to qualitativley describe the interchain coupling of our system.
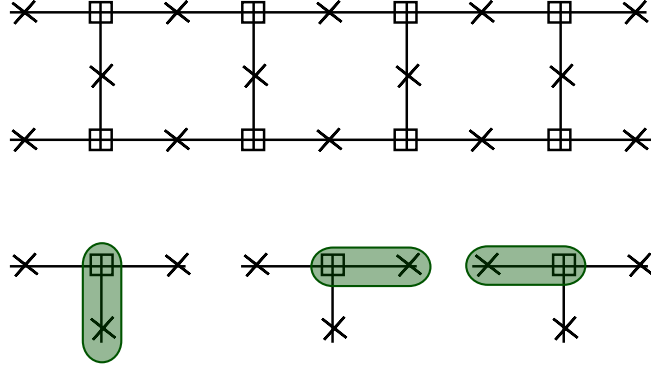

Figure 3.10: Two chain model. Each central site (marked with a square) can be in one out of three states. A chain of length 4 is shown. This model should capture the interchain behavior of our model qualitatively.

The Hamiltonian for each of these unit cells reads

$$H_{\text{site}} = \begin{pmatrix} \Delta_b & t_b & t_b \\ t_b & \Delta_a & t_a \\ t_b & t_a & \Delta_a \end{pmatrix}$$

where Δ_a is the energy cost for a dipol along chain direction, and Δ_b is the energy cost for a dipole in direction transverse to the chains. The effective hopping elements t_a, and t_b are obtained from second order perturbation theory, and they both have a negative sign (since $\Delta_a < \Delta_b < 0$).

$$\begin{aligned} t_b &= \frac{1}{2} t^2 n_0 \left(n_0 + 1\right) \left(\frac{1}{\Delta_a} + \frac{1}{\Delta_b} \right), \\ t_a &= \frac{n_0 \left(n_0 + 1\right) t^2}{\Delta_a}, \end{aligned}$$

and we work in units where $t\sqrt{n_0(n_0+1)} = 1$. In addition to the single site Hamiltonian, there is the hard-core constraint that two central sites cannot point towards each other. This constraint reduces the size of the Hilbert space. The size of the Hilbert space for any chain lenght L can be computed exactly using transfer matrices, see Table 3.1. For long chains it grows as $\dim(H) \sim 5.35^L$.

3.4.2 Results

We diagonalized this system for a chains of up to length nine[10], with periodic boundary conditions. At first sight these results do suggest that these chains are not coupled: it looks like there are four ground states. However, we also observe an energy density associate with ferromagnetic order. For the system sizes we were able to diagonalize, however, this energy density is much smaller than the effective hopping element of the order parameter of each chain, and thus smaller than the finite size gap of each chain.

Gap to the first few excited states: looks like four ground states

Diagonalizing this system for several points in the ordered phase shows a scaling of the gap to the first three excited states which strongly suggests that the system has four ground states. We compare this to two isolated chains, which show a very similar scaling, see Fig. 3.11

Scaling of the gap: looks like independent Ising transitions

For an infinite system close to the critcal poing the gap should behave as $\Delta_{\text{gap}} \sim |\lambda - \lambda_c|^{\nu} = \xi^{-z}$, where λ is the tuning parameter, and λ_c is its critical value. For a finite system, there is a scaling function, which depends only on the ration ξ/L

$$\Delta_{\text{gap}} = E_1 - E_0 = |\lambda - \lambda_c|^{z\nu} \tilde{\phi}(\xi/L) = |\lambda - \lambda_c|^{z\nu} \frac{L^{-z}}{L^{-z}} \tilde{\phi}\left(|\lambda - \lambda_c|^{-\nu}/L\right)$$
$$= L^{-z} f\left(L|\lambda - \lambda_c|^{\nu}\right) = L^{-z} \phi\left(L^{1/\nu}(\lambda - \lambda_c)\right)$$

and so if we plot $(E_1 - E_0)L^{-z}$ for different system sizes, all curves should cross at the critical point. Here we expect $z = 1$. By rescaling also the y-axis, everything should collapse. This allows to measure the correlation length expoinent ν.

Even though this is a very small system, we can look at the scaling for different system sizes. Here I used $\Delta_y = -5$ fixed, and plot for different values of Δ_x, see Figures 3.13, and 3.14. I find good data collapse using the Ising exponents $z = 1$ and $\nu = 1$.

---

[10]while we can diagonalize chains of length nine in all regions of the phase diagram, in some regions the splitting between the lowest eigenvalues seems to become smaller than machine precision, this limits our analysis.

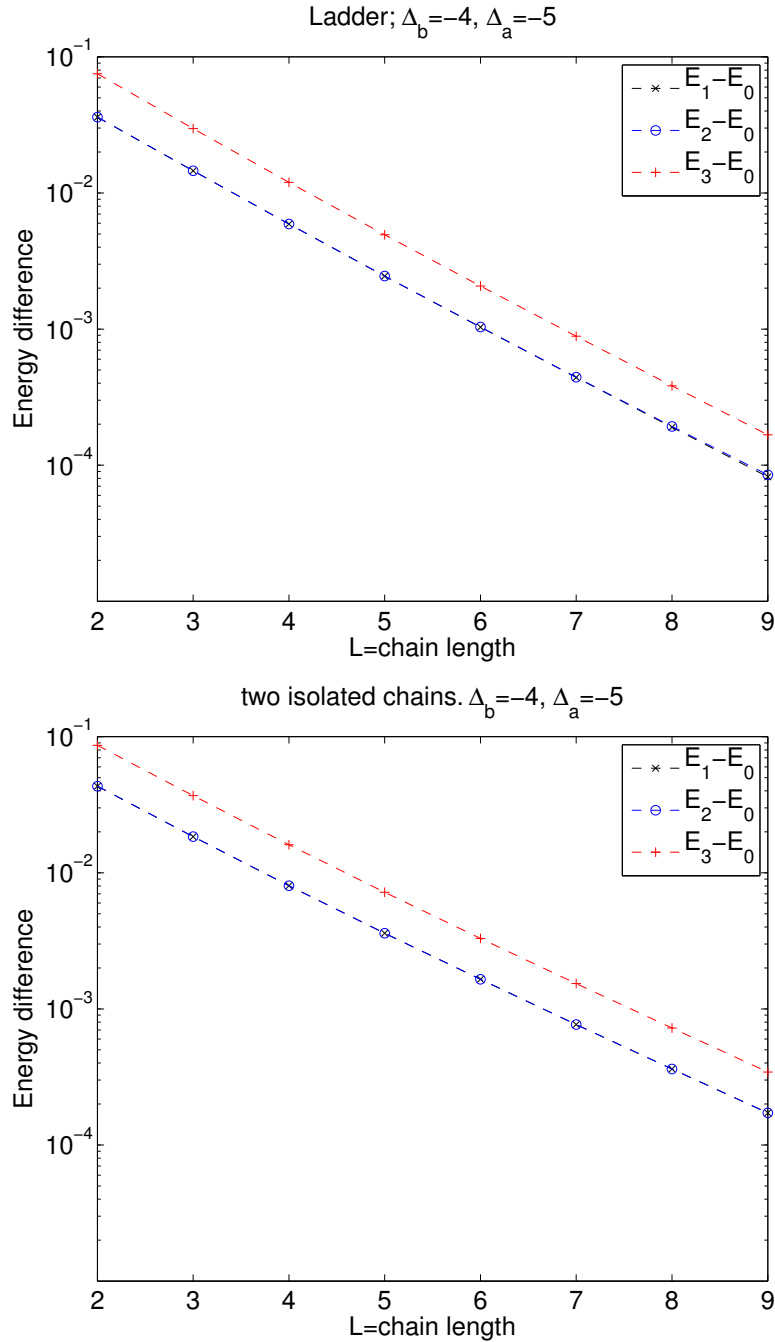Figure 3.11: Logarithmic plot for energy of the first three excited states relative to the ground state as a function of system length, for (a) one ladder as described above and for (b) two isolated chains. The lines $E_1 - E_0$ and $E_2 - E_o$ are on top of each other. This suggests that the order parameters of the chains are not coupled. Similar behavior is observed at other points in the ordered region of the phase diagram.
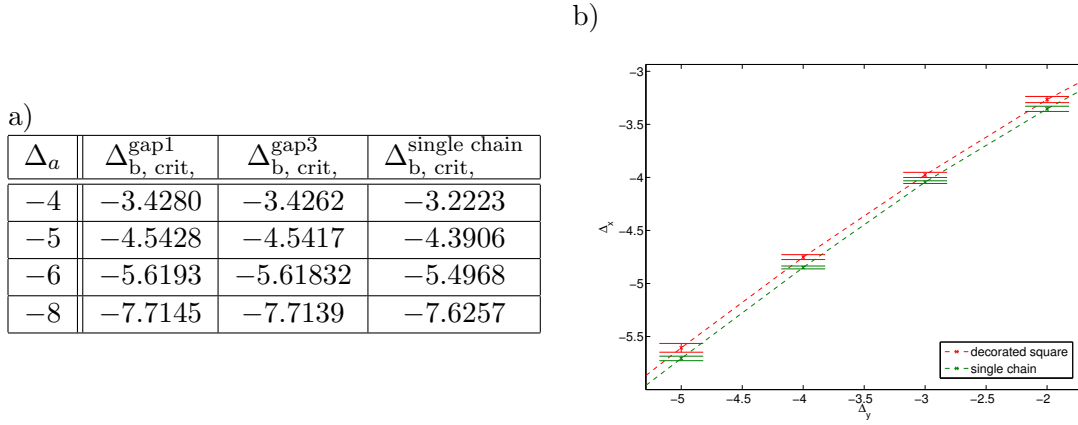
b)

a)

Δ_a	$\Delta_{\text{b, crit,}}^{\text{gap1}}$	$\Delta_{\text{b, crit,}}^{\text{gap3}}$	$\Delta_{\text{b, crit,}}^{\text{single chain}}$
-4	-3.4280	-3.4262	-3.2223
-5	-4.5428	-4.5417	-4.3906
-6	-5.6193	-5.61832	-5.4968
-8	-7.7145	-7.7139	-7.6257

Figure 3.12: Shift of critical point due to inter-chain coupling a) Exact diagonalization of the toy model: critical value $\Delta_{\text{b,crit}}$ for a system of two coupled chains to a system of two isolated chains. The critical point is shifted, so there is some effect due to the coupling. b) QMC: the figure shows the critical line of the decorated square lattice and the critical line of a single chain. We observe a similar shift of the critical line. The direction of the shift both from QMC and from exact diagonalization agrees with the field theory, Eq. (3.13)
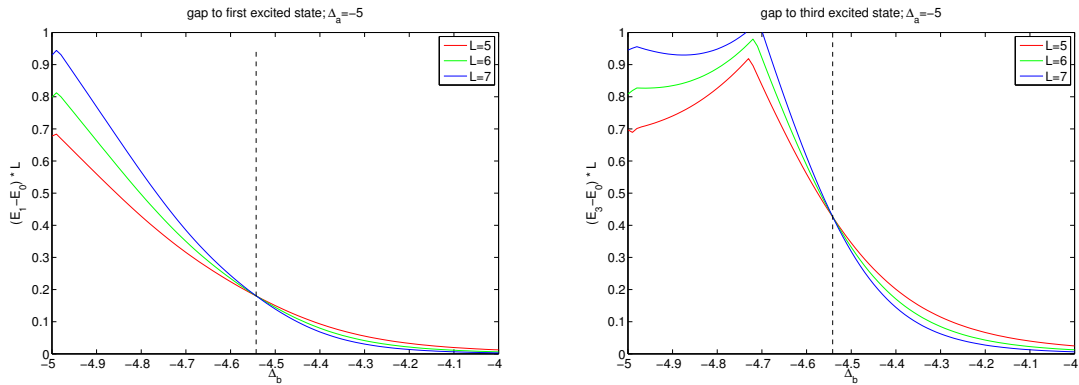
Figure 3.13: a) Spacing between the lowest two eigenvalues, as a function of Δ_x for various system sizes. b) spacing between the third eigenvalues and the ground state. The crossing points are almost equal, but not quite: $\Delta_{\text{x, crit,}}^{\text{gap1}} = -4.5428$, $\Delta_{\text{x, crit,}}^{\text{gap3}} = -4.5417$. If I did the same thing for two isolated chains, the crossing points would agree. The critical point for a single chain is *different,* it is $\Delta_{\text{x, crit}}^{\text{single chain}} = -4.3906$. So there is at least a shift to the critical point due to the presence of a second chain.

Figure 3.14: scaling for the gap to first excited state. $\Delta_{b,crit} = -4.5428$ was used; good data collapse with Ising exponents . Using a larger or smaller value for ν gives less good data collapse, see plots in Appendix.

Estimate for energy-energy coupling by comparing to two isolated chains
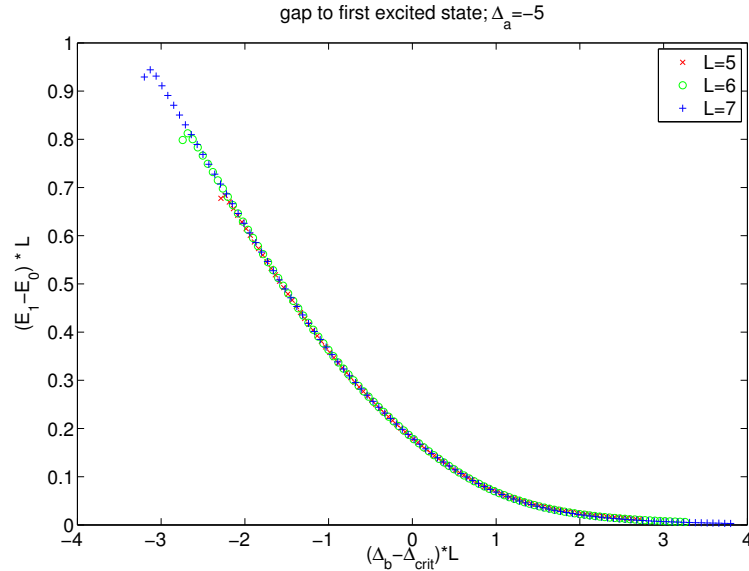
The analysis so far seems to be suggesting that the order parameters of the two chains are not coupled. Yet there is an effect of the interaction since the critical point is shifted compared to a single isolated chain. We can estimate the energy-energy coupling by comparing the ground state energy of two isolated chains with the one of our ladder, see Fig. 3.15.

Estimate of the order parameter coupling

Can we conclude that there is no coupling between the order parameters of the chains? The gap to the first three excited states seems to vanish exponentially, yet the following suggest that an order parameter coupling will appear for longer chains

1. There is a splitting between the first and the second excited state, $E_1 - E_2$. This splitting is very small, but it grows approximately linearly with system size, see Fig. 3.16. If these were truly four ground states, then the splitting should vanish exponentially.
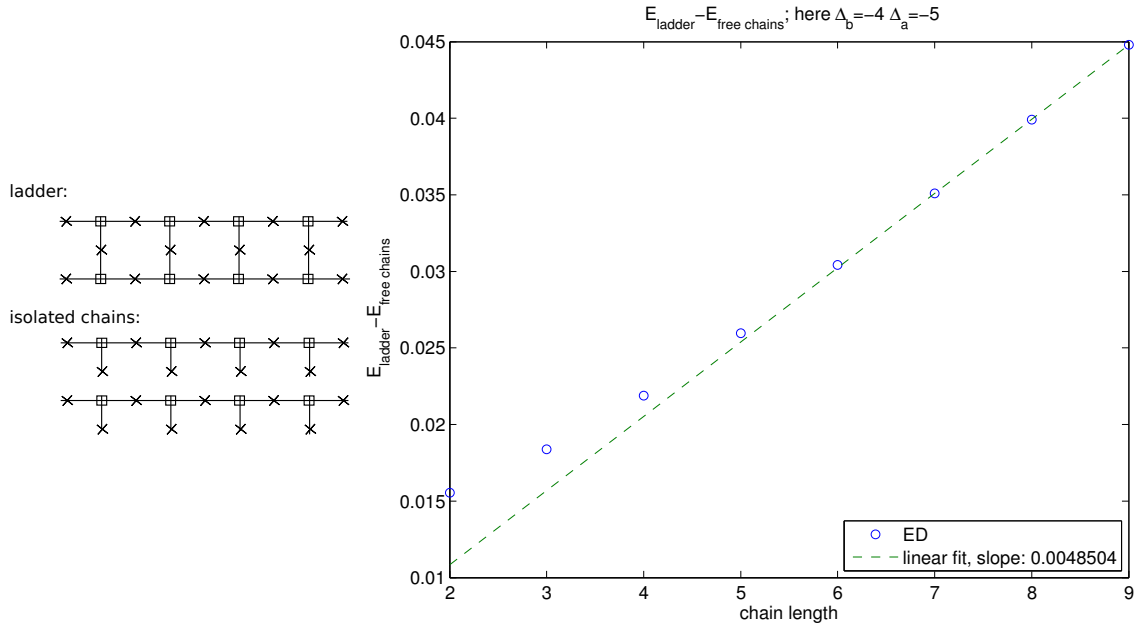
Figure 3.15: Comparing ground state energy of a ladder to the ground state energy of two isolated chains: energy cost for coupling.

2. We can show that there is no hidden symmetry forbidding order parameter coupling: if we fix the boundary conditions[11] to make the chains either aligned or antialigned, there is a difference in ground state energy of these two systems which grows linearly with system size, see Fig. 3.17. We can use the slope of this curve as an estimate for the coupling of the order parameters per unit cell.

3. We can apply a small bias field, which is larger than the splitting between the for lowest eigenstates to align the chains either ferromagnetically or antiferromagnetically. There is again a difference in ground state energy, which grows linearly with system size, see Fig. 3.18, and which again gives an estimate for the order parameter coupling.

The slopes of all three curves agree approximately, giving us a good estimate for the order parameter coupling of the chains. For the system sizes we studied so far, however, this

---

[11]We can view the segment under consideration as a part of a very long system, which is aligned either ferromagnetically or antiferromagnetically. The remainder of the long system provides the boundary conditions for the segment.
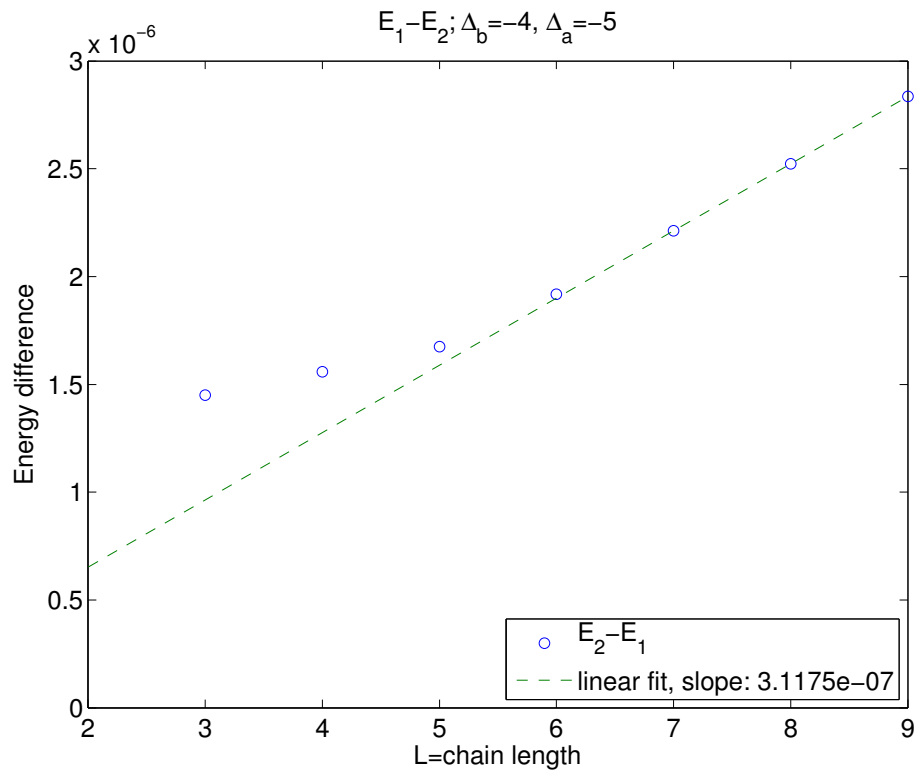
Figure 3.16: splitting between first and second excited state grows with system size. This suggests that there is indeed a coupling between the order parameters of these two chains, which is smaller than the finite size gap of each chain for our system sizes.
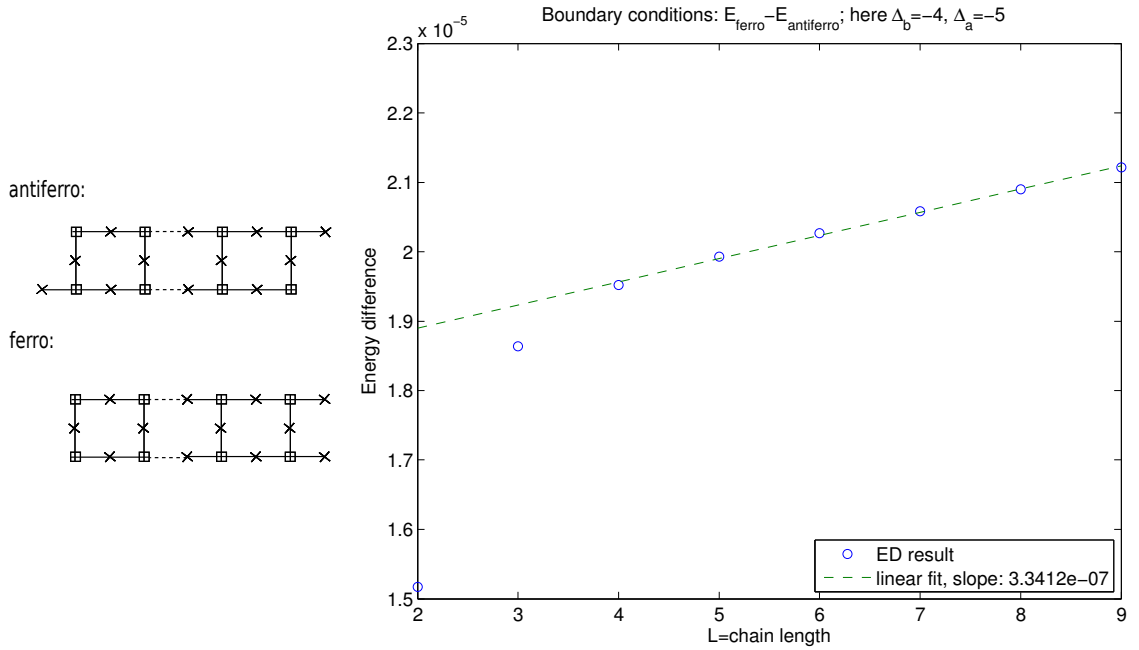
Figure 3.17: Fixing the boundary conditions so that the chains are either aligned or antialigned. The energy difference grows linearly with system size and antiferromagnetic boundary conditions are energetically favorable.

coupling is smaller than the effective tunneling element between the different ground states, i.e. smaller than the finite size gap. For larger chains this order parameter coupling will start to dominate over the tunneling, and then there will only be two ground state.

The coupling between two chains – if present – is *antiferromagnetic.* We can also understand this as from the difference of dimension of the Hibert space for ferromagnetic vs antiferromagnetic boundary conditions, see Tab. 3.1. The Hilbert space is larger for ferromagnetic boundary conditions, giving the system more states to fluctuate to. This reduces the energy.

3.4.3   Conclusions

At first sight this small system exact diagonalization study suggests that there should be no coupling between the order parameters: two coupled chains seem to have four ground states, just as two uncoupled chains. Having a closer look at the splitting between the different ground states, applying a bias field, and fixing the boundary conditions, however, we have been able to measure an antiferromagnetic coupling between two neighboring
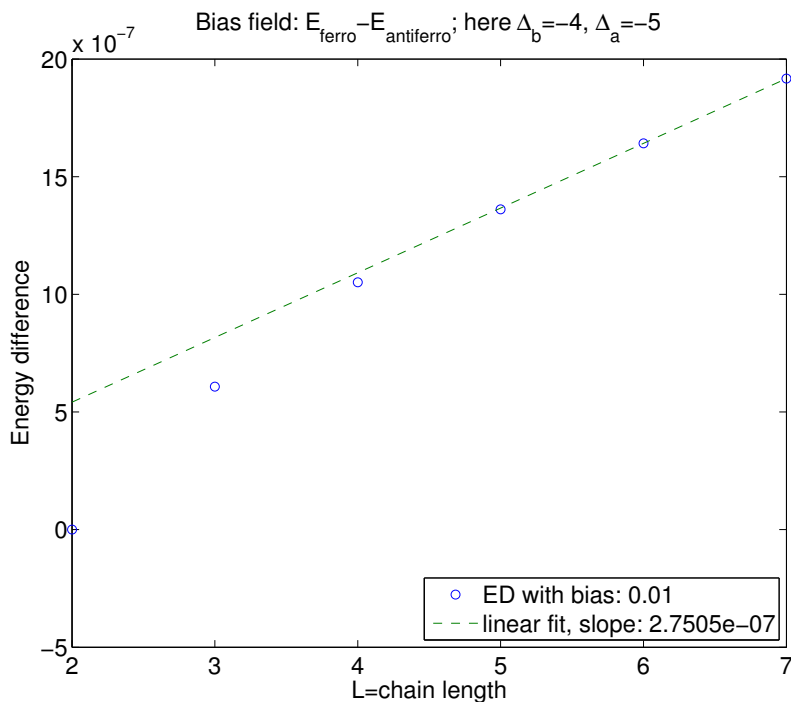
Figure 3.18: Difference in ground state energy for a system with ferromagnetic and antiferromagnetic bias field.

L	$\dim\left(H_{\mathrm{pcb}}\right)$	$\dim\left(H_{\mathrm{ferro}}\right)$	$\dim\left(H_{\mathrm{antiferro}}\right)$
2	32	13	14
3	158	65	73
4	828	341	389
5	4408	1815	2081
6	23564	9701	11140
7	126106	51913	59641
8	675076	277897	319309
9	3614144	1487763	1709535
10	19349432	7965181	9152606

Table 3.1: Dimension of Hilbert space for different boundary conditions: periodic, ferromagnetic, and antiferromagnetic, see text. Note that the dimension of Hilbert space is larger for antiferromangetic boundary conditions.

chains.

For the system sizes studied in exact diagonalization this coupling is smaller than the tunneling element between the two ground states. For systems sizes studies with QMC may become on the order of the finite size gap, but it is still orders of magnitude smaller than the temperature of the system. This is why we cannot see the coupling in QMC.

In conclusion we can say that the system seems to have strong finite size effects. It is very likely that the true phase diagram in the thermodynamic limit should have two regions with two-dimensional long range order. The phase transition would then be in the universality class of the 3D classical Ising model.

A quantum simulator of ultracold atoms would however be limited by the system size and see a one dimensional transition to ordered chains, just as we did in QMC.

量子相變

庚寅年冬月
吳冠彥

Figure 3.19: Quantum phase transition – an artist's view.

Chapter 4

Graphene-Like Coupled Spin Chains

We theoretically study graphene-like coupled spin 1/2 chains with a Heisenberg antiferromagnetic interaction. The chains are coupled in a way that would arise if they were taken off a honeycomb lattice at a zig-zag edge, see Fig. 4.1: along each chain only one out of two spins is coupled to the neighboring chain on the right, while the remaining spins are coupled to the left. Two chains thus form a ladder where every other rung is missing. Focussing on the case where the inter-chain coupling is stronger than the coupling along the chains, we use a bond-operator representation, where two spins are coupled, to obtain a mean-field theory. We also apply a unit cell mean field theory. We compare our results to Quantum Monte Carlo calculations and obtain good qualitative agreement. Such systems could be realized with ultracold atoms, an elongated trap, and optical lattices.

4.1 Introduction

A recent work [46] analyzed the possibility of reproducing graphene physics with cold atoms, and of extending it to the interacting regime by creating a two-dimensional honeycomb optical lattice and loading it with ultracold fermionic atoms, such as ^{6}Li, in two different internal states. The key advantage is that the relevant experimental parameters (*e.g.* configuration and strength of the optical potential, inter-atomic interaction strength tuned via Feshbach resonance) can be accurately controlled. In particular, it was shown that the three different hopping amplitudes between nearest-neighbor sites can be tunned
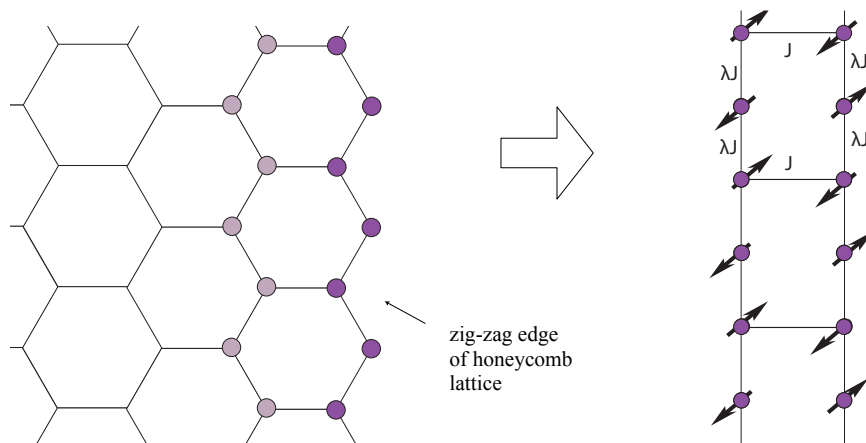
Figure 4.1: Motivation: spin chains coupled in a way that would arise if they were chopped off graphene at a zig-zag edge. Left: zig-zag edge of a honeycomb lattice. Right: two graphene-like coupled spin chains.

independently. When one of the hopping amplitude is much smaller than the two other, the situation of weakly-coupled zig-zag chains is obtained. In the regime of strong repulsion between the fermions, one is lead, at first order, to an effective Heisenberg anti-ferromagnetic interaction between spin 1/2. More precisely, in each chain, one out of two neighboring spins is coupled to a spin of the neighboring chain to the right, while the other one is coupled to the left. Adding a transverse confinement parallel to these weakly coupled chain results in the possibility of having only a few coupled chains, and, finally, for two chains, where only one out of two spins is coupled to the neighboring chain, a situation which differs from the standard spin ladders.

This Chapter is organized as follows. In Section 4.2 we describe the system and Hamiltonian. In Section 4.3 we consider the case of strong bonds and weak chains. We apply a bond operator approach and a unit-cell-mean-field approach, as well as Quantum Monte Carlo (QMC) calculations. In Section 4.4 we consider the opposite case, where the coupling along the chain is strong, while the inter-chain coupling is weak. We use we describe each chain by a Luttinger liquid and argue that, similar to the regular spin ladder any small coupling between the chains opens up a gap. Conclusions are presented in Section 4.5
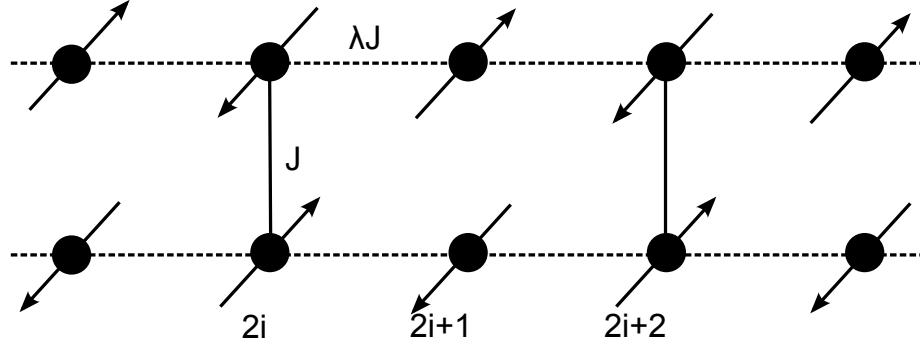
Figure 4.2: Model: two coupled spin chains with Heisenberg interaction. Only even rungs are present. Odd sites are not coupled to the neighboring chain.

4.2   Model and Hamiltonian

We study graphene-like coupled spin chains with Heisenberg antiferromagnetic interactions. For two spin chains, this corresponds to a Heisenberg spin ladder where every other rung is removed (i.e. all the odd rungs have been removed), see Fig. 4.2. The system is described by the following Hamiltonian $\hat{H} = \hat{H}_0 + \lambda \hat{H}_\lambda$

$$\hat{H}_0 \;\; = \;\; \sum_i^N \vec{S}_{l,(2i)} \cdot \vec{S}_{r,(2i)} \tag{4.1a}$$

$$\hat{H}_\lambda \;\; = \;\; \sum_{j,m=l,r}^{2N} \vec{S}_{m,(j)} \cdot \vec{S}_{m,(j+1)} \tag{4.1b}$$

Here the first index is a chain index, l or r, and the second index labels the spins along a chain.

In the following we will take two mean-field approaches and compare them to QMC calculations: a rung basis mean field and a unit cell mean field, keeping only the lowest energy eigenstates of each unit cell.

4.3   Weak chains and strong bonds: $J_\perp \gg J_\parallel$

4.3.1   Bond operator approach: Rung basis mean field

The bond operator approach introduced by S. Sachdev and R.N. Bhatt in Ref. [47], can be used to study spin ladders, as done by Gopalan, Rice, and Sigrist in Ref. [48]. Here we briefly review the bond operator approach and then apply it to our system. First, we describe each rung of a spin ladder (a regular ladder or our graphene-like ladder) in a singlet-triplet basis

$$|s\rangle \;=\; \frac{1}{\sqrt{2}}\left(|\uparrow\downarrow\rangle - |\downarrow\uparrow\rangle\right), \tag{4.2a}$$

$$|t_x\rangle \;=\; \frac{1}{\sqrt{2}}\left(|\uparrow\uparrow\rangle - |\downarrow\downarrow\rangle\right), \tag{4.2b}$$

$$|t_y\rangle \;=\; \frac{1}{\sqrt{2}}\left(|\uparrow\uparrow\rangle + |\downarrow\downarrow\rangle\right), \tag{4.2c}$$

$$|t_z\rangle \;=\; \frac{1}{\sqrt{2}}\left(|\uparrow\downarrow\rangle + |\downarrow\uparrow\rangle\right). \tag{4.2d}$$

We define operators $s^\dagger$ and $\hat{t}_\alpha^\dagger$ which create the state $|s\rangle$ and $|t_\alpha\rangle$ respectively. We now express the spin operators in this basis

$$S_{l,\alpha} \;=\; \frac{1}{2}\left(s^\dagger t_\alpha + \hat{t}_\alpha^\dagger s - i\epsilon_{\alpha,\beta,\gamma}\hat{t}_\beta^\dagger t_\gamma\right), \tag{4.3a}$$

$$S_{r,\alpha} \;=\; \frac{1}{2}\left(-s^\dagger t_\alpha - \hat{t}_\alpha^\dagger s - i\epsilon_{\alpha,\beta,\gamma}\hat{t}_\beta^\dagger t_\gamma\right). \tag{4.3b}$$

The Hamiltonian in this representation becomes

$$\hat{H}_0 \;=\; J\sum_i^N\left(-\frac{3}{4}\hat{s}_{2i}^\dagger s_{2i} + \frac{1}{4}\hat{t}_{2i,\alpha}^\dagger t_{2i,\alpha}\right) - \sum_j^{2N}\mu_j\left(\hat{s}_j^\dagger s_j + \hat{t}_{j\alpha}^\dagger t_{j,\alpha} - 1\right) \tag{4.4a}$$

and $H_\lambda = H_1 + H_2$ with

$$H_1 \;=\; \frac{J}{2}\sum_j^{2N}\left(\hat{t}_{j,\alpha}^\dagger t_{j+1,\alpha}\hat{s}_{j+1}^\dagger s_j + \hat{t}_{j,\alpha}^\dagger \hat{t}_{j1,\alpha}^\dagger s_j s_{j+1} + \text{H.c.}\right)$$

$$H_2 \;=\; -\frac{J}{2}\sum_j^{2N}\frac{1}{2}(1-\delta_{\alpha,\beta})\left(\hat{t}_{j,\alpha}^\dagger \hat{t}_{j+1,\alpha}^\dagger t_{j,\beta}t_{j+1,\beta} - \hat{t}_{j,\alpha}^\dagger \hat{t}_{j+1,\beta}^\dagger t_{j+1,\alpha}t_{j\beta} + \text{H.c.}\right)$$

where we have introduced the chemical potential to ensure the constraint $\hat{s}^\dagger s + \sum_\alpha \hat{t}_\alpha^\dagger t_\alpha = 1$ at each rung. In the following we neglect H_2, as contributions from this part are negligible with respect to those from H_1. The Hamiltionian $H_0 + \lambda H_1$ can be solved by mean field

decoupling. We assume that the singlets condense and take the mean field value $\bar{s}_e = \langle s_{2i} \rangle$ and $\bar{s}_o = \langle s_{2i+1} \rangle$. Here e stands for even, and o for odd, and we assume that also uncoupled rungs condense into singlets. This is justified for two reasons, as we will show: in Section 4.3.4 we present an effective model for the uncoupled spins only, and show that in second order in λ an effective antiferromagnetic coupling between these two spins is generated. Secondly, small system exact diagonalization and QMC calculations shows that the singlet occupation in the uncoupled rungs is indeed high. We take the chemical potentials to be equal for all coupled rungs $\mu_{2i} = \mu_e$ and also for all uncoupled rungs $\mu_{2i+1} = \mu_o$, due to translational invariance. We note that for the uncoupled rungs singlet and triplets are degenerate. The Hamiltonian in momentum space becomes

$$
\begin{aligned}
H_0 &= N\left(-\frac{3}{4}J\bar{s}_e^2 - \mu_o\bar{s}_0^2 - \mu_e\bar{s}_e^2 + \mu_0 + \mu_e\right) + \sum_k \hat{t}_{k,\alpha}^\dagger t_{k,\alpha}\left(\frac{J}{4} - \mu_e\right) - \hat{d}_{k,\alpha}^\dagger d_{k,\alpha}\mu_0 \\
H_1 &= J\bar{s}_o\bar{s}_e \sum_{k,\alpha} \cos(ka)\left(\hat{d}_{k,\alpha}^\dagger t_{k,\alpha} + \hat{t}_{k,\alpha}^\dagger d_{k,\alpha} + \hat{d}_{k,\alpha}^\dagger \hat{t}_{-k,\alpha}^\dagger + d_{k,\alpha}t_{-k,\alpha}\right),
\end{aligned} \tag{4.5}
$$

and it can be diagonalized by a Bogoliubov transform

$$
\begin{aligned}
H &= N\left(-\frac{3}{4}J\bar{s}_e^2 - \mu_o\bar{s}_0^2 - \mu_e\bar{s}_e^2 + \mu_0 + \mu_e\right) \\
&\quad - \frac{3N}{2}\left(\frac{J}{4} - \mu_e - \mu_o\right) \\
&\quad + \sum_k \left[\epsilon_1(k)\left(\hat{\gamma}_{\alpha k}^\dagger \hat{\gamma}_{\alpha k} + \frac{3}{2}\right) + \epsilon_2(k)\left(\hat{\zeta}_{\alpha k}^\dagger \hat{\zeta}_{\alpha k} + \frac{3}{2}\right)\right],
\end{aligned} \tag{4.6}
$$

with

$$
\epsilon_{1,2}(k) = \frac{\sqrt{A^2 + B^2 \mp \sqrt{(A^2 - B^2)^2 + 16ABC^2 \cos^2(ka)}}}{\sqrt{2}}, \tag{4.7}
$$

where we have parametrized

$$
\begin{aligned}
A &= \left(\frac{J}{4} - \mu_e\right), \\
B &= -\mu_0, \\
C &= \lambda J\bar{s}_o\bar{s}_e.
\end{aligned} \tag{4.8}
$$

Next we solve for the parameters μ_e, μ_o, s_e, and s_o by solving the four saddle point equations

$$
\langle\frac{\partial H}{\partial \mu_j}\rangle = 0, \qquad \langle\frac{\partial H}{\partial \bar{s}_j}\rangle = 0 \tag{4.9}
$$

here $j = e, o$. These saddle point equations are solved numerically and results are shown in Section 4.3.3.
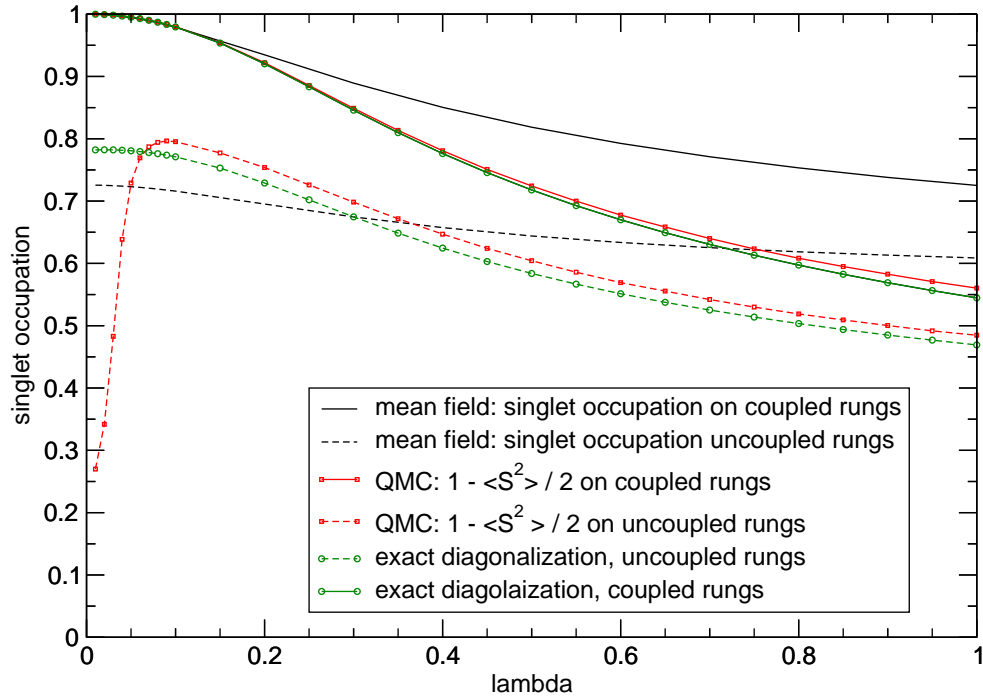
Figure 4.3: Singlet occupation on coupled and uncoupled rungs obtained from our meanfield approach, from QMC, and from exact diagonalization of a small system (16 spins).

Singlets on the uncoupled rungs

QMC and small system exact diagonalization (16 spins, periodic boundary conditions) show that the single occupation on the uncoupled rungs is indeed high, see figure Fig. 4.3 and 4.4. Comparing singlet occupation of the ground state and the first excited state suggest that low energy excitations break a singlet bond on the *uncoupled* rungs.

4.3.2   Unit cell mean field

Here we extend our approach by assuming a condensation of the ground state of each unit cell. We couple the four spins of each unit cell, see Fig. 4.5. This is similar to the plaquette basis approach used in Ref. [49], but here our unit cell has a λ-dependence, while in Ref. [49] it was taken constant. Diagonalizing the unit cell shows a low energy
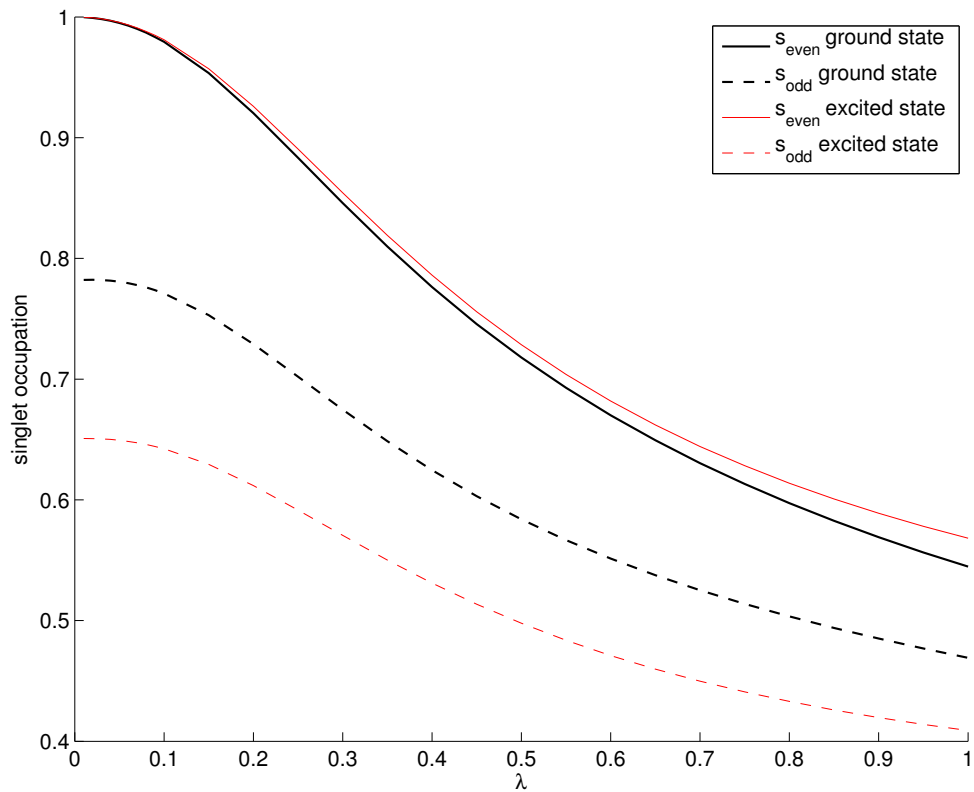
Figure 4.4: Singlet occupation on coupled and uncoupled rungs for the ground state (thick black line) and for the first excited states (thin red line), obtained from small system exact diaonalization (16 spins). The singlet occupation decreases for the first excited state, suggesting that low energy excitation come from breaking singlet bonds along those rungs.

Figure 4.5: unitcell and its energy eigenvalues. Note that for $\lambda \ll 1$ the singlet triplet gap is very small. On the other hand, as λ becomes larger, the distance between the third eigenvalue and the second one, becomes smaller than the singlet triplet gap.
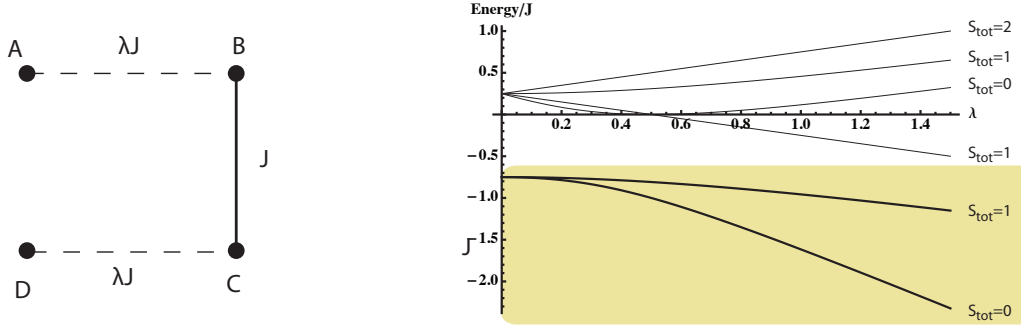
eigenvalue $\times 4$	S_{tot}	deg.	Eigenvector with $S_z = 0$
$-(1 + 2\lambda + 2\sqrt{1 - 2\lambda + 4\lambda^2})$	0	1	$a_s(\lvert 1 \rangle + \lvert 6 \rangle) + b_s(\lvert 2 \rangle + \lvert 5 \rangle) + c_s(\lvert 3 \rangle + \lvert 4 \rangle)$
$-(1 + 2\sqrt{1 + \lambda^2})$	1	3	$-\cos\theta_t(\lvert 1 \rangle - \lvert 6 \rangle) + \sin\theta_t(\lvert 2 \rangle - \lvert 5 \rangle)$
$1 - 2\lambda$	1	3	$\frac{1}{\sqrt{2}}(-\lvert 3 \rangle + \lvert 4 \rangle)$
$-1 - 2\lambda + 2\sqrt{1 - 2\lambda + 4\lambda^2}$	0	1	$a_4(\lvert 1 \rangle + \lvert 6 \rangle) + b_4(\lvert 2 \rangle + \lvert 5 \rangle) + c_4(\lvert 3 \rangle + \lvert 4 \rangle)$
$-1 + 2\sqrt{1 + \lambda^2}$	1	3	$\sin\theta_t(\lvert 1 \rangle - \lvert 6 \rangle) + \cos\theta_t(\lvert 2 \rangle - \lvert 5 \rangle)$
$1 + 2\lambda$	2	5	$\frac{1}{\sqrt{6}}(\lvert 1 \rangle + \lvert 2 \rangle + \lvert 3 \rangle + \lvert 4 \rangle + \lvert 5 \rangle + \lvert 6 \rangle)$

Table 4.1: Eigenstates of a unit cell: eigenvalue, total spin, and degeneracy. For the last column we used $\lvert 1 \rangle = \lvert \uparrow\uparrow\downarrow\downarrow \rangle$, $\lvert 2 \rangle = \lvert \uparrow\downarrow\uparrow\downarrow \rangle$, $\lvert 3 \rangle = \lvert \uparrow\downarrow\downarrow\uparrow \rangle$, $\lvert 4 \rangle = \lvert \downarrow\uparrow\uparrow\downarrow \rangle$, $\lvert 5 \rangle = \lvert \downarrow\uparrow\downarrow\uparrow \rangle$, $\lvert 6 \rangle = \lvert \downarrow\downarrow\uparrow\uparrow \rangle$.

subspace consisting of one ground state with total spin zero, next three degenerate states with $S_{\text{tot}} = 1$. For simplicity we first only keep this low energy subspace and disregard the states with higher energy. Table 4.1 shows eigenstates, their total spin, degeneracy and eigenvectors.

The unperturbed gap between the ground state energy ϵ_s and the energy of the first excitation ϵ_t is given by

$$\Delta_0 := \epsilon_t - \epsilon_s = \frac{1}{2}\left(\lambda - \sqrt{1 + \lambda^2} + \sqrt{1 - 2\lambda + 4\lambda^2}\right).$$

In this section we define the states $\lvert s \rangle$ as the ground state of a unit cell and $\lvert t_\alpha \rangle$ are the three degenerate first excited states. As in the previous section we define corresponding bosonic
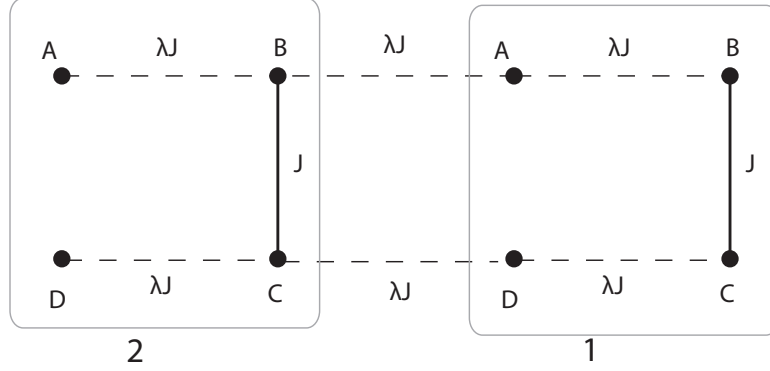
Figure 4.6: Labeling of the spins withing a unitcell.

annihilation and creation operators s, $s^\dagger$, t_α, $t_\alpha^\dagger$, and express our Hamiltonian Eq. (4.1) in this basis. We divide our Hamiltonian in two parts $H = H_{\text{unitcell}} + \frac{1}{2}\sum_{i\neq j} H_{i,j}^{\text{link}}$, the first part is already diagonalized by the choice of basis, and

$$H_{1,2}^{\text{link}} = \lambda J \left(\vec{S}_1^A \cdot \vec{S}_2^B + \vec{S}_1^D \cdot \vec{S}_2^C \right). \tag{4.10}$$

Here we labeled the spins in each unit cell A, B, C, D, see figure Fig. 4.6. Neglecting again the triplet-triplet terms, we find the following expression

$$H^{\text{link}} = \lambda J \alpha_t \sum_j (s_j^\dagger s_{j+1}^\dagger t_{j\alpha} t_{j+1\alpha} + s_j^\dagger s_{j+1} t_{j\alpha} t_{j+1\alpha}^\dagger + \text{H.c.}) \tag{4.11}$$

where $\alpha_t = 2(a_s^2 a_t^2 - b_s^2 b_t^2)$ (the coefficients are defined in Table 4.1) is given as a function of λ by

$$\alpha_t = -\lambda \frac{1 - \lambda + 3\sqrt{1 + \lambda^2} + 2\sqrt{1 - 2\lambda + 4\lambda^2}}{12\sqrt{1 + \lambda^2}\sqrt{1 - 2\lambda + 4\lambda^2}}. \tag{4.12}$$

Assuming condensation of the lowest energy state, we obtain a quadratic Hamiltonian in momentum space

$$H_{MF} = N\left(\epsilon_s \bar{s}^2 - \mu \bar{s}^2 + \mu\right) + \sum_{k,\alpha} \Lambda_k t_{k,\alpha}^\dagger t_{k,\alpha} + \Delta_k \left(\hat{t}_{k,\alpha}^\dagger \hat{t}_{k,-\alpha}^\dagger + t_{k,\alpha} t_{k,-\alpha} \right) \tag{4.13}$$

with

$$\Lambda_k = \epsilon_t - \mu + 2\lambda\alpha_M \bar{s}^2 \cos(kb), \tag{4.14}$$

$$\Delta_k = \lambda\alpha_M \bar{s}^2 \cos(kb). \tag{4.15}$$

a Bogoliobov transform yields

$$
\begin{aligned}
H_{MF} &= N\left(\epsilon_s \bar{s}^2 - \mu \bar{s}^2 + \mu\right) - \frac{3N}{2}(\epsilon_t - \mu) \\
&\quad + \frac{3}{2}\sum_k \omega_k + \sum_{k\alpha} \omega_k \gamma^\dagger_{k\alpha}\gamma_{k\alpha}
\end{aligned}
\tag{4.16}
$$

$$
\omega_k = \sqrt{\Lambda_k^2 - (2\Delta_k)^2}
\tag{4.17}
$$

We again need to solve the saddle point equations $\langle \frac{\partial H_{\mathrm{MF}}}{\partial \mu} \rangle_0 = 0$, $\langle \frac{\partial H_{\mathrm{MF}}}{\partial \bar{s}} \rangle_0 = 0$, which take the following form

$$
\begin{aligned}
\left(-\bar{s}^2 + \frac{5}{2}\right) &= \frac{3}{2}\frac{1}{\pi}\left(\frac{1}{\sqrt{1+d}}K\left(D^2\right) + \sqrt{1+d}E\left(D^2\right)\right), \\
(\mu - \epsilon_s) &= 6\frac{\lambda|\alpha|}{d\pi}\left(\sqrt{1+d}E\left(D^2\right) - \frac{1}{\sqrt{1+d}}K\left(D^2\right)\right),
\end{aligned}
$$

here K and E denote the elliptical integrals[1] of the first and second kind [50]. The ground state energy is then given by

$$
\frac{E_G}{NJ} = (\epsilon_s \bar{s}^2 - \mu\bar{s}^2 + \mu) - \frac{3}{2}(\epsilon_t - \mu) + \frac{3}{\pi}(\epsilon_t - \mu)\sqrt{1-d}E\left(D^2\right)
\tag{4.18}
$$

and the energy gap by

$$
\Delta = \sqrt{(\epsilon_t - \mu)^2 - 4(\epsilon_t - \mu)^2\lambda|\alpha|\bar{s}^2}.
\tag{4.19}
$$

We also included the next triplet band, however, this brings only very slight improvement, see Fig. 4.7

4.3.3   Results

In this section we summarize our results of the mean-field and QMC calculations. The QMC calculations have been performed using the SSE algorithm with directed loop from the ALPS project [51, 52]. The results presented in this paper have been obtained for chain length $L = 60$, corresponding to 240 spins. The typical number of sweeps, after thermalization, is 600 000. The energy gap Δ is extracted from the spin susceptibility $\chi(\beta)$ by fitting with the expression $e^{-\beta\Delta}/\sqrt{\beta}$ as a function of the inverse temperature β. For small value of λ, β values as large as 1000 has been used. We have checked that the results remains the same when increasing the chain length.

---

[1] we used the following definition of the elliptic integrals, which is the same as Ref. [50]: $\int_0^{\pi/2}\frac{d\theta}{\sqrt{1-k^2\sin^2\theta}} = K(k^2)$, and $\int_0^{\pi/2}\sqrt{1-k^2\sin^2\theta}d\theta = E(k^2)$.
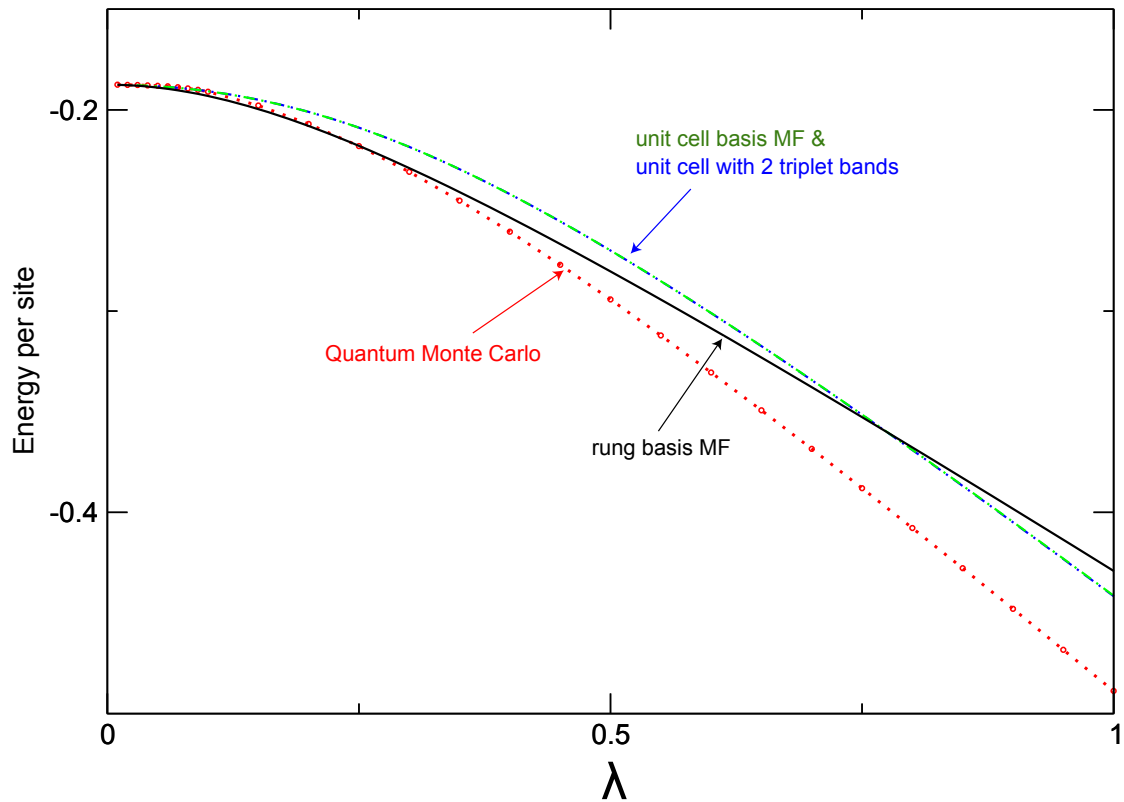
Figure 4.7: Ground state energy: QMC and mean field calculation

Ground state energy

Fig. 4.7 shows the ground state energy of the graphene-like coupled ladder. For small λ, the rung basis MF agrees better with QMC results. This is probably because there it not much of a difference between the ground state of the unit cell and the bonds on each site for that regime, but the rung basis keeps the entire Hilbert space. Then, as λ gets larger, the unit cell basis works better. This might be because then the true ground state becomes more and more different from the one of the rung basis; and the unit cell basis incorporates more of the short scale physics, so it describes the system more accurately.

Energy gap

Fig. 4.8 shows the energy gap as a function of λ, which shows a good qualitative agreement. Surprisingly, the unit cell basis mean-field is closer to the QMC than the bond

Excitation gap vs lambda for graphe-like coupled chain
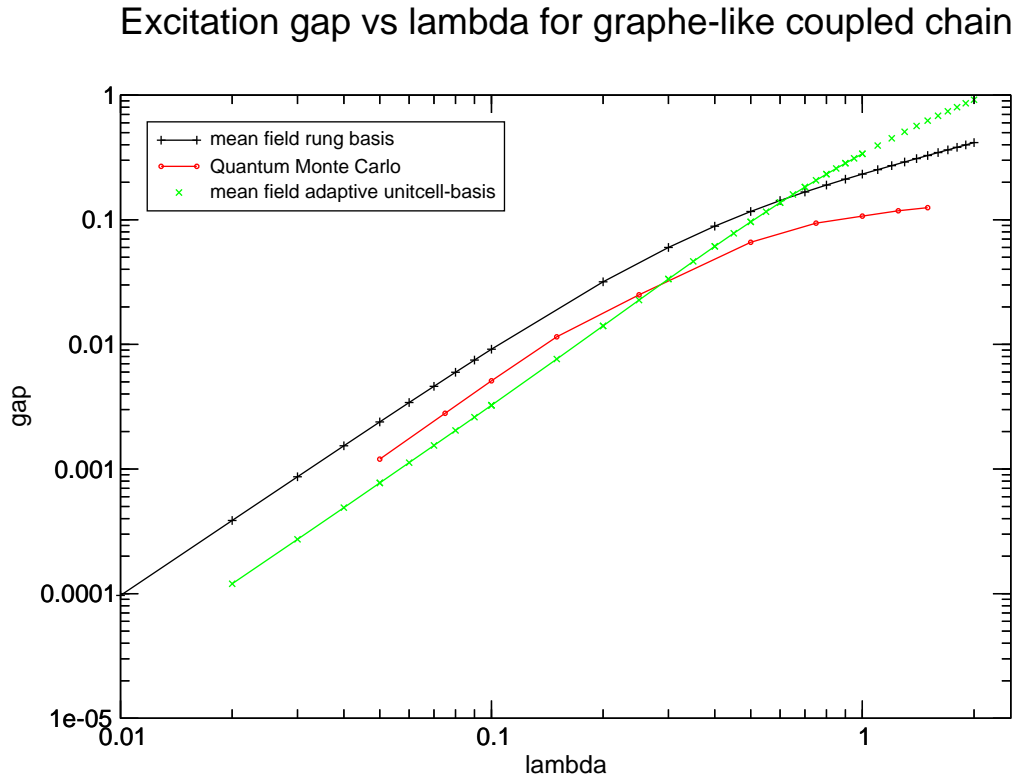
Figure 4.8: Results for the energy gap from mean-field and QMC calculations as a function of λ on a log-log scale. All cases (bond operator mean-field, unitcell meanfield and QMC) show a quadratic dependence of the energy gap on λ for small values of λ, and good qualitative agreement in this region.

operator MF for small λ. For larger λ unit cell mean field overestimates the gap. This could be related to the fact that the unperturbed gap ($\Delta_0 = \epsilon_t - \epsilon_s$) of this model is growing with lambda, while the unperturbed gap for the bond operator approach does not depend on λ.

4.3.4   Limit $J_\parallel/J_\perp \to 0$: effective model

In the limit $\lambda \ll 1$, where the chains are very weak, we can derive an effective Hamiltonian for the uncoupled spins only. We assume that all the coupled spins are locked into singlets, and integrate them out. The effective Hamiltonian has both antiferromagnetic and ferromagnetic coupling, in fact, the coupling along the chains changes sign and becomes
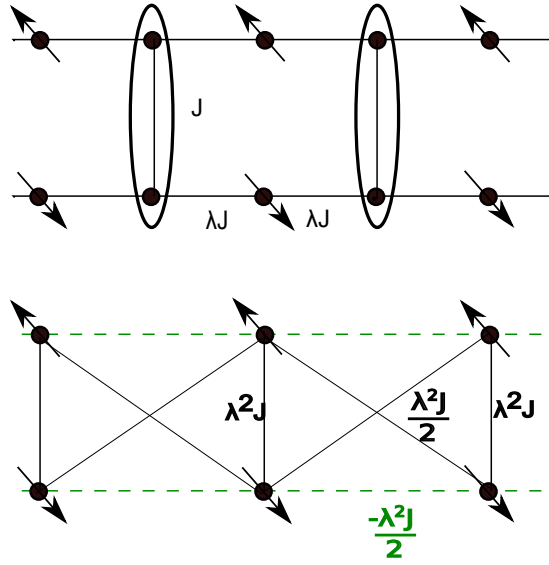
Figure 4.9: Effective model for the uncoupled chains, to second order in λ. Dashed green lines represent *ferro*magnetic coupling, while black lines represent antiferromagnetic coupling.

ferromagnetic, see Fig. 4.9,

$$
\begin{aligned}
\hat{H}_{\text{effective}} \ = \ & -\frac{\lambda^2 J}{2} \sum_{j,m=l,r} \vec{S}_{m,2j-1} \cdot \vec{S}_{m,2j-1} \\
& +\lambda^2 J \sum_{j=0}^{\infty} \vec{S}_{l,2j+1} \cdot \vec{S}_{r,2j+1} \\
& +\frac{\lambda^2 J}{2} \sum_{j=}^{\infty} \vec{S}_{l,2j-1} \cdot \vec{S}_{r,2j+1} + \vec{S}_{r,2j-1} \cdot \vec{S}_{r,2j+1}
\end{aligned}
\tag{4.20}
$$

indeed, an effective coupling along the initially uncoupled bonds appears to second order in λ. Note that we can 'untwist' this chains, redefining each new chain to be following the crossed antiferromagnetic links. This yields an antiferromagnetic spin ladder, with an additional ferromagnetic crossed interaction. Applying the bond operator approach to this model gives precisely the same mean-field equations as for a regular spin ladder [48]. This effective model also explains the quadratic dependence of the gap on λ for small λ.

4.4   Weakly coupled spin chains: $J_\perp/J_\parallel \to 0$

In this section we briefly consider the opposite limit, $\lambda \to \infty$: strong coupling along the chains, and week links. We describe each of the chains by a Luttinger Liquid Hamiltonian [53]

$$H_{LL} = \frac{\hbar}{2\pi} \int dx \left[\frac{uK}{\hbar^2} \left(\pi \hat{\Pi}(x) \right)^2 + \frac{u}{K} \left(\nabla\phi(x) \right)^2 \right] \tag{4.21}$$

there is an additional sine-Gordon term, which is not relevant at the Heisenberg point, and the single Heisenberg antiferromagnetic spin $\frac{1}{2}$ chain is in a gapless Luttinger liquid phase [53]. At the Heisenberg point we have $K = \frac{1}{2}$, and $\phi(x)$ and $\Pi(x)$ are the conjugate Luttinger fields, fulfilling canonic commutations relations. Expression for the original spin operators in terms of the Luttinger fields of a single chain are given by [53]

$$S_z(x) \;\; = \;\; -\frac{1}{\pi}\nabla\phi(x) + \frac{(-1)^x}{\pi\alpha}\cos(2\phi(x)) \tag{4.22}$$

$$S^+(x) \;\; = \;\; \frac{e^{-i\theta(x)}}{\sqrt{2\pi\alpha}} \left[(-1)^x + \cos(2\phi(x)) \right] \tag{4.23}$$

our graphene-like ladder is described by the following Hamiltonian

$$H = H_1^0 + H_2^0 + J_\perp \sum_j \vec{S}_{2j,1} \cdot \vec{S}_{2j,2} \tag{4.24}$$

where H_1^0 (H_2^0) is the Luttinger liquid Hamiltonian for the left (right) chain. We can rewrite this in a more convenient form

$$H = H_1^0 + H_2^0 + J_\perp \frac{1}{2} \sum_j \vec{S}_{j,1} \cdot \vec{S}_{j,2} + J_\perp \frac{1}{2} \sum_j (-1)^j \vec{S}_{j,1} \cdot \vec{S}_{j,2}. \tag{4.25}$$

The first sum corresponds to the rungs of a regular spin ladder (each site of the chain is coupled to a site of the other chain) with half the interaction strength. The second sum is additionally present in our system, canceling all the odd rungs. We proceed to showing that the most relevant terms in this Hamiltonian are the ones coming from the first sum. It is well know that these terms open up a gap for any small coupling $J_\perp$. Writing out the interaction Hamiltonian (first and second sum) yields:

$$\hat{H}_{\text{int}} = H_{\text{int,reg}} + H_{\text{int,stag}} \tag{4.26}$$

where $H_{\text{int,reg}}$ contains all the terms that are present in a regular spin ladder,

$$
\begin{aligned}
H_{\text{int,reg}} \;=\; & \int \Bigg[\frac{g_1}{(2\pi a)^2}\cos(\sqrt{2}\theta_a) + \frac{2g_2}{(2\pi a)^2}\cos(\sqrt{8}\phi_a) + \frac{2g_3}{(2\pi a)^2}\cos(\sqrt{8}\phi_s) \\
& + J_\perp^z a\,\frac{(\nabla\phi_s)^2 - (\nabla\phi_a)^2}{\pi^2} \\
& + \frac{J_\perp}{4\pi a^2}\cos(\sqrt{2}\theta_a)\left[\cos(\sqrt{8}\phi_a) + \cos(\sqrt{8}\phi_s)\right] \Bigg] dx
\end{aligned} \tag{4.27}
$$

where the couplings are $g_1 = \pi j_\perp^{x,y}a$ and $g_2 = g_3 = J_\perp^z a$. Our additional staggered part is

$$
\begin{aligned}
H_{\text{int,staggered}} \;=\; & \int dx\,\frac{\sqrt{2}J_\perp^z}{\pi^2 a^2}\Big[\ (\nabla\phi_s)\cos(\sqrt{2}\phi_s)\cos(\sqrt{2}\phi_s)\cos(\sqrt{2}\phi_a) \\
& \qquad\qquad\quad + (\nabla\phi_s)\cos(\sqrt{2}\phi_s)\cos(\sqrt{2}\phi_s)\cos(\sqrt{2}\phi_a)\Big] \\
& + \int dx\,\frac{2J_\perp^{xy}}{\pi a^2}\ \ \cos(\sqrt{2}\theta_a)\cos(\sqrt{2}\phi_s)\cos(\sqrt{2}\phi_a).
\end{aligned} \tag{4.28}
$$

To get an idea on how the system behaves, we compute the scaling dimensions for each of the terms. We find that the most relevant perturbations are the ones of $H_{\text{int,reg}}$, which open up a gap. There are also terms in $H_{\text{int,staggered}}$ which are relevant, but these are less relevant. This suggests that the graphene-like coupled spin ladder behaves qualitatively like the regular ladder, for all $\lambda \neq 0$. This approach being a low energy effective theory will not gives us values for the ground state energy or the gap.

Let $\hat{O}$ be some operator, and $\dim[\hat{O}] = \Delta$ is called the operator's scaling dimension as the correlations of that operator decay as $\langle\hat{O}(x)\hat{O}(0)\rangle \propto \frac{1}{x^{2\Delta}}$. If the operator now enters the Hamiltonian with a coupling, $g\hat{O}$, and the scaling dimension of the coupling constant is given by $\dim[g] = 2 - \Delta$. Its flow equations, to first order in l is $\frac{dg}{dl} = (2 - \Delta)g$, where the system is rescaled as $x \to xe^{-l}$, see [43]. The scaling dimension of position and momentum are thus given by $\dim[x] = -1$, $\dim[k] = 1$, and $\dim[\nabla] = 1$. The fields ϕ and θ themselves do not flow, $\dim[\phi] = \dim[\theta] = 0$. The operator is a relevant perturbation if $\Delta < 2$, it is marginal if $\Delta = 2$ and irrelevant if $\Delta > 2$.

In this notation, operator $\cos(A\phi)$, where A is some constant, has scaling dimension $\dim[\cos(A\phi)] = KA^2/8$, as

$$
\langle\cos(A\phi(x))\cos(A\phi(0))\rangle \propto e^{-\frac{A^2}{2}\langle(\phi(x)-\phi(0))^2\rangle} \propto \left(\frac{a}{|x|}\right)^{KA^2/2},
$$

and similarly $\dim[\cos(A\theta)] = \frac{A^2}{4K}$. To find the scaling dimensions of terms containing derivatives of the fields, we rewrite the correlations in the following form. For example if

Operator $\hat{O}$	$\Delta = \dim[\hat{O}]$	Δ for $K_a = K_s = \frac{1}{2}$
$\cos(\sqrt{8}\phi_a)$	$2K_a$	1
$\cos(\sqrt{8}\phi_s)$	$2K_s$	1
$\cos(\sqrt{2}\theta_a)$	$\frac{1}{2K_a}$	1
$(\nabla\phi_s)\cos(\sqrt{2}\phi_s)\cos(\sqrt{2}\phi_a)$	$\frac{K_a}{2} + \frac{K_s}{2} + 1$	1.5
$(\nabla\phi_s)\sin(\sqrt{2}\phi_s)\sin(\sqrt{2}\phi_a)$	$\frac{K_a}{2} + \frac{K_s}{2} + 1$	1.5
$\cos(\sqrt{2}\theta_a)\cos(\sqrt{2}\phi_s)\cos(\sqrt{2}\phi_a)$	$\frac{1}{2K_a} + \frac{K_s}{2} + \frac{K_a}{2}$	1.5
$\cos(\sqrt{2}\theta_a)\cos(\sqrt{8}\phi_s)$	$2K_s + \frac{1}{2K_a}$	2
$\cos(\sqrt{2}\theta_a)\cos(\sqrt{8}\phi_a)$	$2K_a + \frac{1}{2K_a}$	2

Table 4.2: Scaling dimensions of the operators in our Hamiltonian. The most relevant operators are the ones that also apper on the regular spin ladder.

the following term (coming from $\cos(\sqrt{2}\phi)$) can be rewritten as

$$
\begin{aligned}
\langle\nabla\phi(x)e^{i\sqrt{2}\phi(x)}\nabla\phi(x')e^{i\sqrt{2}\phi(x')}\rangle &= \frac{1}{2}\frac{d}{dx}\frac{d}{dx'}\langle e^{i\sqrt{2}\phi(x)}e^{i\sqrt{2}\phi(x')}\rangle = \frac{1}{2}\frac{d}{dx}\frac{d}{dx'}e^{-\langle(\phi(x)-\phi(x'))^2\rangle} \\
&= \frac{d}{dx}\frac{d}{dx'}\left(\frac{a}{|x-x'|}\right)^K \propto \frac{-K(K+1)}{|x-x'|^{K+2}},
\end{aligned}
$$

and we can read off its scaling dimension. Table 4.2 shows the scaling dimensions of various terms appearing in our Hamiltonian. This suggest that two graphene-like coupled spin chains behave qualitatively similar to a regular spin ladder, and that the system is gapped for all values of λ, with the exception of the special points: $\lambda = 0$ (no chains) and $\lambda \to \infty$ (no rungs).

We see that the most relevant terms for the graphene-like coupled spin chains are the same as the most relevant terms of the regular spin ladder: these terms open up a gap to all excitations. This strongly suggests that this system behaves qualitatively similar to the regular spin ladder.

4.5   Conclusion and Outlook

We have used various methods to study graphene-like coupled spin chains: a bond-operator mean-field approach, unit cell mean-field, and Quantum Monte Carlo, as well as scaling arguments applied to two coupled Luttinger liquids. Our results suggest that two graphene-like coupled spin chains behave qualitatively similar to a regular spin ladder, and that all excitations are gapped for all finite, non-zero values of λ. There are many possible

extensions to this work. First of all, one could consider the situations where more and more chains are added, studying this way the 1D-2D transition towards the graphene situation. In particular, since there is numerical evidence for the existence of a spin liquid phase in the fermi-hubbard model on the honeycomb lattice [54], it would be interesting to see how this phase emerges from the quasi-1D situation. From that point of view, it would be interesting to extend the present study to either the t-J model or the fermi-hubbard model on these graphene-like coupled chains.

Chapter 5

Interference of Parametrically-Driven 1d Quantum Gases

We theoretically analyze interference patterns of parametrically driven one dimensional ultracold atomic gases. By modulating the interaction strength periodically in time, we propose to excite collective modes in a pair of independent one-dimensional gases at energies corresponding to the drive frequency. The excited collective modes lead to spatial oscillations in the correlations of the interference pattern, which can be analyzed to obtain the sound velocity of the collective modes. We discuss both bosonic and fermionic systems, and how such experiments could be used to probe spin charge separation.

5.1 Introduction

One-dimensional systems show many interesting properties like charge fractionalization and separation of charge excitations from spin excitations. There is experimental evidence for these properties in various systems [55, 56, 57, 58, 59, 60, 61]. Recent progress in trapping and cooling of cold atoms, has made it possible to study one-dimensional systems and their properties in both fermions and bosons [62, 63, 64, 12, 65, 66]. One of the primary tools in measuring properties of cold atoms are interference experiments.

Surprisingly, it has been shown that interfering two independently created Bose
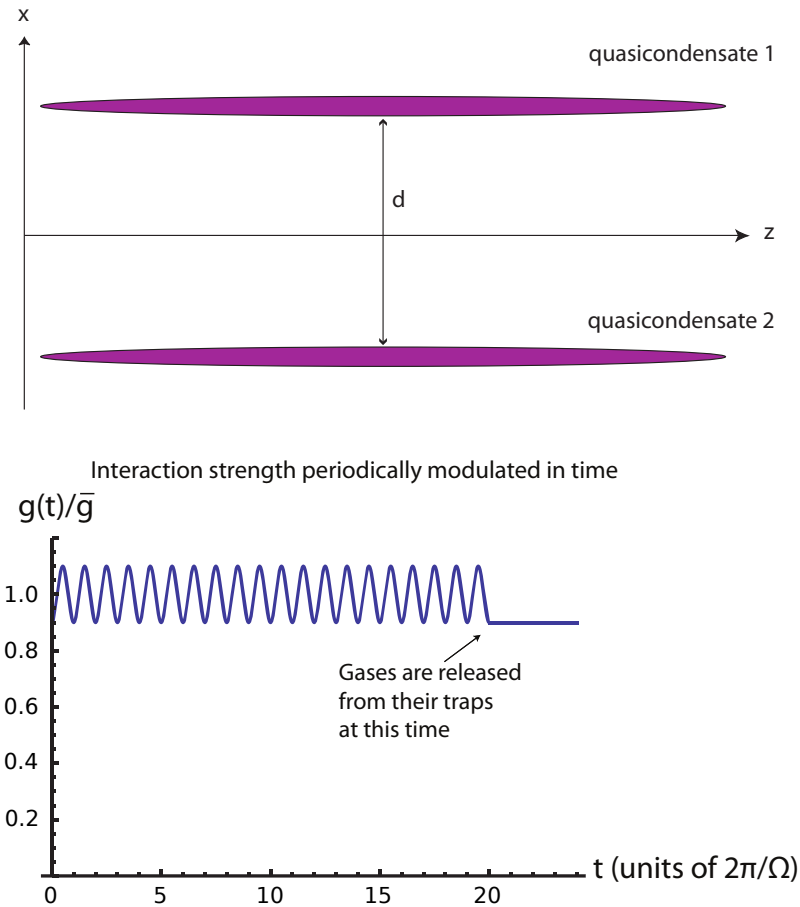
Figure 5.1: Proposed setup: two independently created one-dimensional systems of ultracold atoms are first parametrically driven by changing the inter-atomic interaction strength periodically in time (e.g. by changing the transverse trapping frequency), at time T the driving stops and the systems are released from their traps and allowed to overlap. An absorption image is taken, showing wiggely fringes along the z axis. These fringes contain information about the two-point correlation function within each gas (before expansion) and can be analyzed to obtain the sound velocity of the collective modes.

Einstein condensates (e.g. by releasing the confining potential and letting them expand and overlap) gives rise to spatially periodic patterns in each experimental shot. As there is no well defined phase between the two condensates, the maxima and minima of the pattern are at different positions in each shot, so that the average over many shots, corresponding to a quantum-mechanical ensemble average $\langle \hat{\rho}(\vec{r}) \rangle = 0$, contains no interference fringes. The key to this effect is that we can decompose the state of the two condensates, each containing a definite number of particles, into a superposition of states of well defined relative phases. Measuring the interference pattern collapses the wavefunction of the combined system to a state with definite phase, and thus produces a periodic pattern. To theoretically study this effect, we need to study the density-density correlation function $\langle \hat{\rho}(\vec{r}_1) \hat{\rho}(\vec{r}_2) \rangle$ instead of the average density, since the quantum mechanical average of the density formed in interference experiments samples all possible relative phases and thus hides the interference pattern. The above arguments hold true even for an interfering pair of one-dimensional systems, with one important modification: as there is no long range order, the maxima formed in the interference pattern are wavy lines instead of straight lines. This waviness contains information about the correlation function within each 1d system [67, 68].

Here we propose an experimental approach to create and directly probe excitations in one-dimensional ultracold atom systems of both bosons and fermions. In particular, for systems composed of mixtures of two species, our method allows us to see separation to spin and charge modes. Our approach is to start with a pair of one-dimensional systems, parametrically drive excitations by temporally periodic modulation of the particle particle interaction strength, and finally analyze the interference pattern, see Fig. 5.1 Experiments involving parametric driving to create excitations in one-dimensional fermionic gases have recently been proposed in Refs [69, 70]. In this work, in addition to fermionic gases, we study also bosonic gases, which are of experimental interest.

In interference experiments with one-dimensional systems of cold atoms, the gases are released from their traps and allowed to expand. We label the longitudinal direction as the z the axis, and the two systems lie in the x-z plane, see Fig. 5.1. Due to the strong transverse confinement, when released from their traps, the atoms expand mainly in the transverse directions. Therefore, we shall neglect the motion of atoms in the longitudinal direction during the expansion. Once the gases have expanded to a size much larger than the initial distance d between the two systems, an absorption image is taken. We neglect the slowly varying envelope and the expectation value of the density in case of independently

created quasicondensates is a constant, $\langle \hat{\rho}(x,z) \rangle = \rho_{\text{tof}} \rho_0$, where ρ_0 is the line density of each quasicondensate. The density-density correlations function, however, contains an oscillating term at wave vector $Q = \frac{dm}{\hbar t}$, m is the particle mass, t the time of expansion. See Section 5.6 for a detailed derivation of the following equation:

$$\langle \hat{\rho}(r_1)\hat{\rho}(r_2) \rangle \propto \left(\rho_0^2 \pm \left| \langle \hat{\psi}^\dagger(z_1)\hat{\psi}(z_2) \rangle \right|^2 \cos(\Delta x Q) \right), \tag{5.1}$$

where r_i stands for (x_i, z_i), $\Delta x = x_1 - x_2$, the upper (lower) sign applies to bosons (fermions). $\hat{\psi}(z)$ denotes the particle annihilation operator in either of the equivalent initial 1d systems. To derive Eq. (5.1) we have neglected the motion of atoms along the longitudinal direction during expansion; assumed that the two systems are initially identical and independent; assumed large expansion times (e.g. the size of the overlapping clouds is much larger than their initial separation d). See appendix 5.6; Ref [68] contains a more detailed discussion.

Typically, experimental data is analyzed by looking at the integrated density-density correlation function [67, 71],

$$\int_0^L dz_1 dz_2 \langle \hat{\rho}(x,z_1)\hat{\rho}(0,z_2) \rangle \propto \rho_0^2 L^2 + \langle |A_L|^2 \rangle \cos(Qx),$$

where L is the length of the integration, and the interference amplitude A_L is given by $\langle |A_L|^2 \rangle = L \int_0^L dz \left| \langle \hat{\psi}^\dagger(z)\hat{\psi}(0) \rangle \right|^2$. One can now define the interference contrast $C_L = |A_L|/\rho_0 L$, which decays as the integration length L is increased, encoding the decay of the correlation functions in the one-dimensional systems [67].

Our approach is to study the interference pattern of one-dimensional gases that have been parametrically driven out of equilibrium. The driving is done by a temporally periodic change of interaction strength for a certain time T before the gases are released from their traps. To extract information from the interference pattern, we suggest to take the Fourier transform along the z-axis, and then study correlations for that Fourier transform. We define

$$\hat{\tilde{\rho}}(x,q) = \int_0^L e^{iqz} \hat{\rho}(x,z) dz \tag{5.2}$$

and then consider the quantity $\langle \hat{\tilde{\rho}}(x,q)\hat{\tilde{\rho}}(0,-q) \rangle$ which is given by

$$\langle \hat{\tilde{\rho}}(x,q)\hat{\tilde{\rho}}(0,-q) \rangle \quad \propto \quad \cos(xQ) L \int_0^L dz \cos(qz) \left| \langle \hat{\psi}^\dagger(z)\hat{\psi}(0) \rangle \right|^2.$$

Thus, by Fourier transforming the interference pattern, one can obtain the Fourier transform of the correlation function of a single 1D gas,

$$|A(q,T)|^2 := L \int_0^L dz \cos(qz) \left| \langle \hat{\psi}^\dagger(z)\hat{\psi}(0) \rangle \right|^2. \tag{5.3}$$

The quantity $|A(q,T)|^2$ is also a function of the total driving time T (we have suppressed this time argument T in $\hat{\psi}$ and $\hat{\rho}$ in the above equations). This analysis can in principle be done for fermions and bosons.

Our main results are: (1) We find that parametric drive at frequency Ω creates pairs of excitations with total momentum zero. Therefore, the quantity $|A(q)|$ shows a resonance peak at the wave vector corresponding to half the driving frequency, $q = \Omega/2u_i$ (and, in principle, associated multiples), where u_i is the sound velocity of the corresponding mode. Such an analysis can be used to find the sound velocity of the 1D bose system. (2) For a two component Bose system, we find two primary peaks corresponding to "spin" and "charge" velocity. (3) Similarly one could analyze an interference pattern of a driven 1D system of two component fermions, where one expects two peaks corresponding to spin and charge excitations. For fermions, however, there are some complications due to the rapid decay of the correlation functions, which we will address in Section 5.4.

The remainder of this Chapter is organized as follows: In Section 5.2 we introduce the formalism and describe the relation between a driven 1d gas and a driven simple harmonic oscillator. In Section 5.3 we calculate the correlation functions of driven systems and show how information about the driving can be extracted from the interference pattern. In Section 5.4 we address the problem of observing spin charge separation for fermionic 1d systems.

5.2   Parametric driving and Luttinger mode squeezing

5.2.1   Description of a 1d system: Luttinger liquid

One-dimensional systems of interacting bosons or fermions can in general be described by Hamiltonian

$$
\begin{aligned}
\hat{H} \;=\; & \int_0^L -\frac{\hbar^2}{2m}\hat{\psi}_\sigma^\dagger(z)\nabla^2\hat{\psi}_\sigma(z) & (5.4)\\
& + \int_0^L \int_0^L g_{\sigma\sigma'}(z - z')\hat{\psi}_\sigma^\dagger(z)\hat{\psi}_\sigma(z)\hat{\psi}_{\sigma'}^\dagger(z')\hat{\psi}_{\sigma'}(z')dzdz',
\end{aligned}
$$

where $g(z)$ is the interaction strength, and $\hat{\psi}^\dagger(z)$ creates a particle at point z. Low energy excitations may in turn be described by the Luttinger liquid Hamiltonian which in

momentum space is given by a sum of harmonic oscillators

$$\hat{H} = \frac{1}{2}\sum_{q\neq 0}\left(\frac{\pi u}{K}\hat{\Pi}_q\hat{\Pi}_{-q} + \frac{uK}{\pi}q^2\hat{\varphi}_q\hat{\varphi}_{-q}\right). \tag{5.5}$$

where $\hat{\Pi}$ and $\hat{\varphi}$ are conjugate fields: $\left[\hat{\varphi}_q, \hat{\Pi}_{q'}\right] = i\delta_{q,-q'}$, K and u are the Luttinger parameters, u corresponds to the sound velocity, and K is a dimensionless parameter. For a finite system of length $\mathcal{L}$ we quantize the momentum $q = \frac{2\pi}{\mathcal{L}}n$. We shall first consider the case of spinless bosons and then generalize to a two component Bose mixture and fermions with spin. For a weakly interacting one component Bose system ($K > 1$) the Luttinger parameters are given by[1]

$$K = \pi\hbar\sqrt{\rho_0/gm}, \qquad u = \sqrt{\frac{\rho_0 g}{m}} \tag{5.6}$$

where ρ_0 is the 1D line density, and g is the interaction parameter, related to the three dimensional scattering length a_s through $g = 2h\nu_T a_s$ [13, 72], where ν_T is the transverse trapping frequency. The relation between the physical boson creation operator and the Luttinger fields is given by

$$\hat{\psi}^\dagger(z) = \sqrt{\rho_0 + \hat{\Pi}(z)}e^{-i\hat{\varphi}(z)} \tag{5.7}$$

and the correlation function in the ground state has a power law decay

$$\langle\psi^\dagger(z)\psi(0)\rangle_0 \propto \rho_0\left(\frac{z}{\xi_h}\right)^{-\frac{1}{2K}}, \tag{5.8}$$

where $\xi_h = 2K/\rho_0$ is a short distance cutoff. Let us now assume that there are two species of bosons (e.g. two hyperfine states or two different atoms), labelled $\uparrow$ and $\downarrow$. We further assume that the interaction between two atoms of the species labelled up and the one between two atoms of the species down are the same, $g_{\uparrow\uparrow} = g_{\downarrow\downarrow} = g_\parallel$, a condition that can be realized in experiments using hyperfine states $|F = 1, m_F = -1\rangle$ and $|F = 2, m_F = +1\rangle$ of ^{87}Rb [73, 67, 74]. We label $g_\perp$ the interaction strength between different species. In this case the Hamiltonian separates into a "charge" part with $g_c = g_\parallel + g_\perp$ and "spin" part with $g_s = g_\parallel - g_\perp$. The ground state correlation function becomes

$$\langle\psi^\dagger(z)\psi(0)\rangle_0 \propto \rho_0\left(\frac{z}{\xi_h}\right)^{-\frac{1}{4K_c}-\frac{1}{4K_s}} \tag{5.9}$$

---

[1]This expression holds for weakly interacting bosons; for non-interacting bosons $K \to \infty$; and for impenetrable bosons $K = 1$.

where K_c (K_s) is related to g_c (g_s) through Eq. (5.6).

Next let us consider a fermionic system of two components labelled $\uparrow$ and $\downarrow$. In the case of ultracold atomic gases, two fermions of the same species cannot interact via s-wave scattering ($g_{\parallel} = 0$). In the following we assume δ-interactions and denote by g the interaction constant between two fermions of opposite spin. The Hamiltonian separates in a charge part H_ρ and a spin part $\hat{H}_\sigma$. Both charge and spin part have the form of Eq. (5.5) with the Luttinger parameters[2] given by [53]

$$u_\nu K_\nu = v_F, \tag{5.10}$$

$$\frac{u_\nu}{K_\nu} = v_F \left(1 \pm \frac{g}{\pi v_F}\right), \tag{5.11}$$

here $\nu = \rho, \sigma$ and the upper (lower) sign applies to the charge (spin) mode. The single particle annihilation operators are given by $\psi_\uparrow(z) = \psi_{\uparrow,R}(z) + \psi_{\uparrow,L}(z)$, where the index R (L) stand for a right (left) moving particle, and

$$\hat{\psi}_{\uparrow R}^\dagger(z) \rightarrow \sqrt{\rho_0} e^{-ik_F z} e^{-i(-\hat{\varphi}_\uparrow(z) + \theta_\uparrow(z))}, \tag{5.12}$$

$$\hat{\psi}_{\uparrow L}^\dagger(z) \rightarrow \sqrt{\rho_0} e^{ik_F z} e^{-i(\hat{\varphi}_\uparrow(z) + \theta_\uparrow(z))}, \tag{5.13}$$

analogously for $\downarrow$. The fields which decouple the Hamiltonians in H_ρ and H_σ are given by

$$\varphi_\rho = \frac{1}{\sqrt{2}} (\varphi_\uparrow + \varphi_\downarrow), \tag{5.14}$$

$$\varphi_\sigma = \frac{1}{\sqrt{2}} (\varphi_\uparrow - \varphi_\downarrow). \tag{5.15}$$

and same for θ_ν, which enters in the Luttinger liquid Hamiltonian as $\nabla\theta_\nu(z) = \pi\Pi_\nu(z)$.

The spin part of the Hamiltionan has an additional sine Gordon term, arising from backscattering between fermions with opposite spin ($g_{1\perp}$ term). However, this term renormalizes to zero [53] if $K_\sigma > 1$ (repulsive interactions), otherwise it creates a gap in the spectrum of the spin Hamiltonan. In this work we concentrate on repulsive interactions and the sine-Gordon term is not relevant.

The single particle correlation function in the ground state

$$\langle \psi_\uparrow(z)\psi_\uparrow(0) \rangle = 2\rho_0 \cos(k_F z) \left(\frac{z}{\xi_h}\right)^{-\frac{1}{4}\left(K_\rho + \frac{1}{K_\rho} + K_\sigma + \frac{1}{K_\sigma}\right)} \tag{5.16}$$

is oscillating at the length scale of particle spacing.

---

[2]For fermions: $K_\rho < 1$ for repulsive interaction and $K_\rho > 1$ for attractive interaction. $K = 1$ for free fermions.

5.2.2 Parametric driving and squeezing

Experimentally the interaction parameter g can be changed by either changing the scattering length a_s, or by changing the transverse confinement. Let us now imagine a 1d system that is parametrically driven by changing g periodically in time for a certain time T,

$$g(t) = \bar{g} \left(1 - \delta' \cos(\Omega t) \right), \tag{5.17}$$

where $\bar{g}$ is the average value of interaction and Ω is the driving frequency. Since the Luttinger Hamiltonian Eq. (5.5) is just a collection of harmonic oscillators, this situation can be mapped to a collection of parametrically driven simple harmonic oscillators via $\hat{P}_q = -\sqrt{uKq^2/\pi}\hat{\varphi}_q$ and $\hat{Q}_q = \sqrt{\pi/uKq^2}\hat{\Pi}_q$. We note that this mapping is time-independent for both the bosonic and the fermionic case, as uK remains constant. Each pair of modes $(q, -q)$ is then described by

$$\hat{H}_q(t) = \frac{1}{2}\hat{P}_q\hat{P}_{-q} + \frac{\omega_q^2}{2} \left[1 - \delta \cos(\Omega t) \right] \hat{Q}_q\hat{Q}_{-q} \tag{5.18}$$

with

$$\omega_q = \bar{u}q, \tag{5.19}$$

and $\bar{u}^2 = \bar{g}\rho_0$, $\delta = \delta'$ for bosons and $\bar{u}_\nu^2 = v_F^2(1 \pm \frac{\bar{g}}{\pi v_F})$, $\delta = \pm\delta'\frac{\bar{g}}{\pi v_F \pm \bar{g}}$ for fermions. It is well know that a parametrically driven quantum harmonic oscillator can be mapped to a static reference system [75]. If initially in the ground state, the final state after a driving time T is, up to an overall phase factor, given by $\hat{S}\left(\xi_q(T)\right)|0\rangle$ where

$$\hat{S}(\xi_q(T)) = \exp\left[\xi_q^*(T)\hat{a}_q\hat{a}_{-q} - \xi_q(T)\hat{a}_q^\dagger\hat{a}_{-q}^\dagger\right] \tag{5.20}$$

is the squeezing operator, and $\hat{a}_q$ $(\hat{a}_q^\dagger)$ is the annihilation (creation) operator of one excitation in the static reference system,

$$\hat{a}_q = \sqrt{\frac{\omega_{\text{ref}}(q)}{2}} \left(\hat{Q}_q + \frac{i}{\omega_{\text{ref}}(q)}\hat{P}_q \right). \tag{5.21}$$

We choose our reference system to have the eigenfrequency of the system at $t = 0$, $\omega_{\text{ref}}(q) = \omega_q\sqrt{1-\delta}$. The squeezing parameter $\xi_q(T)$ can be expressed in terms of solutions of the classical parametrically driven harmonic oscillator, namely solutions to the following second order differential equation

$$z''(\tau) + \left(\frac{2\omega_q}{\Omega}\right)^2 \left[1 - \delta \cos(2\tau)\right] z(\tau) = 0, \tag{5.22}$$
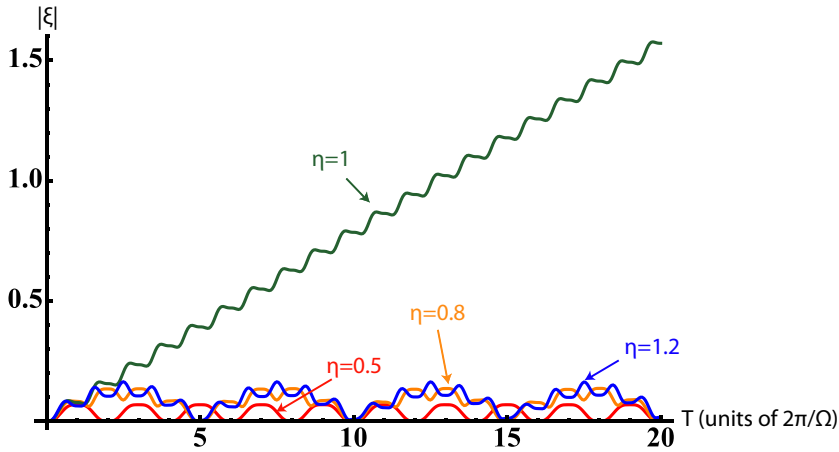
a)
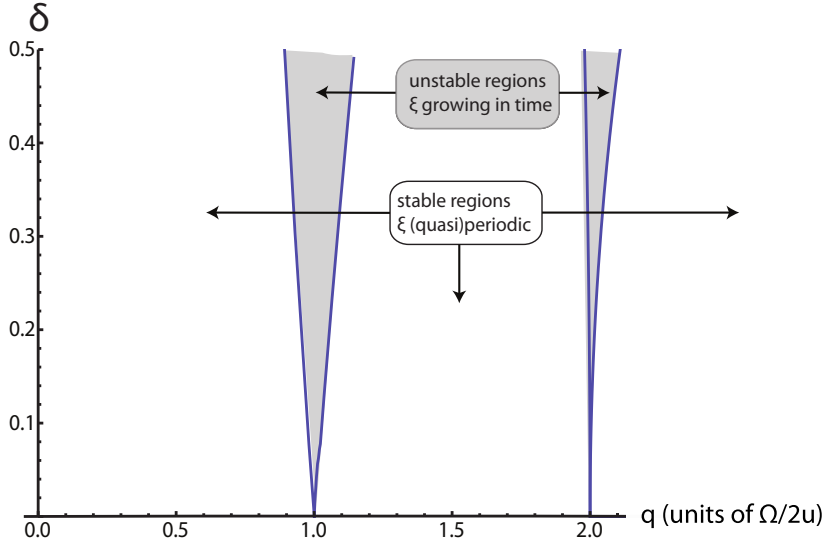
b)

Figure 5.2: a) Stability diagram of Eq. (5.22), as a function of momentum q (in units of $\frac{\Omega}{2\bar{u}}$) and relative driving amplitude δ. Gray shaded regions are resonant, where the number of excitations in that mode grows exponentially in time. White regions are off-resonant and the number of excitations is a (quasi-) periodic function in time and thus bounded from above. b) Absolute value of squeezing parameter $|\xi|$ as a function of time for different values of $\eta = \frac{2\omega_q}{\Omega}$, at fixed $\delta = .1$. In the unstable region, ξ grows linearly in time. The first resonance occurs at $2uq = \Omega$, when the driving frequency is twice the frequency of an excitation in that mode, since excitations are created in pairs $(-q, q)$.
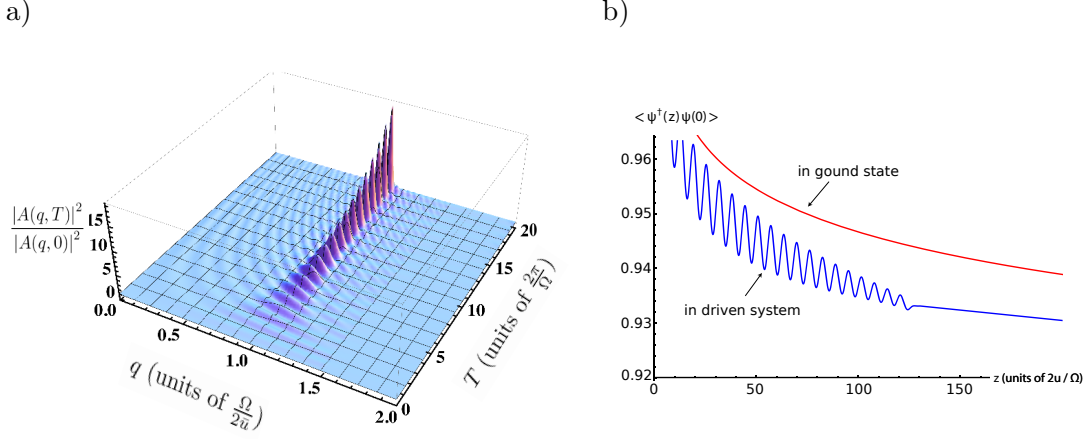
a) b)

Figure 5.3: Driven one-dimensional Bose gas: (a) Observable quantity $\langle |A(q,T)|^2 \rangle$, divided by its ground state value, as a function of wavevector q and number of oscillations complete during driving time T. At $T = 0$ the system is in the ground state. As driving continues a resonance peak corresponding to the drive frequency and sound velocity emerges and grows in time. The relative driving amplitude here is $\delta = .1$. (b) Correlation function after driving time $T = 20\frac{2\pi}{\Omega}$.

which we have expressed in dimensionless variables, and $\tau = \frac{\Omega t}{2}$. We define $\eta = \frac{2\omega q}{\Omega}$, and $\eta_{\text{ref}} = \eta\sqrt{1-\delta}$. Let $\mathcal{X}(\tau)$ and $\mathcal{Y}(\tau)$ be solutions of this equation with $\mathcal{X}(0) = \mathcal{Y}'(0) = 1$ and $\mathcal{X}'(0) = \mathcal{Y}(0) = 0$, and define $z(\tau) = \mathcal{X}(\tau) + i\eta_{\text{ref}}\mathcal{Y}(\tau)$, then ξ_q is defined through

$$4\cosh^2(|\xi_q|) = |z|^2 + \left|z'\right|^2 / \eta_{\text{ref}}^2 + 2 \tag{5.23}$$

and an expression for its phase, $\xi = |\xi|\, e^{i\vartheta}$, can be found through $\vartheta = \vartheta_u + \vartheta_v$, where $|u| = \cosh|\xi|$, and [75]

$$u = |u|\, e^{i\vartheta_u} = \frac{e^{-i\omega_r t}}{2}\left[z(t) - \frac{i\dot{z}(t)}{\omega_r}\right], \tag{5.24}$$

$$v = |v|\, e^{i\vartheta_v} = \frac{e^{i\omega_r t}}{2}\left[z(t) + \frac{i\dot{z}(t)}{\omega_r}\right]. \tag{5.25}$$

Physically relevant quantities can be expressed in terms of the above, e.g. average number of excitations $\langle \hat{a}^\dagger \hat{a} \rangle = \sinh^2 |\xi|$, and uncertainties in position and momentum variables: $\eta_{\text{ref}}\frac{\Omega}{2}\Delta\hat{x}^2 = |z|/2$ and $\eta_{\text{ref}}\frac{2}{\Omega}\Delta\hat{p}^2 = |z'|/2$.

We note that Eq. (5.22) is Mathieu's equation and its odd and even solutions $\mathcal{X}(\tau)$ and $\mathcal{Y}(\tau)$ are referred to as Mathieu S and Matheiu C functions, because of their resemblance to sinusoidal functions in certain parameter regimes. Depending on parameters η and δ, this

equation has stable, i.e. (quasi-)periodic solutions or unstable i.e. exponentially growing
and decaying solutions, see Fig. 5.2. On resonance $\eta \approx 1$ the squeezing parameter grows as
$|\xi| \approx \frac{\delta}{8} T \Omega$.

To summarize the above, the final state of a parametrically driven 1d system is
fully described by the set of squeezing parameters ξ_q, which in turn is given by solutions of
Eq. (5.22).

5.3   Detecting excitations via interference

We now show how the excitations of the driven condensate change the correlation
function and the interference pattern. While the parameter K can be extracted from the
ground state interference pattern, interference of driven systems could be used to measure
the sound velocity u. Given a set of squeezing parameters ξ_q we calculate the correlation
function for bosons and fermions and obtain $\langle |A_q|^2 \rangle$, a quantity that can be extracted from
the interference pattern in experiments.

5.3.1   Bosons: one and two component systems

The correlation function can be written in terms of the quadratures $\langle \hat{\varphi}_q \hat{\varphi}_{-q} \rangle_t$ as

$$\langle \hat{\psi}^\dagger(z) \hat{\psi}(0) \rangle \;=\; \rho_0 \left(\frac{z}{\xi_h} \right)^{-\frac{1}{2K}} e^{-\frac{1}{K} \int d(\eta) \sin^2 \left(\frac{\eta \tilde{z}}{2} \right) d\eta} \tag{5.26}$$

where $\tilde{z} = \frac{\Omega}{2u} z$ is the normalized dimensionless position variable. The function $d(\eta)$ is
defined as the change in quadrature $\langle \hat{\varphi}_q \hat{\varphi}_{-q} \rangle_t$ due to the excitations,

$$d \left(\frac{2\bar{u}}{\Omega} q \right) \;:=\; \frac{K\Omega}{2\bar{u}} \left(\langle \hat{\varphi}_q \hat{\varphi}_{-q} \rangle_t - \langle \hat{\varphi}_q \hat{\varphi}_{-q} \rangle_0 \right) \tag{5.27}$$

and can be expressed in terms of the squeezing parameters $\xi_\eta = r_\eta e^{i\vartheta_\eta}$

$$d \left(\frac{2\bar{u}}{\Omega} q \right) = \frac{1}{q} \left(\cosh(2 |\xi_q|) - \cos \vartheta_q \sinh(2 |\xi_q|) - 1 \right).$$

We calculate the correlation function and $\langle |A_q|^2 \rangle$ of a 1D bose gas after it has been paramet-
rically driven. The integral in the exponent of Eq. (5.26) is evaluated numerically. Fig. 5.3
shows a result, as expected there is a peak in $|A_q|^2$ at a momentum corresponding to the
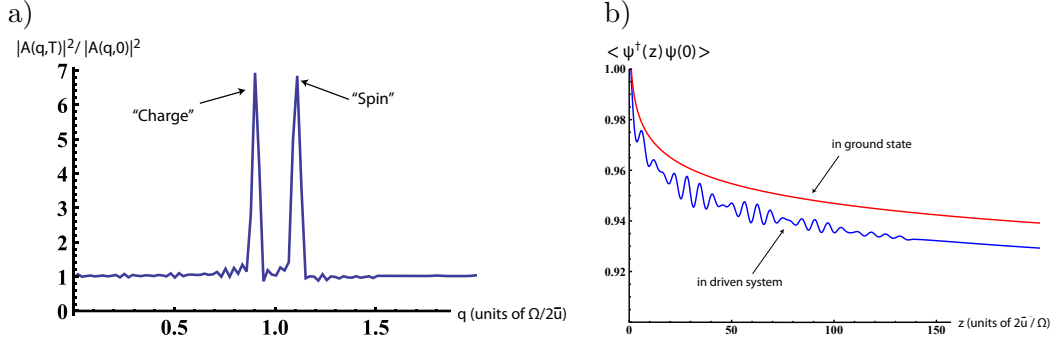driving frequency.

Figure 5.4: Observable quantity $\langle |A_q|^2 \rangle$ and correlations function for parametrically driven two component one-dimensional Bose gas. The parameters here chosen are $\delta = .1$ and number of oscillations in driving $n = \left(\frac{T\Omega}{2\pi} \right) = 20$.

There are two modes in a two component bose system with different sound velocities. The parametric driving excited each of the modes independently. This creates beats in the correlation function, which can be seen as peaks in A_q: there are then two peaks, one corresponding to each mode, see Fig. 5.4. This setup can be used to probe spin-charge separation in continuous bosonic systems. It has previously been proposed to use continuous bosonic one-dimensional systems to probe spin-charge separation [64] .

5.3.2 Two component Fermi systems

We first calculate the correlation function for the driven fermi gas. Note that both fields appear in the exponent of single particle operators, see Eq. (5.2.1). We find for each mode

$$\langle \hat{\psi}_R^\dagger(z)\hat{\psi}_R(0) \rangle = \rho_0 e^{-ik_F z} \left(\frac{z}{\xi_h} \right)^{-\frac{1}{2}\left(K + \frac{1}{K} \right)} e^{-I(z)} \tag{5.28}$$

$$I(z) = \int d\eta \sin^2\left(\frac{\eta \tilde{z}}{2} \right) \left[\left(K + \frac{1}{K} \right) \sinh^2(r_\eta) - \left| K - \frac{1}{K} \right| \cos \vartheta_\eta \sinh(2r_\eta) \right]. \tag{5.29}$$

The above formula is valid for spin-polarized fermions, and also for spin and charge part of a two component system of fermions. In that case, we just have to replace the constants (e.g. interaction strength g and what follows from it) by the corresponding value for the spin- or charge part.

As a first approximation, let us neglect the second part of $I(z)$ with respect to the first

part. There are two reasons for that: first, for fermions the Luttinger parameter K is close to one (in fact, for the spin part it renormalizes to $K_\sigma = 1$), second, only the second term contains the phase of the squeezing parameter $\cos \vartheta_q$, which will average out if the systems are left to evolve after driving and before interfering. We then have

$$I(z) \approx \text{const} - \left(K + \frac{1}{K} \right) \int d\eta \cos \left(\eta \tilde{z} \right) \frac{1}{\eta} \sinh^2 r_\eta \tag{5.30}$$

which contains the Fourier transform of the function $d'(\eta) = \frac{1}{\eta} \sinh^2 r_\eta$, which is a function peaked around $\eta = 1$ with height $\sinh^2 \left(\frac{\pi n \delta}{4} \right)$ and width $\delta/2$. Fourier transforming it will give an oscillating part in the correlation function.

Directly calculating $|A_q|$ in the same way as for bosons does not give any peaks. In the next section we discuss why and how to resolve this issue. Using parametric driving and analyzing the momentum distribution of cold fermionic gases to study spin-charge separation has been proposed in [69, 70]. Here we propose to analyze an interference pattern.

5.4   Observing Spin Charge Separation for Fermions

In Fig. 5.4 we see two peaks in $|A_q|^2$ for the two component bose system, corresponding to the sound velocities of two modes. In this section we show how one could observe spin charge separation for fermions in a similar way, however, for fermions there are some complications. The fast decay of correlation functions coming from the factor $(1/K + K)$ in the power law exponent poses a problem when calculating $\langle |A_q|^2 \rangle$, as this quantity will then be dominated by contributions from close to the origin $z = 0$, preventing the Fourier transform from resolving the beats in the correlation function. We can solve this problem by using a simple trick to avoid the region around the origin (similarly as used in [76]). We need to extract

$$\int_{z^{\text{beg}}}^{z^{\text{end}}} \cos(zq) \left| \langle \hat{\psi}^\dagger(z) \hat{\psi}(0) \rangle \right|^2 \tag{5.31}$$

from the interference pattern, with $z^{\text{end}} > z^{\text{beg}} > 0$.

This can be realized by looking at correlations of Fourier transformations of density of different regions in the interference pattern. For this purpose we define

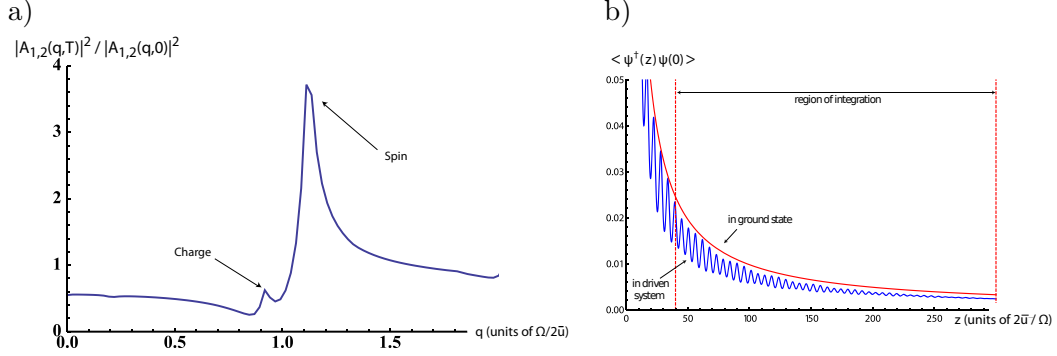$$\hat{\tilde{\rho}}_{1/2}(x, q) = \int_{\text{region } 1/2} e^{iqz} \hat{\rho}(x, z) dz \tag{5.32}$$

Figure 5.5: Fermions with spin: (a) $\langle |A_{1,2}(q,T)|^2 \rangle$ shows a peak for the spin mode and one for the charge mode. To obtain these peaks, one has to integrate over different regions of the interference patter, see text. (b) Correlation function for driven two component system of fermions, and integration region.

and choose the two regions so that they have no overlap. Then

$$\langle \hat{\tilde{\rho}}_1(x,q)\hat{\tilde{\rho}}_2(0,-q)\rangle = 2\cos(xQ)\langle A_{\mathrm{reg1}}(q)A^{\dagger}_{\mathrm{reg2}}(q)\rangle \tag{5.33}$$

where we defined $A_{\mathrm{reg}\ i}(q) = \int_{\mathrm{region}\ i} e^{iqz}\hat{\psi}_1^{\dagger}(z)\hat{\psi}_2(z)dz$ and we have

$$\langle A_{\mathrm{reg}\ 1}(q)A^{\dagger}_{\mathrm{reg}\ 2}(q)\rangle \approx L \int_{z_2^{\mathrm{beg}}-z_1^{\mathrm{end}}}^{z_2^{\mathrm{end}}-z_1^{\mathrm{beg}}} e^{izq}\left|\langle\hat{\psi}^{\dagger}(z)\hat{\psi}(0)\rangle\right|^2. \tag{5.34}$$

Note that because of the different regions the above quantity does not have to be real. We define

$$|A_{1,2}(q)|^2 = \left|\langle A_{\mathrm{reg}\ 1}(q)A^{\dagger}_{\mathrm{reg}\ 2}(q)\rangle\right|. \tag{5.35}$$

This quanity as well as the correlation function is shown in Fig. 5.5, where the red lines in the plot of the correlation function in mark z_{begin} and z_{end}. $|A_{1,2}(q)|^2$ shows two peaks corresponding to charge and spin velocities. The difference in size of the peaks is simply due to the different relative change in the sound velocities u, which are given by Eq. (5.11), where the relative change in g is of course equal for both modes. There are more excitations in the spin sector.

5.5 Conclusions

We have studied interference of parametrically driven one-dimensional systems of both bosonic and fermionic ultracold systems, and found that the interference pattern contains information about the excitations driven into the systems. For two component systems

two kinds of excitations are driven on resonance: those corresponding to charge velocity, and those corresponding to spin velocity. This can be extracted from the interference pattern. In the case of fermions one needs to use different regions of the interference pattern to resolve the effect. We argued that such experiments could be used to probe properties of one-dimensional systems, as measuring the sound velocity, and spin charge separation.

Note added: During the preparation of this manuscript the author became aware of Refs. [69, 70], who studied similar effects for fermionic systems and obtained similar results.

5.6 Appendix: Derivation of equation Eq. (5.1)

When we write down the creation operator $\hat{\psi}^{\dagger}_{\text{cloud}}(x_1, z_1)$ for a particle after expansion at position (x_1, z_1), this particle can have come from either quasicondensate, and there is a relative phase between those paths

$$\hat{\psi}^{\dagger}_{\text{cloud}}(x, z) \propto \hat{\psi}^{\dagger}_1(z) e^{ixQ/2} + \hat{\psi}^{\dagger}_2(z) e^{-ixQ/2} \tag{5.36}$$

where $\hat{\psi}^{\dagger}_j(z)$, $j = 1, 2$, is the creation operator for a particle in quasicondensate j before expansion, and we factored out a common phase. The relative phase comes from the expansion the particles initially confined in a harmonic potential (particles only occupy the ground state of the transversal confinement). Consider first a particle in a harmonic oscillator at position $x \pm d/2$, whose potential is suddenly removed. The wave function $f_{\pm}(x, t)$ expands and picks up a phase factor

$$f_{\pm}(x, t) = \frac{1}{\pi^{3/4}\sqrt{R_t}} \exp\left[-\frac{\left(x \pm \frac{d}{2}\right)^2 \left(1 - i\frac{t}{mR_0^2}\right)}{2R_t^2}\right] \tag{5.37}$$

where $R_0 = \sqrt{\frac{\hbar}{m\omega_{\perp}}}$ is the initial radius of the Gaussian wave function, m is the particle mass, and $\omega_{\perp}$ is the harmonic oscillator potential, here the transverse confinement frequency, and

$$R_t^2 = R_0^2 + \left(\frac{\hbar t}{mR_0}\right)^2. \tag{5.38}$$

For large expansion times, so that $R_t \gg R_0$, $R_t \to \frac{\hbar t}{mR_0}$, and

$$f_{\pm}(x, t) \approx \frac{1}{\pi^{3/4}\sqrt{R_t}} \exp\left[i\frac{m}{2\hbar t}\left(x \pm \frac{d}{2}\right)^2\right]. \tag{5.39}$$

As the two systems are initially independent, $\langle \hat{\psi}_1^\dagger(z)\psi_2(z)\rangle = 0$, and thus the expectation value

$$\langle \hat{\psi}_{\text{cloud}}^\dagger(x,z)\psi_{\text{cloud}}(x,z)\rangle = \text{const.} \tag{5.40}$$

However, each single shot will have interference fringes due to interference of the different paths, which one can see in the expectation value of the density-density correlation function $\langle \hat{\rho}(x_1,z_1)\hat{\rho}(x_2,z_2)\rangle$ of the cloud. The operator for finding one particle at $r_1 = (x_1,z_1)$, and the other one in $r_2 = (x_2,z_2)$, is proportional to

$$\begin{aligned}\hat{\psi}_{\text{cloud}}(r_1)\hat{\psi}_{\text{cloud}}(r_2) \quad \propto \quad &\hat{\psi}_1(z_1)\hat{\psi}_1(z_2)e^{-i(x_1+x_2)Q/2} + \hat{\psi}_2(z_1)\hat{\psi}_2(z_2)e^{i(x_1+x_2)Q/2} \\ &+\psi_1(z_1)\hat{\psi}_2(z_2)e^{-i\Delta x Q/2} + \psi_2(z_1)\hat{\psi}_1(z_2)e^{i\Delta x Q/2}\end{aligned} \tag{5.41}$$

here $\Delta x = x_1 - x_2$. The first two terms describe the case when the two particles come both from the same quasi condensate. The latter two terms describe the case when the two particles come each from a different quasi condensates: those are the terms giving an oscillating term in Eq. (5.1) – and the interference pattern. When we multiply the above with its complex conjugate, and take the expectation value, the following two terms give non-constant contributions:

$$\begin{aligned}&\langle \hat{\psi}_2^\dagger(z_2)\hat{\psi}_1^\dagger(z_1)\psi_2(z_1)\psi_1(z_2)\rangle e^{i\Delta x Q} + \text{H.c.} \pm \langle \hat{\psi}_2^\dagger(z_2)\hat{\psi}_2(z_1)\rangle\langle \hat{\psi}_1^\dagger(z_1)\hat{\psi}_1(z_2)\rangle e^{i\Delta x Q} + \text{H.c.} \\ = \quad &\pm 2\left|\langle \hat{\psi}^\dagger(z_2)\hat{\psi}(z_1)\rangle\right|^2 \cos(\Delta x Q)\end{aligned} \tag{5.42}$$

the upper (lower) sign is for bosons (fermions). In the first step we assumed that systems 1 and 2 are independent, thus the expectation value factorizes, in the second step we assumed that they are equal, i.e. in the same quantum state, and used ψ to describe that state.

Bibliography

[1] Immanuel Bloch, Jean Dalibard, and Wilhelm Zwerger. *Many-Body Physics with Ultracold Gases.* Reviews of Modern Physics **80**, 885 (2008).

[2] Markus Greiner, Olaf Mandel, Tilman Esslinger, Theodor W. Hansch, and Immanuel Bloch. *Quantum phase transition from a superfluid to a Mott insulator in a gas of ultracold atoms.* Nature **415** (6867), 39–44 (2002).

[3] Jonathan Simon, Waseem S. Bakr, Ruichao Ma, M. Eric Tai, Philipp M. Preiss, and Markus Greiner. *Quantum simulation of antiferromagnetic spin chains in an optical lattice.* Nature **472**, 307–312 (2011).

[4] Waseem S. Bakr, Philipp M. Preiss, M. Eric Tai, Ruichao Ma, Jonathan Simon, and Markus Greiner. *Interaction-induced orbital excitation blockade of ultracold atoms in an optical lattice.* arXiv:1105.5834v1.

[5] Waseem S. Bakr, Jonathon I. Gillen, Amy Peng, Simon Folling, and Markus Greiner. *A quantum gas microscope for detecting single atoms in a Hubbard-regime optical lattice.* Nature **462** (7269), 74–77 (2009).

[6] W. S. Bakr, A. Peng, M. E. Tai, R. Ma, J. Simon, J. I. Gillen, S. Fölling, L. Pollet, and M. Greiner. *Probing the Superfluid-to-Mott Insulator Transition at the Single-Atom Level.* Science **329**, 547–550 (2010).

[7] Subir Sachdev, K. Sengupta, and S. M. Girvin. *Mott insulators in strong electric fields.* Phys. Rev. B **66**, 075128 (2002).

[8] S. Trotzky, P. Cheinet, S. Flling, M. Feld, U. Schnorrberger, A. M. Rey, A. Polkovnikov, E. A. Demler, M. D. Lukin, and I. Bloch. *Time-Resolved Observation and Control of Superexchange Interactions with Ultracold Atoms in Optical Lattices.* Science **319** (5861), 295–299 (2008).

[9] K. Sengupta, Stephen Powell, and Subir Sachdev. *Quench dynamics across quantum critical points.* Phys. Rev. A **69**, 053616 (2004).

[10] J. Ignacio Cirac, Paolo Maraner, and Jiannis K. Pachos. *Cold Atom Simulation of Interacting Relativistic Quantum Field Theories.* Phys. Rev. Lett. **105** (19), 190403 (2010).

[11] Niels Strohmaier, Daniel Greif, Robert Jördens, Leticia Tarruell, Henning Moritz, Tilman Esslinger, Rajdeep Sensarma, David Pekker, Ehud Altman, and Eugene Demler. *Observation of Elastic Doublon Decay in the Fermi-Hubbard Model.* Phys. Rev. Lett. **104**, 080401 (2010).

[12] Toshiya Kinoshita, Trevor Wenger, and David S. Weiss. *Observation of a One-Dimensional Tonks-Girardeau Gas.* Science **305**, 1125–1128 (2004).

[13] S. Hofferberth, I. Lesanovsky, B. Fischer, T. Schumm, and J. Schmiedmayer. *Non-equilibrium coherence dynamics in one-dimensional Bose gases.* Nature **449**, 324–327 (2007).

[14] Takuya Kitagawa, Susanne Pielawa, Adilet Imambekov, Jörg Schmiedmayer, Vladimir Gritsev, and Eugene Demler. *Ramsey Interference in One-Dimensional Systems: The Full Distribution Function of Fringe Contrast as a Probe of Many-Body Dynamics.* Phys. Rev. Lett. **104**, 255302 (2010).

[15] Jacob F. Sherson, Christof Weitenberg, Manuel Endres, Marc Cheneau, Immanuel Bloch, and Stefan Kuhr. *Single-atom-resolved fluorescence imaging of an atomic Mott insulator.* Nature **467** (7311), 68–72 (2010).

[16] Paul Fendley, K. Sengupta, and Subir Sachdev. *Competing density-wave orders in a one-dimensional hard-boson model.* Phys. Rev. B **69** (7), 075106 (2004).

[17] D. Jaksch, C. Bruder, J. I. Cirac, C. W. Gardiner, and P. Zoller. *Cold Bosonic Atoms in Optical Lattices.* Phys. Rev. Lett. **81** (15), 3108–3111 (Oct 1998).

[18] Sebastian Will, Thorsten Best, Ulrich Schneider, Lucia Hackermuller, Dirk-Soren Luhmann, and Immanuel Bloch. *Time-resolved observation of coherent multi-body interactions in quantum phase revivals.* Nature **465**, 197–201 (2010).

[19] P R Johnson, E Tiesinga, J V Porto, and C J Williams. *Effective three-body interactions of neutral bosons in optical lattices.* New Journal of Physics **11**, 093022 (2009).

[20] Waseem Bakr, (private communication).

[21] M.A. Novotny and D.P. Landau. *Zero temperature phase diagram for the d=1 quantum Ising antiferromagnet.* Journal of Magnetism and Magnetic Materials **54-57** (Part 2), 685 – 686 (1986).

[22] A. A. Ovchinnikov, D. V. Dmitriev, V. Ya. Krivnov, and V. O. Cheranovskii. *Antiferromagnetic Ising chain in a mixed transverse and longitudinal magnetic field.* Phys. Rev. B **68** (21), 214406 (2003).

[23] O. Perron. *Zur Theorie der Matrices.* Mathematische Annalen **64 (2)**, 248 – 263 (1907).

[24] G. Frobenius. *Über Matrizen aus nicht negativen Elementen.* Sitzungsber. Königl. Preuss. Akad. Wiss. pages 456 – 477 (1912).

[25] A. Auerbach. *Interacting Electrons and Quantum Magnetism.* Springer (1994).

[26] Daniel S. Rokhsar and Steven A. Kivelson. *Superconductivity and the Quantum Hard-Core Dimer Gas.* Phys. Rev. Lett. **61**, 2376–2379 (1988).

[27] R. J. Baxter. *Exactly solved models in statistical mechanics.* Academic Press (1982).

[28] K. S. Raman, R. Moessner, and S. L. Sondhi. *SU(2)-invariant spin-* 12 *Hamiltonians with resonating and other valence bond phases.* Phys. Rev. B **72** (6), 064413 (2005).

[29] N. Read and Subir Sachdev. *Spin-Peierls, valence-bond solid, and Néel ground states of low-dimensional quantum antiferromagnets.* Phys. Rev. B **42** (7), 4568–4589 (1990).

[30] Ashvin Vishwanath, L. Balents, and T. Senthil. *Quantum criticality and deconfinement in phase transitions between valence bond solids.* Phys. Rev. B **69** (22), 224416 (2004).

[31] Eduardo Fradkin, David A. Huse, R. Moessner, V. Oganesyan, and S. L. Sondhi. *Bipartite Rokhsar–Kivelson points and Cantor deconfinement.* Phys. Rev. B **69**, 224415 (2004).

[32] P. W. Leung, K. C. Chiu, and Karl J. Runge. *Columnar dimer and plaquette resonating-valence-bond orders in the quantum dimer model.* Phys. Rev. B **54**, 12938–12945 (1996).

[33] Olav F. Syljuåsen. *Plaquette phase of the square-lattice quantum dimer model: Quantum Monte Carlo calculations.* Phys. Rev. B **73** (24), 245105 (Jun 2006).

[34] A. Ralko, D. Poilblanc, and R. Moessner. *Generic Mixed Columnar-Plaquette Phases in Rokhsar-Kivelson Models.* Phys. Rev. Lett. **100** (3), 037201 (Jan 2008).

[35] E. Fradkin and S. A. Kivelson. *Short range resonating valence bond theories and superconductivity.* Mod. Phys. Lett. B **4**, 225 (1990).

[36] Leon Balents, Lorenz Bartosch, Anton Burkov, Subir Sachdev, and Krishnendu Sengupta. *Putting competing orders in their place near the Mott transition. II. The doped quantum dimer model.* Phys. Rev. B **71** (14), 144509 (Apr 2005).

[37] M. Girardeau. *Relationship between Systems of Impenetrable Bosons and Fermions in One Dimension.* J. Math. Phys. **1**, 516 (1960).

[38] Ulli Wolff. *Collective Monte Carlo Updating for Spin Systems.* Phys. Rev. Lett. **62** (4), 361–364.

[39] Robert H. Swendsen and Jian-Sheng Wang. *Nonuniversal critical dynamics in Monte Carlo simulations.* Phys. Rev. Lett. **58** (2), 86–88 (1987).

[40] Steven E. Koonin and Dawn C. Meredith. *Computational Physics.* Westview Press (1990).

[41] Nicholas Metropolis, Arianna W. Rosenbluth, Marshall N. Rosenbluth, Augusta H. Teller, and Edward Teller. *Equation of State Calculations by Fast Computing Machines.* The Journal of Chemical Physics **21**, 1087 (1953).

[42] K. Binder. *Finite size scaling analysis of ising model block distribution functions.* Zeitschrift für Physik B Condensed Matter **43**, 119–140 (1981).

[43] Subir Sachdev. *Quantum Phase Transitions.* Cambridge University Press (2011).

[44] John Cardy. *Scaling and Renormalization in Statistical Physics.* Cambridge University Press (2002).

[45] J. Ashkin and E. Teller. *Statistics of Two-Dimensional Lattices with Four Components.* Phys. Rev. **64** (5-6), 178–184 (1943).

[46] Kean Loon Lee, Benoît Grémaud, Rui Han, Berthold-Georg Englert, and Christian Miniatura. *Ultracold fermions in a graphene-type optical lattice.* Phys. Rev. A **80** (4), 043411 (Oct 2009).

[47] Subir Sachdev and R. N. Bhatt. *Bond-operator representation of quantum spins: Mean-field theory of frustrated quantum Heisenberg antiferromagnets.* Phys. Rev. B **41** (13), 9323–9329 (May 1990).

[48] Sudha Gopalan, T. M. Rice, and M. Sigrist. *Spin ladders with spin gaps: A description of a class of cuprates.* Phys. Rev. B **49** (13), 8901–8910 (Apr 1994).

[49] J. Piekarewicz and J. R. Shepard. *Mean-field theory for spin ladders using angular-momentum coupled bases.* Phys. Rev. B **60** (13), 9456–9467 (Oct 1999).

[50] Milton Abramowitz and Irene A. Stegun. *Handbook of Mathematical Functions with Formulas, Graphs, and Mathematical Tables.* Dover New York, ninth dover printing, tenth gpo printing edition (1964).

[51] Fabien Alet, Stefan Wessel, and Matthias Troyer. *Generalized directed loop method for quantum Monte Carlo simulations.* Phys. Rev. E **71** (3), 036706 (2005).

[52] A.F. Albuquerque, F. Alet, P. Corboz, P. Dayal, A. Feiguin, S. Fuchs, L. Gamper, E. Gull, S. Grtler, A. Honecker, R. Igarashi, M. Krner, A. Kozhevnikov, A. Luchli, S.R. Manmana, M. Matsumoto, I.P. McCulloch, F. Michel, R.M. Noack, G. Pawlowski, L. Pollet, T. Pruschke, U. Schollwck, S. Todo, S. Trebst, M. Troyer, P. Werner, and S. Wessel. *The ALPS project release 1.3: Open-source software for strongly correlated systems.* Journal of Magnetism and Magnetic Materials **310** (2, Part 2), 1187 – 1193 (2007). Proceedings of the 17th International Conference on Magnetism, The International Conference on Magnetism.

[53] Thierry Giamarchi. *Quantum Physics in One Dimension.* Oxford Science Publications (2003).

[54] Z. Y. Meng, T. C. Lang, S. Wessel, F. F. Assaad, and A. Muramatsu. *Quantum spin liquid emerging in two-dimensional correlated Dirac fermions.* Nature **464**, 847–851 (2010).

[55] Y. Jompol, C. J. B. Ford, J. P. Griffiths, I. Farrer, G. A. C. Jones, D. Anderson, D. A. Ritchie, T. W. Silk, and A. J. Schofield. *Probing Spin-Charge Separation in a Tomonaga-Luttinger Liquid.* Science **325**, 597–601 (2009).

[56] C. Kim, A. Y. Matsuura, Z.-X. Shen, N. Motoyama, H. Eisaki, S. Uchida, T. Tohyama, and S. Maekawa. *Observation of Spin-Charge Separation in One-Dimensional SrCuO2.* Phys. Rev. Lett. **77**, 4054–4057 (1996).

[57] B. J. Kim, H. Koh, E. Rotenberg, S.-J. Oh, H. Eisaki, N. Motoyama, S. Uchida, T. Tohyama, S. Maekawa, Z.-X. Shen, and C. Kim. *Distinct spinon and holon dispersions in photoemission spectral functions from one-dimensional $SrCuO_2$.* Nature Physics **2**, 397 – 401 (2006).

[58] M. Hengsberger P. Segovia, D. Purdie and Y. Baer. *Observation of spin and charge collective modes in one-dimensional metallic chains.* Nature **402**, 504–507 (1999).

[59] Yaroslav Tserkovnyak, Bertrand I. Halperin, Ophir M. Auslaender, and Amir Yacoby. *Interference and zero-bias anomaly in tunneling between Luttinger-liquid wires.* Phys. Rev. B **68**, 125312 (2003).

[60] O. M. Auslaender, A. Yacoby, R. de Picciotto, K. W. Baldwin, L. N. Pfeiffer, and K. W. West. *Tunneling Spectroscopy of the Elementary Excitations in a One-Dimensional Wire.* Science **295**, 825 – 828 (2002).

[61] O. M. Auslaender, H. Steinberg, A. Yacoby, Y. Tserkovnyak, B. I. Halperin, K. W. Baldwin, L. N. Pfeiffer, and K. W. West. *Spin-Charge Separation and Localization in One Dimension.* Science **308**, 88 – 92 (2005).

[62] Markus Greiner, Immanuel Bloch, Olaf Mandel, Theodor W. Hänsch, and Tilman Esslinger. *Exploring Phase Coherence in a 2D Lattice of Bose-Einstein Condensates.* Phys. Rev. Lett. **87**, 160405 (2001).

[63] Henning Moritz, Thilo Stöferle, Michael Köhl, and Tilman Esslinger. *Exciting Collective Oscillations in a Trapped 1D Gas.* Phys. Rev. Lett. **91**, 250402 (2003).

[64] A. Kleine, C. Kollath, I. P. McCulloch, T. Giamarchi, and U. Schollwöck. *Spin-charge separation in two-component Bose gases.* Phys. Rev. A **77**, 013607 (2008).

[65] Belen Paredes, Artur Widera, Valentin Murg, Olaf Mandel, Simon Fölling, Ignacio Cirac, Gora V. Shlyapnikov, Theodor W. Hänsch, and Immanuel Bloch. *Tonks-Girardeau gas of ultracold atoms in an optical lattice.* Nature **429**, 277–281 (2004).

[66] A Recati, P O Fedichev, W Zwerger, and P Zoller. *Fermi one-dimensional quantum gas: Luttinger liquid approach and spincharge separation.* Journal of Optics B **5**, S55 (2003).

[67] S. Hofferberth, I. Lesanovsky, T. Schumm, A. Imambekov, V. Gritsev, E. Demler, and J. Schmiedmayer. *Probing quantum and thermal noise in an interacting many-body system.* Nature Physics **4**, 489 – 495 (2008).

[68] Adilet Imambekov, Vladimir Gritsev, and Eugene Demler. *Fundamental noise in matter interferometers.* arXiv:cond-mat/0703766v1 (2007).

[69] Yu. Kagan and L. A. Manakova. *Parametric generation of density and spin modes with formation of stationary condensed states in ultracold two-component quasi-one-dimensional Fermi gases.* Physical Review A (Atomic, Molecular, and Optical Physics) **80**, 023625 (2009).

[70] C. D. Graf, G. Weick, and E. Mariani. *Parametric resonance and spin-charge separation in 1D fermionic systems.* EPL (Europhysics Letters) **89**, 40005 (2010).

[71] Anatoli Polkovnikov, Ehud Altman, and Eugene Demler. *Interference between independent fluctuating condensates.* Proc Natl Acad Sci USA **103**, 6125–6129 (2006).

[72] M. A. Cazalilla. *Bosonizing one-dimensional cold atomic gases.* AMOP **37**, S1 (2004).

[73] Artur Widera, Stefan Trotzky, Patrick Cheinet, Simon Fölling, Fabrice Gerbier, Immanuel Bloch, Vladimir Gritsev, Mikhail D. Lukin, and Eugene Demler. *Quantum Spin Dynamics of Mode-Squeezed Luttinger Liquids in Two-Component Atomic Gases.* Physical Review Letters **100**, 140401 (2008).

[74] M. Erhard, H. Schmaljohann, J. Kronjäger, K. Bongs, and K. Sengstock. *Measurement of a mixed-spin-channel Feshbach resonance in ^{87}Rb.* Phys. Rev. A **69**, 032705 (2004).

[75] Alla N. Seleznyova. *Unitary transformations for the time-dependent quantum oscillator.* Phys. Rev. A **51**, 950–959 (1995).

[76] V. Gritsev, E. Demler, and A. Polkovnikov. *Interferometric probe of paired states.* Physical Review A **78**, 063624 (2008).